Information Harvesting: Leveraging Wireless Power Transfer for Next-Generation Communication Frameworks

by

Mehmet Ertuğ Pıhtılı

A Dissertation Submitted to the
Graduate School of Sciences and Engineering
in Partial Fulfillment of the Requirements for
the Degree of

Master of Science

in

Electrical and Electronics Engineering

KOÇ ÜNİVERSİTESİ

July 4, 2024

Information Harvesting: Leveraging Wireless Power Transfer for Next-Generation Communication Frameworks

Koç University

Graduate School of Sciences and Engineering

This is to certify that I have examined this copy of a master's thesis by

Mehmet Ertuğ Pıhtılı

and have found that it is complete and satisfactory in all respects,
and that any and all revisions required by the final
examining committee have been made.

Committee Members:

Assoc. Prof. Ertuğrul Başar (Advisor)

Assist. Prof. Murat Kuşcu

Prof. Oğuz Kucur

Date: ______________________

To my dear family...

ABSTRACT

Information Harvesting: Leveraging Wireless Power Transfer for Next-Generation Communication Frameworks
Mehmet Ertuğ Pıhtılı
Master of Science in Electrical and Electronics Engineering
July 4, 2024

As wireless information transmission (WIT) progresses into its sixth generation (6G), the challenge of sustaining terminal operations with limited batteries for Internet-of-things (IoT) platforms arises. Wireless power transfer (WPT) emerges as a solution, empowering battery-less infrastructures and enabling nodes to harvest energy for sustainable operations. The integration of WPT with WIT mechanisms becomes crucial to mitigate the need for battery replacements while ensuring secure and reliable communication. A novel protocol, Information Harvesting (IH), amalgamates WIT and WPT through index modulation (IM) techniques atop the existing far-field WPT mechanism to address challenges in wireless information and power transfer (WIPT).

Moreover, innovative modes of information and power transfer are explored to meet the rising demand for energy and spectrum resources in next-generation IoT systems. One potential solution involves harnessing the active transmission capability of devices to facilitate data transmission and wireless energy harvesting (WEH) for backscatter communication (BC), forming a symbiotic radio (SR) environment. Furthermore, incorporating reconfigurable intelligent surfaces (RISs) into the SR environment enhances the reliability of backscatter communication, reinforcing symbiotic relationships between active and passive devices. This thesis explores novel and synergistic methods for coordinating WPT and WIT in next-generation communication systems through state-of-the-art technologies.

In Chapter 3, a unified framework for index modulation (IM)-based IH mechanisms is presented, evaluating their energy harvesting capability, bit error rate (BER), and ergodic secrecy rate (ESR) performance for diverse IM schemes. The findings indicate significant potential in facilitating reliable data communication within existing far-field WPT systems, underscoring promising refinements in green

and secure communication paradigms for next-generation IoT wireless networks.

Chapter 4 introduces a new IH mechanism atop the orthogonal frequency-division multiplexing (OFDM)-based far-field WPT mechanism, investigating its benefits in terms of harvested energy, achievable rates, and reliability.

Finally, Chapter 5 presents a novel SR system, where a standalone RIS sustains its functions through WEH based on a low-power RIS structure. Mutualistic symbiosis is established by utilizing a signal conveyed by the primary transmitter (PTx) to assist ongoing transmissions and convey information to the primary receiver (PRx). The PTx employs time index modulation (TIM) to transmit information to the PRx and power to the RIS and energy harvester (EH). A log-likelihood ratio (LLR)-based detector is presented to address challenges in the TIM scheme. The performance of the proposed scheme is investigated in terms of harvested direct current (DC) power at the RIS and EH, as well as the BER at the PRx.

ÖZETÇE

Bilgi Toplama: Gelecek Nesil İletişim Sistemleri İçin Kablosuz Güç Transferini Kullanma

Mehmet Ertuğ Pıhtılı
Elektrik ve Elektronik Mühendisliği, Yüksek Lisans
4 Temmuz 2024

Kablosuz bilgi iletimi (WIT), altıncı nesline (6G) doğru ilerledikçe, nesnelerin interneti (IoT) platformları için sınırlı bataryalarla terminal işlemlerini sürdürme zorluğunu ortaya çıkarmaktadır. Kablosuz güç transferi (WPT), bataryasız altyapıları güçlendirerek ve kablosuz cihazların enerji hasatlamasına olanak tanıyarak sürdürülebilir işlemler için bir çözüm olarak ortaya çıkar. WPT'nin WIT mekanizmaları ile entegrasyonu, güvenilir ve güvenli iletişimi sağlarken batarya değişim ihtiyacını azaltmak için hayati öneme sahiptir. Yeni bir protokol olan Bilgi hasatlama (IH), kablosuz bilgi ve güç transferindeki (WIPT) zorlukları ele almak için mevcut uzak alan WPT mekanizmasının üzerine indis modülasyonu (IM) tekniklerini uygulayarak WIT ve WPT'yi birleştirir.

Ayrıca, enerji ve spektrum kaynaklarına olan artan talebi karşılamak için yenilikçi bilgi ve güç transferi modları araştırılmaktadır. Potansiyel çözümlerden biri, cihazların aktif iletim yeteneğini kullanarak veri iletimini ve geri yansıma iletişimi için kablosuz enerji hasatlama (WEH) sağlayarak bir simbiyotik radyo (SR) ortamı oluşturmaktır. Ek olarak, uyarlanabilir akıllı yüzeyleri (RIS'ler) SR ortamına entegre etmek geri yansıma iletişiminin güvenilirliğini artırır ve aktif ve pasif cihazlar arasındaki simbiyotik ilişkileri güçlendirir. Bu tez, gelecek nesil iletişim sistemlerinde WPT ve WIT koordinasyonu için yeni ve sinerjik yöntemleri araştırmaktadır.

Üçüncü Bölümde, IM tabanlı IH mekanizmaları için birleştirilmiş bir yapı sunulmuş ve çeşitli IM şemaları için enerji toplama yetenekleri, bit hata oranları (BER) ve ergodik gizlilik oranı (ESR) performansları değerlendirilmiştir. Bulgular, mevcut uzak alan WPT sistemleri içinde güvenilir veri iletimini kolaylaştırma potansiyelinin önemli olduğunu gösterirken, gelecek nesil IoT kablosuz ağları için yeşil ve güvenli iletişim paradigmalarında umut verici iyileştirmeleri vurgular.

Dördüncü Bölüm, dikey frekans bölmeli çoklama (OFDM) tabanlı uzak alan

WPT mekanizmasının üzerine yeni bir IH mekanizması tanıtırken, bu mekanizmanın hasatlanan enerji, ulaşılabilir hızlar ve güvenilirlik açısından faydalarını araştırmaktadır.

Son olarak, Beşinci Bölüm, bir bağımsız RIS'in düşük güçlü bir RIS yapısı üzerinden WEH'ye dayalı olarak işlevlerini sürdürdüğü yeni bir SR sistemi sunar. Karşılıklı simbiyoz, birincil verici (PTx) tarafından iletilen bir sinyalin sürekli iletilen iletimlere yardımcı olmak ve birincil alıcıya (PRx) bilgi aktarmak için kullanılmasıyla kurulur. PTx, bilgiyi PRx'e ve RIS'e iletim için zaman indisi modülasyonu (TIM) kullanırken, RIS ve enerji toplayıcıya (EH) güç sağlamaktadır. TIM şemasındaki zorlukları ele almak için bir log-olasılık oranı (LLR) tabanlı dedektör sunulmaktadır. Son olarak, önerilen şemanın RIS ve EH'de hasatlanan direkt akım (DC) gücü ile PRx'de BER açısından performansı araştırılmıştır.

ACKNOWLEDGMENTS

I wholeheartedly express my gratitude to my advisor, Assoc. Prof. Ertuğrul Başar, for guiding me on my academic journey. Under his mentorship, I not only expanded my comprehension of my research field but also gained invaluable life and academic insights. I am grateful and honored to have been mentored by such an esteemed advisor.

I extend heartfelt appreciation to Dr. Mehmet Çağrı İlter for his significant contributions to my academic development. His ideas consistently inspired me and enhanced the quality of my research. It has been a privilege to shape my academic endeavors through his insightful feedback.

I owe immense gratitude to my motivating father, Kazım, whose encouragement and positivity have always uplifted me throughout this journey. I am deeply thankful to my caring mother, Nevin, who has been my unwavering source of support. I am incredibly fortunate to have my lovely sisters, Güzin and Nevsun, whose emotional and material help have been invaluable.

Lastly, I wish to express my heartfelt thanks to the wonderful friends and collaborative members of CoreLab. The genuine friendship from the members of CoreLab truly made my time in the lab enjoyable.

TABLE OF CONTENTS

LIST OF TABLES

LIST OF FIGURES

ABBREVIATIONS

6G	Sixth Generation
AmBC	Ambient Backscatter Communications
AN	Artificial Noise
ASK	Amplitude Shift Keying
AWGN	Additive White Gaussian Noise
BC	Backscatter Communications
BER	Bit Error Rate
CLC	Constant Linear Constant
CPEP	Conditional Pairwise Error Probability
CSI	Channel State Information
CSCG	Circularly Symmetric Complex Gaussian
CW	Continuous Wave
DAC	Digital-to-Analog Converter
DC	Direct Current
EH	Energy Harvester
EIRP	Effective Isotropic Radiated Power
ESR	Ergodic Secrecy Rate
FSK	Frequency Shift Keying
GQSM	Generalized Quadrature Spatial Modulation
GQSSK	Generalized Quadrature Space Shift Keying
GQSSK	Generalized Quadrature Space Shift Keying
GSM	Generalized Spatial Modulation
GSSK	Generalized Space Shift Keying
IH	Information Harvesting/Harvester
IM	Index Modulation

IoT	Internet of Things
IR	Information Receiver
LLR	Log-Likelihood Ratio
ML	Maximum Likelihood
MU-SWIPT	Multi-User Simultaneous Wireless Information and Power Transfer
OFDM	Orthogonal Frequency Division Multiplexing
OFDM-IM	Orthogonal Frequency Division Multiplexing with Index Modulation
PAPR	Peak to Average Power Ratio
PDF	Probability Density Function
PLS	Physical Layer Security
PRx	Primary Receiver
PTx	Primary Transmitter
QAM	Quadrature Amplitude Modulation
QSM	Quadrature Spatial Modulation
QSSK	Quadrature Space Shift Keying
RF	Radio Frequency
RFI	Request for Information
RFID	Radio Frequency Identification
RIS	Reconfigurable Intelligent Surfaces
SLIPT	Simultaneous Light-Wave Information and Power Transfer
SM	Spatial Modulation
SR	Symbiotic Radio
SSK	Space Shift Keying
STx	Secondary Transmitter
SVD	Singular Value Decomposition
SWIPT	Simultaneous Wireless Information and Power Transfer
TIM	Time Index Modulation
TS-SWIPT	Time Switching Simultaneous Wireless Information and Power Transfer
UC	Unit Cell

WIT	Wireless Information Transfer
WPCN	Wireless Powered Communication Networks
WPT	Wireless Power Transfer
WPTx	Wireless Power Transmitter

Chapter 1

INTRODUCTION

In the sixth generation (6G) era, Internet-of-things (IoT) platforms are required to support a massive number of devices and to tackle energy demands in addition to existing challenges in data transmission. In this respect, existing discussions in standardization frameworks are underway in ambient IoT scenarios [Zhang and Long, 2022], where IoT devices are able to harvest ambient energy from external sources. In this direction, zero-power communication technology [Naser et al., 2023] has been emerged as the next logical step in future networks and promises information transmission where its energy is harvested from surrounding radio frequency (RF) energy, thus reducing the need for replacing batteries [Liu et al., 2022]. To reach greater sustainability and environmentally friendly architectures, the synergistic integration of various frameworks connecting energy harvesting with communication infrastructure appears to be an inevitable development in the near future.

In RF energy harvesting systems, the concept of wireless-powered communication networks (WPCN) was initially introduced to reduce the operational burden associated with battery replacement/recharging [Bi et al., 2016]. In WPCN, network elements first harvest energy from signals transmitted by RF energy sources and then utilize this harvested energy for their upcoming communication periods. Over the last decade, the concept has evolved to include data communication within wireless power transfer, known as simultaneous wireless information and power transfer (SWIPT) for RF-based mechanisms [Ponnimbaduge Perera et al., 2018]. More recently, a similar approach has been introduced for optical-based systems, termed simultaneous light information and power transfer (SLIPT) [Uysal et al., 2021]. In these systems, the power and information components are primarily separated across different domains: the power domain (power splitting), time domain (time switching), and space domain (antenna splitting) [Liu et al., 2016]. This separation introduces a trade-off between information transfer and energy transfer, dependent on the design preferences for data and power transmission, as extensively investigated in existing literature [Amarasuriya et al., 2016]. SWIPT studies are also found in commercial RFID systems, particularly in communication from reader to RFID tags [Paolini et al., 2022]. Furthermore, the SWIPT mechanism has been extended into multi-user scenarios, known as multi-user (MU)-SWIPT, where a multi-antenna transmitter simultaneously transmits wireless information and energy through spatial multiplexing to multiple single-antenna receivers [Xu et al., 2014].

It is essential to consider that most devices are simple nodes, i.e., RedCap devices [Veedu et al., 2022], operating at a level of several kbps with limited computational capabilities. For these devices, the SWIPT mechanism might be impractical in real-world scenarios due to distinct device requirements, particularly in ensuring secure data transmission alongside a far-field wireless power transfer (WPT) mechanism in simple devices. The findings in [Xu and Zhu, 2019] illustrate a significant drop in power transfer efficiency over transmission distance in such systems when incorporating security enhancements for information transmission into the design. In response to this limitation, a distributed antenna-based SWIPT protocol was proposed in [Huang et al., 2018]. Additionally, in [Krikidis and Psomas, 2019], information bits are embedded in the tone index of multi-sine waveforms as an alternative solution. Another approach involves creating a modulation signal within a vacant resource block of communication in an orthogonal frequency division multiplexing (OFDM) block, as introduced in [Nakamoto et al., 2022].

Accordingly, there is a demand for further solutions to prevent the potential interception of confidential information by unintended users. While conventional encryption techniques prove valuable in many instances for securing data transmission, there are specific use cases or protocols where implementing additional encryption is not feasible [Wang et al., 2019]. In this aspect, artificial noise (AN)-based physical layer security (PLS) techniques [Goel and Negi, 2008] turned into a powerful tool due to its ability to generate orthogonal noise through the channel state information

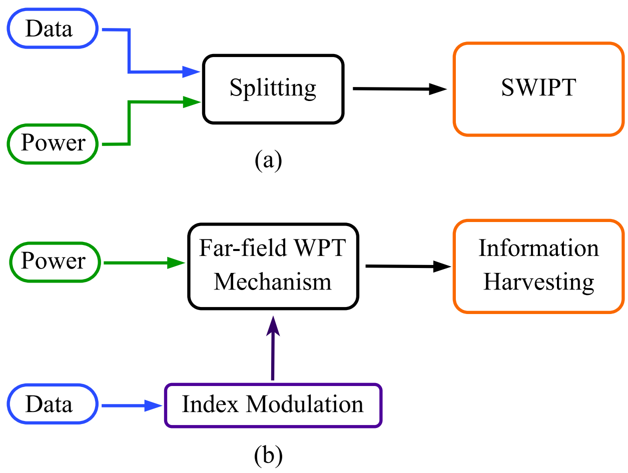

Figure 1.1: The design aspects of (a) SWIPT and (b) Information Harvesting [Ilter et al., 2022b] mechanisms which show how data and power parts are integrated together.

between the transmitter and intended receiver. Considering its advantages against eavesdropping, the AN technique has been applied to multiple-input single-output (MISO) [Lv et al., 2018] and multiple-input multiple-output (MIMO) systems [Gu et al., 2019].

To address the efficiency losses in power transfer and to handle implementation concerns arising from differing sensitivities between the energy harvester and the data recipient, an alternative approach was proposed in [Ilter et al., 2022b]. This novel scheme, *Information Harvesting (IH)*, presented in Chapter 3, enables information transfer without disrupting the ongoing far-field WPT mechanism between the power transmitter and the energy harvester. Figure 1.1 compares the IH mechanism with SWIPT and depicts how the IH technique utilizes the existing far-field WPT mechanism to enable WIT through dedicated WPT waveforms. In the IH mechanism, WIT is achieved by injecting information into the indices of transmitter entities using index modulation (IM) schemes. This strategy contrasts with the SWIPT approach, which either employs different signaling schemes at the transmitter side or splits the received signal into various domains to deliver information and power to the intended receiving ends. Notably, the IH mechanism does not divide signals into different domains; instead, it distributes the total power among the active transmit antennas through the distinctive feature of IM schemes. This characteristic makes the IH mechanism adequate for extending the service area of the far-field WPT mechanism, overcoming the power transmission range challenge, which is a common limitation in SWIPT systems. Another superiority of the IM-based IH lies in its reduced pilot overhead since the MU-SWIPT system necessitates the channel state information (CSI) of both the information receiver (IR) and the energy harvester (EH) links. In contrast, the IH systems do not require CSI of the EH link, potentially leading to a reduced pilot overhead for channel estimation. The generalized space shift keying (GSSK)-based IH mechanism and its performance in terms of secrecy capacity and average harvested power was first investigated in [Ilter et al., 2022a]. Then, [Ilter et al., 2023] introduced a new IH mechanism that relies on quadrature spatial modulation (QSM).

Earlier far-field WPT studies did not integrate OFDM-based solutions since they were mainly limited to strong, non-dispersive, short-range channels. Then, considering its high peak-to-average-power ratio (PAPR) characteristics resulting in high energy conversion efficiency [Boaventura et al., 2015], OFDM-based wireless power transfer was investigated in [Nasir et al., 2020, Nasir et al., 2022]. Within this direction, [Nakamoto et al., 2022] considered a joint information and power transmission mechanism where Zadoff-Chu sequences are adopted as WPT signals due to their small PAPR value under OFDM transmission. In the context of OFDM-SWIPT systems, a hybrid time switching/power-splitting scheme was proposed in [El Shafie et al., 2017], where a cyclic prefix was utilized for generating artificial noise as well as for energizing the legitimate receiver. Also, [Buckley and Heath, 2021] introduced a novel architecture to extract the cyclic prefix (CP) of the signal for energy harvesting and selectively harvest a fraction of the received signal to increase energy capability.

Motivated by the existing interest on OFDM-based power transfer, Chapter 4 introduces the implementation of IH concept [Ilter et al., 2022b] into an OFDM-based far-field power transfer mechanism after utilizing OFDM with index modulation (OFDM-IM) structure. To do so, a novel data transmission mechanism on top of OFDM-based far-field power transmitter has been implemented, where information transmission is carried out through an active OFDM subcarrier set that emits WPT waveforms. The benefits of the proposed mechanisms are investigated from the energy harvester's and information receiver's perspectives in terms of harvested energy amount, achievable rate, and error performance, respectively. Besides, dual-mode OFDM-based IH is also introduced where all subcarriers are active with two different waveforms. The presented results validates the superiority of the OFDM-based IH in energy harvesting capability compared to a time splitting (TS)-based SWIPT mechanism [Buckley and Heath, 2021] where some parts of the data frame have been used for energy harvesting in addition to the cyclic prefix. In this respect, the presented results highlight the substantial potential of OFDM-based IH mechanism for enabling data communication in far-field power transfer scenarios.

The integration of wireless energy harvesting (WEH) into future IoT architectures is increasingly vital as the coexistence between cellular and IoT devices demands additional energy resources to support the growing number of connected devices. In order to address rising demand, symbiotic relationships among cellular and IoT devices have been discovered, whereby the passive transmission capabilities of IoT devices leverage the power and spectrum resources of active transmission technology used by cellular devices. The concept, known as symbiotic radio (SR), has been introduced to enable energy- and spectrum-efficient communications within the network [Liang et al., 2020].

Similar to SR, IoT devices can utilize ambient backscatter communications (AmBC) by leveraging existing ambient RF signals in the environment. However, AmBC suffers from direct link interference from surrounding ambient RF signals, which limits detection performance at the target receiver [Long et al., 2020]. Contrary to AmBC, the SR concept forms a novel architecture in which active and passive systems rely on mutualistic communication through joint decoding at the receiver and an additional link provided by a backscatter device (BD) rather than parasitic communication, which is a drawback of AmBC [Liang et al., 2020]. In the SR framework, the primary transmitter (PTx) shares its energy and spectrum resources with the secondary transmitter (STx). Meanwhile, STx operates as a passive device that also transmits its information to primary receiver (PRx) by manipulating the resources of PTx. To establish mutualistic symbiosis, the PTx maintains a higher transmission rate than the PRx, which means the symbol duration of the STx is longer than that of PTx [Long et al., 2020]. In [Zhang and Long, 2022], the authors reveal that the mutualistic condition depends on the average strength of direct and backscatter links, and [Liang et al., 2020] mentions that the backscatter link can be improved by utilizing reconfigurable intelligent surfaces (RISs). The RIS-aided SR system has recently introduced in [Yang et al., 2024], where the RIS performs two functions simultaneously: assisting PTx transmission and transmitting its information by orchestrating the phase shifts on the incident signals.

Specifically, RISs are passive devices consisting of N unit cells (UCs) that operate as reflectors to manipulate the wireless channel by tuning the phase of the reflected signal [Basar et al., 2019]. RIS UCs are tunable devices equipped with PIN diodes, varactors, and RF switches, that control the wireless medium and enable the reflection function. Nevertheless, UCs can also be operated as absorbers for WEH on the RIS. In [Petrou and Georgiou, 2022], a novel RIS controller architecture, called integrated architecture, is discussed to form a low-power RIS setup. Based on this integrated architecture, WEH protocols for self-sustainable operations are explored in [Ntontin et al., 2024], assuming perfect absorbers with no reflected signals caused by the RIS. To achieve a self-sustainable architecture, the harvested direct current (DC) power on the RIS should be at least equal to its total power consumption. Although the integrated architecture provides lower power consumption than conventional RIS controllers, the type of UCs can make self-sustainable operations infeasible if varactor-based UCs are employed, as they are driven by power-hungry digital-to-analog converters (DACs). The authors examined the power consumption of various UCs and claimed that it is possible to design an RF switch-based RIS without DACs [Wang et al., 2024]. An RF switch-based RIS prototype was designed, demonstrating that by connecting one port of the RF switch to the absorber, WEH can be achieved on RIS [Rossanese et al., 2022].

IM can map information bits by altering the on/off status of transmission entities in a communication system, such as transmit antennas and subcarriers [Basar et al., 2017]. This distinctive feature enables the integrated transfer of power and information by means of IM. To facilitate data transfer and wireless energy harvesting (WEH) efficiently, a time index modulation (TIM) technique that employs time slots to convey additional information is presented in [Zhao et al., 2023]. In [Basar et al., 2013], an orthogonal frequency division multiplexing (OFDM)-IM scheme is proposed by inactivating some subcarriers, and its performance under the low-complexity log-likelihood ratio (LLR) detector is investigated. Furthermore, [Mao et al., 2016] presents a dual-mode OFDM-IM system by replacing inactive subcarriers with a different constellation set from those used in active ones. Building upon the concept introduced in [Ilter et al., 2022b], a novel OFDM-based information harvesting concept is proposed in [Ilter et al., 2024], where OFDM-IM is applied to an ongoing wireless power transfer mechanism. [Lin et al., 2021] proposes an RIS-based IM scheme in which the indices of the activated group of RIS UCs are utilized to convey environmental data collected by RIS. To prevent power loss caused by inactivating a group of RIS UCs, partitioning the RIS UCs into two orthogonal groups is proposed in [Lin et al., 2022].

1.1 Contributions

Chapter 3 presents the IH architecture within a unified framework, encompassing a variety of IM techniques. Our investigation focuses on evaluating the feasibility of these techniques and establishing unified performance criteria. We conduct a comprehensive evaluation of IM-based IH mechanisms, considering both space shift keying-based techniques with no modulated symbol and spatial modulation ones. Rather than concentrating solely on specific performance metrics, we introduce a more comprehensive approach to performance evaluation, analyzing various IM-based IH mechanisms in terms of their energy harvesting capability, bit error rate, and ergodic secrecy rate to offer valuable insights. Additionally, we introduce a unified framework to calculate the theoretical error performance of the proposed schemes. The simulated results are validated using analytical expressions for the BER of the proposed IM-based IH mechanisms. We demonstrate the advantages of IM-based IH mechanisms, particularly for far-field WPT range, compared to existing SWIPT mechanisms, along with other practical advantages.

In Chapter 4, we implement the IH concept [Ilter et al., 2022b] into an OFDM-based far-field power transfer mechanism using OFDM-IM structure. We propose a novel data transmission mechanism on top of an OFDM-based far-field power transmitter, where information transmission occurs through an active OFDM subcarrier set emitting WPT waveforms. We investigate the benefits of the proposed mechanisms from the perspectives of the energy harvester and the information receiver in terms of harvested energy amount, achievable rate, and error performance, respectively. Furthermore, we introduce dual-mode OFDM-based IH, where all subcarriers are active with two different waveforms. Our results validate the superiority of OFDM-based IH in energy harvesting capability compared to a TS-based SWIPT mechanism [Buckley and Heath, 2021]. We highlight the substantial potential of the OFDM-based IH mechanism for enabling data communication in far-field power transfer scenarios.

Chapter 5 presents a novel TIM-driven SR environment empowered by a standalone RIS architecture. This architecture utilizes an integrated controller to reduce the power consumption of the RIS and employs 2-bit resolution RF switches as UCs to eliminate power-hungry DACs, promoting sustained functionality through WEH. Consequently, the RIS operates as a BD in the SR environment by applying WEH initially, assisting the PTx transmission strategy, and conveying RIS information by inducing phase shifts selected from a discrete set. Additionally, PTx implements the TIM scheme to power the RIS and EH while ensuring reliable communication with the PRx. We propose an log-likelihood ratio (LLR)-based detector tailored for the TIM-based SR scheme within our framework to address decoding challenges.

As a result, this thesis and the corresponding works aim to present novel system designs for future wireless communication systems that utilize wireless power transfer to achieve greater sustainability through 6G. This thesis illustrates that combining emerging paradigms of next-generation communication systems with RF energy harvesting addresses the rising power demands, especially for IoT networks, as these simple devices will be deployed everywhere for more intelligent operations in the near future. Even though they are not sophisticated, IoT connectivity demands reliable and sustainable communications, and this thesis presents the potential to meet the requirements for ubiquitous connectivity.

This thesis has contributed to the existing literature with three journal papers: *"Index Modulation-based Information Harvesting for Far-Field RF Power Transfer,"* published in IEEE Transactions on Wireless Communications; *"OFDM-based Information Harvesting,"* published in IEEE Communications Letters; and *"Time Index Modulation-Driven Standalone RIS Mechanism for Symbiotic Radio,"* submitted to IEEE Internet of Things Journal.

1.2 Notations

Italic letters x denote scalar values, while lowercase $\mathbf{x}$ and uppercase $\mathbf{X}$ in boldface represent vectors and matrices, respectively. The superscripts $(\cdot)^T$ and $(\cdot)^H$ denote the transpose and the Hermitian transpose operations, respectively. $\angle\cdot$, $|\cdot|$, and $\|\cdot\|$ denote the angle, absolute value, and the norm of a vector/matrix, respectively. $\log_a(\cdot)$ represents the logarithm with base a. The operator $\mathbb{E}[\cdot]$ indicates averaging/statistical expectation, and $\mathbb{E}\mathbf{x}[\cdot]$ is the statistical expectation with respect to the random variable x. $\Pr(\cdot)$ represents the probability of an event. $\lceil\cdot\rceil$ and $\lfloor\cdot\rfloor$ denote the ceil and floor operations, respectively. The symbol j represents the imaginary unit $\sqrt{-1}$, while I and Q denote a complex symbol's in-phase and quadrature parts, respectively. $\mathcal{CN}(\mu, \sigma^2)$ represents a circularly symmetric complex Gaussian (CSCG) random variable with mean μ and variance σ^2. The set of complex matrices of dimensions $m \times n$ is denoted by $\mathbb{C}^{m\times n}$, the set of non-negative integers of dimensions $m\times n$ is denoted by $\mathbb{N}^{m\times n}$, and $\mathbb{Z}^+$ denotes the set of integers greater than zero. The binomial coefficient is denoted by $C(n, k)$. The $\mathbf{0}_{n\times m}$ denotes the all-zero matrix of size $n \times m$. $\mathcal{Q}(x)$ represents the Q-function. $\Re\{\cdot\}$ and $\Im\{\cdot\}$ denote the real and imaginary parts, respectively.

Chapter 2

EMERGING TECHNOLOGIES FOR FUTURE WIRELESS COMMUNICATION SYSTEMS

This chapter presents a literature review and highlights some fundamental aspects of promising technologies for future wireless communication architectures. First, wireless power transfer (WPT) is introduced, and a nonlinear rectenna model is explained. Subsequently, index modulation (IM), backscatter communication (BC), and reconfigurable intelligent surfaces (RIS) are discussed.

2.1 Wireless Power Transfer

The origin of WPT can be traced back to the seminal work of N. Tesla [Tesla, 1904]. His idea was based on radiating the energy through a medium (i.e., air) with the help of antenna elements. Nowadays, the WPT has been extensively studied for RF signals [Valenta and Durgin, 2014, Gu et al., 2021] and for visible light communications [Pan et al., 2019], which is an emerging 6G paradigm. The WPT can be broadly classified into two primary categories: near-field and far-field. Near-field WPT involves power transfer over short distances through magnetic fields using inductive coupling or electric fields between the energy harvester and the power transmitter, which is beyond the scope of this thesis. On the other hand, far-field WPT leverages dedicated or ambient RF signals in the surrounding indoor or outdoor environment. Ambient WPT results from existing RF transmission and is coupled with backscattering techniques. Far-field WPT serves as an advantageous and sustainable power source for longer ranges [Clerckx et al., 2018]. In this aspect, the far-field WPT introduces viable solutions to tackle the battery depletion problem for wireless nodes/devices since RF energy harvesting allows wireless nodes to scavenge energy from the environment without tethering to electricity grids or requiring

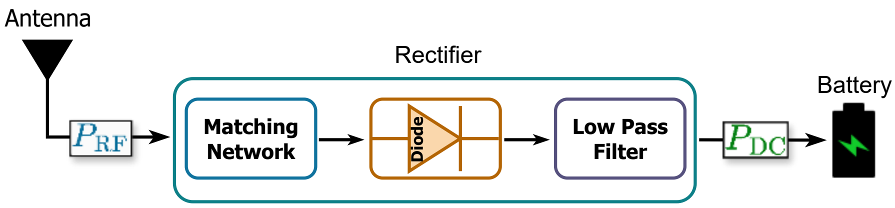

Figure 2.1: A single diode rectenna model.

battery replacement, particularly in hazardous and inaccessible environments [Ku et al., 2016]. Thus, WPT is an emerging technology for various applications, including remote environmental monitoring, consumer electronics, biomedical implants, building/home automation, and logistics solutions [Leemput et al., 2023].

In the far-field RF power transfer, one of the crucial focuses has been enhancing the RF-to-DC conversion efficiency of a rectenna, a combination of a rectifier and an antenna, serving as a key element in energy harvesting systems. Accordingly, developing efficient rectennas has been a longstanding focus in the literature [Clerckx et al., 2018]. These investigations have highlighted the significance of tailoring rectenna designs to match precise operating frequencies and input power levels, thus posing a significant challenge due to the inherent nonlinear characteristics in practical rectenna implementations [Costanzo and Masotti, 2016].

In Fig. 2.1, a single diode rectenna model is depicted. Therein, a matching network is used for matching the antenna impedance to the input impedance of the rectifier. Subsequently, the rectenna first harvests ambient energy, then rectifies and filters it. The scavenged DC power then either powers a low-power device directly or is stored in a super-capacitor or battery. Assuming that all signaling schemes used in WPT are normalized to the same average power, the harvested DC power should be the same for all. However, it has been shown that the efficiency of RF energy harvesting also depends on the choice of a selected WPT waveform at the power transmitter, in addition to rectenna design [Clerckx et al., 2019]. For instance, it has been demonstrated that deploying multitone waveforms enhances the efficiency of RF-to-DC conversion, thereby increasing the output DC power in

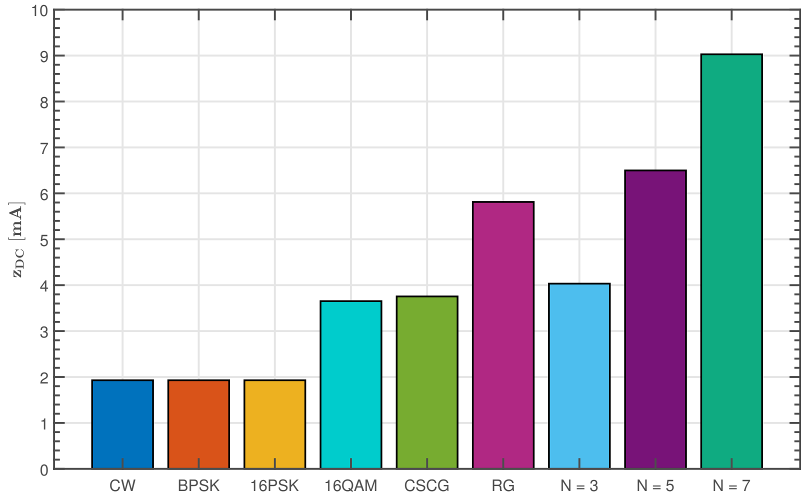

Figure 2.2: Response of various signaling schemes to the nonlinear rectenna model.

flat-fading channels [Shen and Clerckx, 2021b]. Aside from grid-based and lattice-based constellations used in conventional communication systems where low PAPR is typically desired due to nonlinearity in power amplifiers, real Gaussian (RG) signals, flash signaling, and linear frequency-modulated signals are preferred in earlier far-field power harvesting mechanisms [Clerckx et al., 2018] at the cost of higher complexity and power consumption in the transmitter due to their higher PAPR. Interestingly, the effects of different modulation techniques, such as amplitude shift keying (ASK), quadrature amplitude modulation (QAM), phase-shift keying (PSK), and frequency shift keying (FSK) on battery charging time, are measured and theoretically analyzed in [Cansiz et al., 2020].

The nonlinear characteristic of the rectenna is analyzed in [Clerckx et al., 2019] by examining the impact of various signaling schemes on RF energy harvesting using the Taylor series expansion of the diode characteristic function, which can be expressed as follows:

$$z_{dc} = \underbrace{k_2 R_{\text{ant}} \mathbb{E}[|y(t)|^2]}_{\text{linear part}} + \underbrace{k_4 R_{\text{ant}}^2 \mathbb{E}[|y(t)|^4]}_{\text{nonlinear part}}. \tag{2.1}$$

where k_2 and k_4 represent the rectifier-dependent parameters, and R_{ant} denotes the antenna impedance.

Although the average power is assumed to be the same for all types of waveforms, their response to (2.1) varies due to the fourth-order moment, which accounts for nonlinearity [Clerckx et al., 2019]. Fig. 2.2 illustrates the response of different signaling schemes to the nonlinear rectenna model. First, comparing PSK with QAM, it can be observed that the performance of QAM is better than PSK since it induces amplitude fluctuations that boost the RF-to-DC conversion efficiency of the nonlinear rectenna. There is a performance gap between conventional modulations used for communications, such as BPSK, QAM, and Circularly Symmetric Complex Gaussian (CSCG), and waveforms designed for WPT, such as RG and multitone signals with parameter N, which refers to the number of tones. These waveforms are characterized by a high PAPR. It is important to note that multitone signals are deterministic and, therefore, unsuitable for WIT, though their energy harvesting performance outperforms that of conventional modulations [Kim et al., 2020].

2.2 Index Modulation

Spatial modulation (SM) was first proposed in the inspiring work by R. Mesleh [Mesleh et al., 2008]. The idea behind SM is to create a novel domain called the spatial domain to convey additional information bits by altering the on/off status of the transmit antennas. Inactivating transmit antennas of communication systems brings advantages such as increased energy efficiency and reduced decoding overhead due to the sparse nature of the transmit vector [Basar et al., 2017]. This distinctive feature has subsequently been applied to various entities of a communication system. Inspired by SM, [Basar et al., 2013] transmits additional bits by inactivating some OFDM subcarriers. [Li et al., 2016] introduced a novel scheme called virtual spatial modulation (VSM), utilizing virtual parallel channels to send index modulation (IM) bits. Additionally, time index modulation, presented in Zhao et al. [Zhao et al., 2023], indexes the transmission order of M-ary modulated symbols in a block that spans L time durations for integrated energy and data transfer.

Now, we briefly introduce the working principle of a variant of SM called quadrature spatial modulation (QSM). Moreover, this thesis investigates many IM techniques, and novel system models are presented.

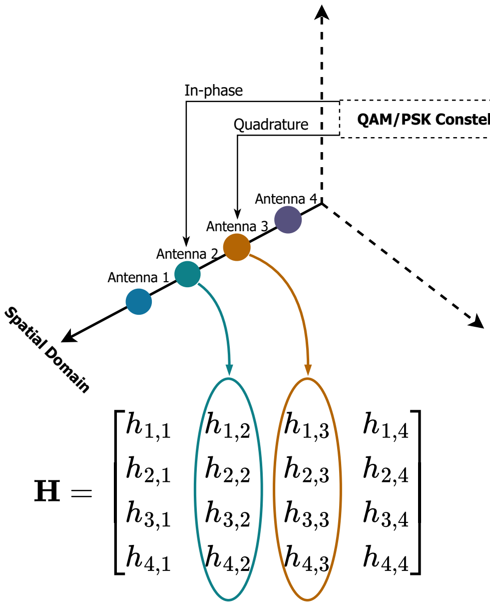

Figure 2.3: Antenna selection of QSM with $N_T = N_R = 4$ for the bit sequence 100110.

Let both the modulation order M and the number of transmit antennas N_T be 4. Assuming the bit sequence $\begin{bmatrix}1 & 0 & 0 & 1 & 1 & 0\end{bmatrix}$ is to be transmitted. In quadrature spatial modulation (QSM), the first $\log_2(M)$ bits select the symbol x from the QAM/PSK constellation diagram, corresponding to $(-1+j)$ in a 4-QAM constellation. The selected symbol is then divided into its real ($x_{\Re}$) and imaginary ($x_{\Im}$) parts. One transmit antenna is used to transmit the real part, $x_{\Re}$, of the symbol, while another transmit antenna is utilized to transmit the imaginary part, $x_{\Im}$ [Mesleh et al., 2015]. Subsequently, the real part is determined by the first $\log_2(N_T)$ bit sequence $\begin{bmatrix}0 & 1\end{bmatrix}$, corresponding to the antenna index $i_{\Re} = 2$, and the imaginary part is determined by the last $\log_2(N_T)$ bit sequence $\begin{bmatrix}1 & 0\end{bmatrix}$, corresponding to the antenna index $i_{\Im} = 3$. The resulting vector can be expressed as the sum of two transmit vectors, which is given by:

$$\mathbf{s} = \mathbf{s}_{\Re} + \mathbf{s}_{\Im} = \begin{bmatrix}0 & -1 & 0 & 0\end{bmatrix}^T + \begin{bmatrix}0 & 0 & j & 0\end{bmatrix}^T = \begin{bmatrix}0 & -1 & j & 0\end{bmatrix}^T \tag{2.2}$$

Subsequently, the signal is transmitted over the channel $\mathbf{H} \in \mathbb{C}^{N_R \times N_T}$, where N_R is the number of receive antennas. The received signal can be expressed as follows:

$$\mathbf{y} = \mathbf{H}\mathbf{s} + \mathbf{n} = \mathbf{H}(\mathbf{s}_{\Re} + \mathbf{s}_{\Im}) + \mathbf{n} = \mathbf{h}_{i_{\Re}} x_{\Re} + j\mathbf{h}_{i_{\Im}} x_{\Im} + \mathbf{n}, \tag{2.3}$$

where $\mathbf{n}$ is the additive white Gaussian noise (AWGN) sample vector, which has a row length of N_R and $\mathbb{E}[|x|^2] = 1$. It is worth mentioning that indexing antennas means selecting the columns of the channel matrix $\mathbf{H}$ to send IM bits, with the columns of $\mathbf{H}$ acting as random constellation points [Jeganathan et al., 2008], which is also depicted in Fig. 2.3. Moreover, QSM can work only for N_T being a power of two integers, similar to SM [Mesleh et al., 2015].

Assuming the perfect CSI is available at the receiver, the indices of antennas as well as the real and imaginary parts of the symbols can be estimated using the maximum likelihood (ML) detector by minimizing the following metric,

$$\left(\hat{i}_{\Re}, \hat{i}_{\Im}, \hat{x}_{\Re}, \hat{x}_{\Im}\right) = \arg \min_{i_{\Re}, i_{\Im}, x_{\Re}, x_{\Im}} \|\mathbf{y} - (\mathbf{h}_{i_{\Re}} x_{\Re} + j\mathbf{h}_{i_{\Im}} x_{\Im})\|^2. \tag{2.4}$$

Moreover, the diversity gain of the QSM system is directly related to the number of receive antennas and is equal to N_R [Mesleh et al., 2015].

2.3 Backscatter Communication and Symbiotic Radio

A transmission strategy of backscatter communications (BC) exploits the RF signals in the environment to convey information by means of reflection modulation. Thus, the backscatter transmitter uses the received signal sent by dedicated or non-dedicated sources without generating any RF signal for communication such that a BC transmitter does not require active RF components. Reflection modulation is achieved by tuning the antenna impedance to embed information into the received signal. Specifically, the backscatter transmitter embeds its information on RF signals by altering the states of the load impedance of the antenna, which is called load modulation [Van Huynh et al., 2018]. The reflection coefficient of the antenna is given by

$$\alpha_i = \frac{Z_{L,i} - Z_a^*}{Z_{L,i} + Z_a}, \tag{2.5}$$

where Z_a is the antenna impedance, and $i = 1, 2$ represents the switch state. Two states called absorbing and reflecting states can be utilized at the backscatter transmitter by switching between two loads, $Z_{L,1}$ and $Z_{L,2}$. In the absorbing state, i.e., impedance matching, RF signals are absorbed, and this state represents bit '0'. Correspondingly, the received signal power at the receiver is P. In the reflecting state, i.e., impedance mismatching, the RF signals are reflected, and this state represents bit '1'. Correspondingly, the received signal power at the receiver is $|1+\alpha|^2 P$ [Van Huynh et al., 2018].

The first variant of BC is known as monostatic backscatter communication (MsBC). Its origin goes back to World War II when radar transmitted an RF signal, and the backscatter from an oncoming airplane was used to identify it as "friend or foe" [Wang et al., 2016]. Currently, MsBC can be found in RFID devices. A conventional RFID system consists of a reader and a tag. The reader generates an RF signal through its RF source, and the tag first harvests energy, then modulates the received signal and reflects it to the reader [Boyer and Roy, 2014]. Since the same RF signal is first transmitted to the tag and reflected to the reader, this system suffers from round-trip path loss, which limits the range of communication. Thus, MsBC is mainly used for short-range RFID applications.

To overcome the limits of MsBC, bistatic backscatter communication (BsBC) has been proposed [Kimionis et al., 2014], where the RF source is separated from the reader to increase the range of BC. In BsBC, the tag harvests energy from the signal transmitted by the RF source; subsequently, it modulates the signal in a backscatter manner to send it to the reader. Since the RF source is separated, the power consumption, size, and complexity of the reader are less than those of MsBC. Moreover, by placing RF sources in close proximity to the tag, the path loss can be reduced significantly [Van Huynh et al., 2018].

The idea of replacing dedicated RF sources with ambient RF sources has led to the discovery of a novel BC scheme called ambient backscatter communication (AmBC) [Liu et al., 2013]. Exploiting ambient RF signals for BC, such as FM base stations, cellular, and Wi-Fi, offers significant advantages in terms of the deployment cost of RF sources as in BsBC and spectrum resources [Van Huynh et al., 2018]. However, exploiting modulated signals in AmBC causes severe direct link interference by ambient RF sources, which limits the detection performance of BC [Liang et al., 2020].

The symbiotic radio (SR), also known as cooperative AmBC, is introduced in [Liang et al., 2020] to address the limitations of AmBC. The term symbiotic describes the cooperative association among wireless devices. While AmBC typically involves interfering spectrum sharing, the SR concept aims for mutualistic spectrum sharing. Thus, SR establishes a cooperative relationship rather than a parasitic one found in AmBC. To achieve this, the ambient RF source, known as the primary transmitter (PTx), collaborates with a backscatter device (BD) called the secondary transmitter (STx). Initially, PTx shares its spectrum and energy resources with STx, which then exploits these resources. Subsequently, STx sends its information by modulating the signal with a reflection coefficient while enhancing the signal of PTx. Ultimately, highly reliable BC is achieved at the target receiver, the primary receiver (PRx), through joint decoding of information from both PTx and STx [Long et al., 2020].

2.4 Reconfigurable Intelligent Surfaces

The wireless medium presents significant challenges to communication signals. Energy loss occurs due to material absorption and free-space propagation. Most importantly, these signals are subject to multipath effects caused by scattering, diffraction, and reflection, which yield constructive or destructive interference at the received signal. Therefore, multiple copies of the signal can arrive at the receiver in different phases, and the highly probabilistic nature of the wireless channel can degrade communication. To mitigate these challenges, RISs are emerging as a promising solution by tailoring the unknown wireless channel. RISs comprise N reflectors, known as elements or unit cells (UCs), capable of coherently aligning the phase of the reflected signals to change a random wireless channel into a deterministic one [Basar et al., 2019].

Since passive RIS architectures do not employ active elements, their power consumption is lower than that of relays. The power consumption of RIS includes the power required by its controller, the type of UCs, and the UC drive mechanism. In [Wang et al., 2024], the power consumption model for various RIS structures that employ PIN diodes, varactors, and RF switches is derived, indicating that different RIS structures exhibit varying power consumption characteristics. The idea of replacing bulky and power-consuming conventional RIS controllers with a novel, very low-power mechanism called integrated architecture, in which each controller in the integrated architecture can control only a few UCs, is proposed in [Petrou and Georgiou, 2022].

Utilizing RIS elements as absorbers instead of reflectors to enable RF energy harvesting on RIS is presented in [Abadal et al., 2020]. Moreover, [Petrou et al., 2018] has demonstrated that both reflection and absorption functions can be achieved at the same RIS. Based on the integrated architecture, authors investigated an autonomous RIS that can sustain its operations through wireless energy harvesting (WEH) in [Ntontin et al., 2023] by changing the reflection function of UCs into an absorbing state. [Tyrovolas et al., 2023] presents three energy harvesting protocols for RIS: element splitting, time switching, and power splitting, theoretically validating joint energy-data rate outage probability for base station (BS)-side RIS and user equipment (UE)-side RIS. The work [Ntontin et al., 2024] depicted that static power consumption, which is caused by the digital-to-analog converters (DACs) in varactor-based RIS, can dominate the dynamic power consumption caused by UC reconfiguration and make the perpetual condition challenging. In [Rossanese et al., 2022], an RF switch-based RIS prototype is presented, claiming that one port of the RF switch can be connected to an absorber in order to enable WEH on RIS. Consequently, the literature suggests that RIS can operate in a self-sustainable manner by utilizing strategies that achieve low power consumption and enable WEH while re-engineering the wireless medium.

Chapter 3

INDEX MODULATION-BASED INFORMATION HARVESTING FOR FAR-FIELD RF POWER TRANSFER

This chapter presents the general structure of the IM-based IH model. Various implementations in the power transmitter based on the choice of IM technique are discussed. Additionally, we investigate how the energy harvester and information receiver operate according to the selected IM technique. A unified error performance analysis is provided by deriving the average bit error rate (ABER) in both the IR and the eavesdropper (Eve). Furthermore, an ergodic capacity analysis is conducted to emphasize the effectiveness of the proposed scheme against illegitimate receivers. The feasibility of the IM-based IH mechanism is investigated through extensive simulation results and validation of the analysis.

3.1 IM-based Information Harvesting Model

The block diagram of the IM-based IH mechanism is illustrated in Fig. 3.1, where the EH and the IR are located within the service area of the wireless power transmitter (WPTx) node, along with a potential malicious node, Eve. In the initial phase, assuming successful identification and synchronization between WPTx and an EH device, WPTx, equipped with a total of N_T transmit antennas, serves as the transmitting node responsible for sending multitone WPT waveforms across N distinct subbands into the service area for RF energy harvesting. When an IR device enters the service area, WPTx aims to transmit available information blocks to the IR. This is achieved by mapping the information blocks into vectors corresponding to active transmit antennas, a process called *information seeding.* Meanwhile, the EH device, equipped with N_{EH} receive antennas, conducts recharging operations without any disruption. Notably, when the IR device enters the service area, there already exists a far-field WPT mechanism facilitated by a wireless link denoted as $\mathbf{G}_{\mathrm{EH}} \in \mathbb{C}^{N_{\mathrm{EH}} \times N_T \times N}$.

Subsequently, upon deployment, the IR device, which is equipped with N_{IR} receive antennas, initiates an information seeding cycle. This initiation is performed by transmitting a request-for-information (RFI) signal over a dedicated link represented by $\mathbf{H}_{\mathrm{IR}} \in \mathbb{C}^{N_{\mathrm{IR}} \times N_T \times N}$. The RFI signal may also include configuration parameters on the information seeding cycle, such as the frequency of changing the transmitting entity based on the required data rate within the IR and the necessity for additional PLS protocols [Ilter et al., 2022b]. Then, the information seeding process is initiated upon detecting the RFI signal at the WPTx. During this phase, the IR aims to capture variations resulting from the activation of various transmit antenna sets, which are determined by the information bits. This process is referred to as *information harvesting.* Importantly, it was demonstrated in [Ilter et al., 2022b] that activating more transmit antennas in WPTx during the power transfer period reduces the probability of detecting information seeding activity by devices located even in close proximity to the EH.

The channel entries are assumed to be independent and identically distributed (i.i.d.) according to $\mathcal{CN}(0, 1)$. Note that the channels between the WPTx and other network elements in Fig. 3.1 are assumed to be stationary, so the time dependency of the channel coefficients is emitted from the channel coefficient and weight factors in the rest of this chapter.

3.1.1 EH: Energy harvesting

During the period when the WPTx emits power transfer waveforms into a service area (regardless of the activation of information seeding cycle), the EH converts the received RF signal into DC output power thanks to its rectennas. Particularly, the EH consists of a receive antenna chain along with N_{EH} receive antennas, battery charging unit, and battery. Herein, the battery charging unit is configured to establish a link between the receive antenna chain and battery, wherein the manner in

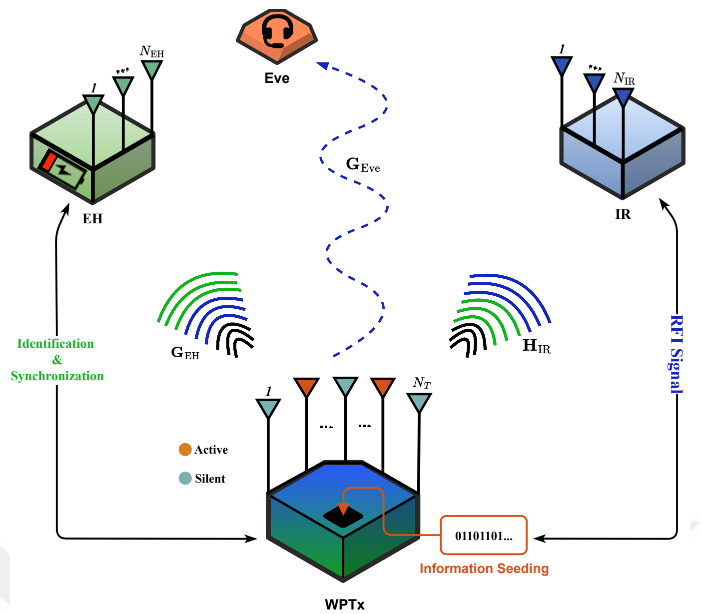

Figure 3.1: The block diagram of the IM-based IH mechanism where the WPTx serves EH while sending its information to the IR by utilizing IM techniques with the existence of Eve in a service area.

which power is transferred from the wireless power transceiver is controlled according to the parameters and/or state information assigned by the power management unit [Ilter et al., 2023].

The EH device operates in two stages: firstly, the received RF power is converted into DC power using rectennas. Note that due to the nature of the wireless medium, there exists a fraction of time where the rectenna cannot perform harvesting since input RF power lies below certain RF power that is called as *rectenna sensitivity* and after certain received signal power level at harvester, *rectenna saturation power*, the harvested energy stays constant as shown in [Alevizos and Bletsas, 2018]. After considering these practicalities as in [Clerckx et al., 2022], the output DC power for rectenna q can be formulated as a function of the received RF signal, which is,

$$v_{out,q} = \begin{cases} 0, & P_r^t \in [0, \Gamma_{in}] \\ \beta_2 P_r^t + \beta_4 P_r^{t2}, & P_r^t \in [\Gamma_{in}, \Gamma_{sat}] \\ \beta_2 \delta_{sat} + \beta_4 \delta_{sat}^2, & P_r^t \in [\Gamma_{in}, \Gamma_{sat}] \end{cases}, \tag{3.1}$$

where P_r^t is the received input power during coherence period t, $P_r^t = \mathbb{E}[|y(t)|^2]$, Γ_{in} refers the harvester sensitivity, Γ_{sat} denotes the saturation level, β_2 and β_4 are the parameters of the nonlinear rectifier model. Then, the outputs of all rectennas are aggregated to obtain the cumulative harvested DC power at the combiner's output. This technique is referred to as DC combining, as discussed in [Clerckx et al., 2022]. Then, the total DC output power can be obtained from $\sum_{q=1}^{N_{\mathrm{EH}}} v_{out,q}^2 / R_L$ where R_L refers to the resistive load used to determine the output DC power.

In the nonlinear rectenna model, the calculation of the harvested DC power is not straightforward. For this purpose, [Clerckx and Bayguzina, 2016] introduced a new technique where Taylor series expansion was applied into the nonlinear diode model. This approach provides insight into how the choices of the signal modulation or the input distributions affect the energy harvesting capability along with the configuration of the rectenna. Inspired from it the energy harvesting capability relates with a variable of z_{DC} which establishes a direct connection with (3.1) and reflects the harvested power when the signal operates within the bounds of the linear and saturation regions. Mathematically, z_{DC} is formulated as [Clerckx and Bayguzina, 2016]

$$z_{\mathrm{DC}} = k_2 R_{\mathrm{ant}} \mathbb{E}[|y(t)|^2] + k_4 R_{\mathrm{ant}}^2 \mathbb{E}[|y(t)|^4], \tag{3.2}$$

where k_2 and k_4 represent the rectifier-dependent parameters, and R_{ant} denotes the antenna impedance. In a steady-state response, an ideal rectifier maintains a constant output voltage over time, and the level of this output voltage depends on the peaks of the input voltage. Therefore, z_{DC} can be improved as the number of subbands increases in the emitted waveform from the WPTx. This enhancement is particularly associated with the generation of larger peaks facilitated by multitone signals despite their average power being equivalent to that of continuous wave (CW) signals. The impact of multitone signals, which results in the generation of larger peaks, leads to a higher PAPR. Consequently, higher PAPR enhances the efficiency of the RF-to-DC conversion process in the nonlinear rectifier, contributing to an improved energy harvesting capability. In this respect, (3.2) demonstrates a positive correlation with PAPR, suggesting that modulation schemes or input distributions characterized by higher PAPR values offer advantages to the nonlinear rectenna model [Kim et al., 2020].

3.1.2 WPTx: Information seeding

In this subsection, we discuss the integration of different IM schemes into IH mechanism along with detailed description of the information seeding cycle. IM represents a unique approach to information transmission, achieved by selectively activating specific elements for conveying information. When information seeding is initiated in WPTx alongside the specified IM scheme, the resulting set of waveforms emitted from the N_a activated WPTx antennas, obtained by combining an IM waveform at the WPTx, is as follows:

$$\mathbf{s} = \left[\frac{s_1(t)}{\sqrt{N_\mathrm{a}}}, 0, \ldots, 0, \frac{s_m(t)}{\sqrt{N_\mathrm{a}}}, 0, \ldots, 0, \frac{s_{N_\mathrm{a}}(t)}{\sqrt{N_\mathrm{a}}}\right], \tag{3.3}$$

at a given time instant t. Hereby, $s_m(t)$ is directly associated with the selection of the WPT waveform, $m \in \{1, \ldots, N_T\}$. For instance, when employing a multitone signal with N distinct subbands, the expression for $s_m(t)$ can be formulated as:

$$s_m(t) = \Re\Big\{\sum_{n=1}^{N} \omega_{n,m} e^{j2\pi f_n t}\Big\}. \tag{3.4}$$

Hereby, N represents the number of subbands of multitone WPT signals, and f_n denotes the center frequency of the nth subband waveform. More specifically, $\omega_{n,m} = a_{n,m}e^{j\theta_{n,m}}$ where $a_{n,m}$ and $\theta_{n,m}$ are the nth subband amplitude and phase components of baseband WPT signal and these values are based on the chosen IM scheme. Subsequently, the received passband signal at the IR, without the additive white Gaussian noise (AWGN) term, can be expressed mathematically, as given in [Clerckx and Bayguzina, 2016],

$$\mathbf{y}_{\mathrm{IR}}(t) = \Re\Big\{\sum_{n=1}^{N} \mathbf{G}_{\mathrm{EH},n}\mathbf{w}_n e^{j2\pi f_n t}\Big\}, \tag{3.5}$$

where $\mathbf{G}_{\mathrm{EH},n}$ is the channel between WPTx and IR for nth subband and $\mathbf{w}_n = [\omega_{n,1} \ldots \omega_{n,N_T}]^T$, where the power of $\mathbf{w}_n$, denoted as λ_s^2/N (i.e., $\mathbb{E}[\mathbf{w}_n^H\mathbf{w}_n] = \lambda_s^2/N$), is arranged in accordance with the values of N and N_a.

GSSK/SSK-based IH

In the IH mechanism based on GSSK, the available information bits are exclusively mapped into a transmit antenna vector, determining the number of active transmit antennas denoted as N_a, with the constraint $N_\mathrm{a} \leq N_T$ [Jeganathan et al., 2008], when $N_\mathrm{a} = 1$, it simplifies to the SSK-based IH mechanism. The number of information bits that can be mapped into the transmit antenna indices for GSSK modulation is given by:

$$\eta_{\mathrm{GSSK}} = \left\lfloor \log_2 \binom{N_T}{N_\mathrm{a}} \right\rfloor, \tag{3.6}$$

where $\lfloor \cdot \rfloor$ indicates floor operation. Under this assumption, the emitted WPT waveform does not contain any information components itself; instead, the antennas simply emit power transfer waveforms to the service area. From the EH perspective, there is no difference in the GSSK/SSK-based IH mechanism, as no signal modulation is employed, leading to $a_{n,m} = 1$ and $\theta_{n,m} = 0$. Note that $L = 2^\eta$ different active antenna combinations exist when N_a antennas are active out of total N_T transmit antennas, which is equal to the cardinality of the GSSK codebook.

GSM/SM-based IH

In the case of GSM-based IH, WPTx begins embedding information within the emitted symbol. This differs from the SSK-based techniques mentioned earlier, where only unmodulated WPT waveforms exist. Consequently, the number of transmitted information bits can be expressed as:

$$\eta_{\mathrm{GSM}} = \left\lfloor \log_2 \binom{N_T}{N_\mathrm{a}} \right\rfloor + \log_2 (M), \tag{3.7}$$

where M represents the modulation order of M-QAM constellation used in the WPTx. In the GSM-based IH mechanism, $a_{n,m}$ and $\theta_{n,m}$ should be configured according to the employed M-QAM. For instance, in case of 4-QAM is utilized for GSM/SM-based IH mechanism, the $a_{n,m}$ and $\theta_{n,m}$ values can be set to $\{\sqrt{2}, 7\pi/4\}$ for a bit sequence of [01] in addition to the bits mapped into active antenna indices.

GQSSK/QSSK-based IH

Quadrature-based implementations require additional signal processing before transmission to the information seeding stage. The transmitted symbols are decomposed into in-phase and quadrature components, resulting in two transmit antenna vectors. The first transmit antenna vector corresponds to the real part of a wireless power symbol, while the second corresponds to the imaginary part [Mesleh et al., 2015]. Therefore the number of information bits increases to

$$\eta_{\mathrm{GQSSK}} = 2\eta_{\mathrm{GSSK}}. \tag{3.8}$$

Assuming $s_m(t)$ is a complex WPT signal, and its the real part, $\Re\{s_m(t)\}$, and its imaginary part, $\Im\{s_m(t)\}$, are transmitted separately through the different antennas over cosine and sine carriers respectively [Mesleh et al., 2015]. In the GQSSK/QSSK-based IH mechanism, the transmitted symbol is fixed and equal to $(1+j)$. Consequently, the corresponding $a_{n,m}$ and $\theta_{n,m}$ values are $\{\sqrt{2}, \pi/4\}$.

GQSM/QSM-based IH

Similar to (3.7), now WPT signal carries the modulated symbol from M-ary constellation, and the real part modulates the in-phase part of the carrier, whereas the imaginary part modulates the quadrature component of the carrier signal. Then, the spectral efficiency of GQSM is given by

$$\eta_{\mathrm{GQSM}} = 2\left\lfloor \log_2 \binom{N_T}{N_{\mathrm{a}}} \right\rfloor + \log_2(M). \tag{3.9}$$

Without loss of generality, $a_{n,m}$ and $\theta_{n,m}$ values are drawn from $M-$QAM constellation points.

AN generation

AN is intentionally generated to safeguard against information leakage across the communication channel connecting WPTx and a potential Eve and is characterized by the channel matrix $\mathbf{G}_{\mathrm{Eve}} \in \mathbb{C}^{N_{\mathrm{Eve}} \times N_T \times N}$. Provided Eve possesses knowledge of the mapping rule utilized by the IM schemes, it could intercept the information transmission between WPTx and IR, thus being capable of conducting information harvesting. The primary objective of introducing this deliberately produced interference is to enhance the robustness of the PLS within the system to combat Eve, preventing it from decoding the information intended for IR.

For the AN generation, it is assumed that the IR has N_{IR} receive antennas such that $N_{\text{IR}} < N_T$. Then, the singular value decomposition (SVD) can be implemented through each subband such that $\mathbf{H}_{\text{IR},n} = \mathbf{U}_n \mathbf{\Lambda}_n \mathbf{V}_n^H$ where $\mathbf{H}_{\text{IR},n}$ is a $N_{\text{IR}} \times N_T$ channel matrix with $r = \text{rank}\left(\mathbf{H}_{\text{IR},n}\right)$ and $\mathbf{V}_n = \left[\mathbf{v}_1^n \mathbf{v}_2^n \ldots \mathbf{v}_r^n \mathbf{v}_{r+1}^n \ldots \mathbf{v}_{N_T}^n\right]$ includes the nullspaces of $\mathbf{H}_{\text{IR},n}$, which are $\mathbf{V}_{\perp,n} = \left[\mathbf{v}_{r+1}^n \ldots \mathbf{v}_{N_T}^n\right]$. Then, the AN waveform can be expressed as

$$\boldsymbol{\varepsilon}_n = \sum_{i=r+1}^{N_t} \delta_i \mathbf{v}_i^n u_i. \tag{3.10}$$

Herein, (3.10) is the jamming signal obtained from i.i.d. Gaussian distribution, $u_i \sim \mathcal{CN}\left(0, \lambda_u^2\right)$ along with $\sum_{i=r+1}^{N_t} \delta_i^2 = 1$. Since $\mathbf{H}_{\text{IR},n} \cdot \mathbf{V}_{\perp,n} = 0$ holds, the generated AN on top of the existing WPT waveform does not affect on the received signal in IR while it leads to additional jamming power in Eve side due to $\mathbf{G}_{\text{Eve},n} \cdot \mathbf{V}_{\perp,n} \neq 0$. Given that AN is generated based on the link between WPTx and IR, it also contributes to additional jamming power on the EH side; hence, $\mathbf{G}_{\text{EH},n} \cdot \mathbf{V}_{\perp,n} \neq 0$. Later, we will provide comprehensive insights into how this interference also plays a pivotal role in boosting the system's energy harvesting capability.

As a result, the AN-added received passband waveform at the EH can be expressed as

$$\mathbf{y}_{\text{EH}} = \Re\left\{\sum_{n=1}^{N} \mathbf{G}_{\text{EH},n}\left[\mathbf{w}_n e^{j2\pi f_n t} + \boldsymbol{\varepsilon}_n e^{j2\pi f_1 t}\right]\right\}. \tag{3.11}$$

Herein, the AN waveform aligns with the frequency of the first subband, f_1, and its power defined as λ_u^2/N for nth subband (i.e., $\mathbb{E}[\boldsymbol{\varepsilon}_n^H \boldsymbol{\varepsilon}_n] = \lambda_u^2/N$). In (3.11), AWGN term is omitted, assuming that the antenna noise is negligible and not substantial enough to be harvested.

3.1.3 IR: Information harvesting

The primary objective of the IH mechanism is to extract information from the received WPT-IM waveform. To conduct this, the IR leverages both the mapping rule employed by the IM scheme and the CSI of the WPT-IR link. While energy can be directly harvested from the received RF signal, the IR must acquire the baseband version of the received signal for a specific subband n. Following downconversion and filtering processes, the resulting baseband signal at the IR is mathematically expressed as described in [Clerckx et al., 2019]

$$\mathbf{y}_{\mathrm{IR},n} = \mathbf{H}_{\mathrm{IR},n}\mathbf{x}_n + \mathbf{z}_{\mathrm{IR},n}. \tag{3.12}$$

Here, $\mathbf{x}_n$ includes the WPT-IM waveform $\mathbf{w}_n$ along with the AN waveform $\boldsymbol{\varepsilon}_n$ such that $\mathbf{x}_n = \mathbf{w}_n + \boldsymbol{\varepsilon}_n$. In (3.12) $\mathbf{z}_{\mathrm{IR},n} \in \mathbb{C}^{N_{\mathrm{IR}} \times 1}$ denotes the noise vector, where its each element $z_{\mathrm{IR},n} \sim \mathcal{CN}(0, \sigma_n^2)$ has a zero mean and a variance σ_n^2 for the nth subband. Consequently, the total received baseband signal at the IR can be represented as:

$$\mathbf{y}_{\mathrm{IR}} = \sum_{n=1}^{N} \left[\mathbf{H}_{\mathrm{IR},n}\mathbf{x}_n + \mathbf{z}_{\mathrm{IR},n}\right]. \tag{3.13}$$

The IR employs an ML detector to estimate transmitted bits from the WPT-IM waveform. Since various IM techniques can be employed for conveying information, the resulting ML representations vary based on the utilized IM scheme. Consequently, the optimum ML decoder representations are provided separately below.

GSSK/SSK-based IH

The GSSK technique involves selecting specific columns from each subband component of the channel matrix, $\mathbf{H}_{\mathrm{IR},n}$ to transmit information bits. Accordingly, the product $\mathbf{H}_{\mathrm{IR},n}\mathbf{x}_n$ yields the term $\mathbf{h}_{\mathrm{IR},n}^{l}$, which corresponds to the channel coefficient set of the lth GSSK codebook out of L possible combinations in total. It is worth noting that in the case of SSK, only a single column of $\mathbf{H}_{\mathrm{IR},n}$ is chosen. Therefore, for mechanisms based on GSSK/SSK, the ML detector is designed to estimate the transmit antenna indices when given the value of N_{a}. The ML procedure can be implemented as follows:

$$\hat{l}_{\mathrm{IR}} = \underset{l\in\{1,\ldots,L\}}{\arg\min} \sum_{n=1}^{N} \left\| \mathbf{y}_{\mathrm{IR},n} - \mathbf{h}^{l}_{\mathrm{IR},n} \right\|^2 . \tag{3.14}$$

Here, $\hat{l}_{\mathrm{IR}}$ represents the estimated antenna index.

GSM/SM-based IH

GSM/SM schemes differ from GSSK/SSK ones through the use of signal modulation, specifically M-QAM, to enhance spectral efficiency. In cases where the WPT waveform includes a modulated symbol, (3.14) can be rewritten as follows:

$$(\hat{l}_{\mathrm{IR}}, \hat{\omega}) = \underset{l\in\{1,\ldots,L\},\omega\in\psi}{\arg\min} \sum_{n=1}^{N} \left\| \mathbf{y}_{\mathrm{IR},n} - \mathbf{h}^{l}_{\mathrm{IR},n}\omega \right\|^2 . \tag{3.15}$$

Here, $\omega_{n,m}$ representation in (3.4) simplifies to a ω as IM schemes transmit identical symbols from N_{a} active antennas across all subbands. Thus, $\omega = ae^{j\theta}$ represents a symbol selected from an M-QAM constellation, ψ, and $\hat{\omega}$ is decoded transmitted symbol.

GQSSK/QSSK-based IH

Similar to the GSSK/SSK-based mechanism, the ML detector only needs to estimate the active antenna indices without performing symbol decoding. The distinction is that QSSK scheme activates two antennas at a time to convey quadrature components, whereas GQSSK might activate more than two antennas. Hence, the ML detector should jointly estimate in-phase and quadrature components, and it is given by

$$\left(\hat{l}^{\Re}_{\mathrm{IR}}, \hat{l}^{\Im}_{\mathrm{IR}}\right) = \underset{\substack{\mathbf{h}^{\Re,l}_{\mathrm{IR}},\mathbf{h}^{\Im,l}_{\mathrm{IR}}\\ l\in\{1,\ldots,L\}}}{\arg\min} \sum_{n=1}^{N} \left\| \mathbf{y}_{\mathrm{IR},n} - \left[\mathbf{h}^{\Re,l}_{\mathrm{IR},n} + j\mathbf{h}^{\Im,l}_{\mathrm{IR},n}\right] \right\|^2 . \tag{3.16}$$

Herein, $\mathbf{h}^{\Re,l}_{\mathrm{IR}}$ and $\mathbf{h}^{\Im,l}_{\mathrm{IR}}$ correspond to the lth potential codebook channel coefficient set of the WPTx-IR link out of L candidates for real part and imaginary part transmission, respectively. $\left(\hat{l}^{\Re}_{\mathrm{IR}}, \hat{l}^{\Im}_{\mathrm{IR}}\right)$ refers the estimated indices of active transmit antennas at the IR. For a toy example, $\left(\hat{l}^{\Re}_{\mathrm{IR}}, \hat{l}^{\Im}_{\mathrm{IR}}\right) = ([110], [011])$ implies the 1st and

2nd transmit antennas are active for the real part and 2nd and 3rd for the imaginary part, respectively.

GQSM/QSM-based IH

GQSM/QSM augments QSSK/GQSSK techniques by incorporating M-QAM constellation symbols to transmit quadrature components, separately containing the in-phase and quadrature part of the M-QAM symbol. If the WPT-IM waveform contains a modulated symbol, (3.16) can be rewritten as follows:

$$\left(\hat{l}_{\mathrm{IR}}^{\Re}, \hat{l}_{\mathrm{IR}}^{\Im}, \hat{\omega}\right) = \underset{\substack{\mathbf{h}_{\mathrm{IR}}^{\Re,l}, \mathbf{h}_{\mathrm{IR},n}^{\Im,l} \\ l\in\{1,\ldots,L\}, \omega\in\psi}}{\arg\min} \sum_{n=1}^{N} \left\| \mathbf{y}_{\mathrm{IR},n} - \left[\mathbf{h}_{\mathrm{IR},n}^{\Re,l} \Re\{\omega\} + j\mathbf{h}_{\mathrm{IR},n}^{\Im,l} \Im\{\omega\}\right] \right\|^2, \quad (3.17)$$

where $\hat{\omega}$ is a decoded transmitted symbol whose real and imaginary parts are carried by different active transmit antennas.

3.2 Error Performance Analysis

In this section, average bit error rates (ABER) at the IR and the Eve are calculated, respectively.

3.2.1 ABER of Information receiver

The conditional pairwise error probability (CPEP) of deciding on a baseband IM codebook $\boldsymbol{x}_k$ in the case of that $\boldsymbol{x}_j$ transmitted under ML detection can be calculated by [Mesleh et al., 2015]

$$\begin{aligned} &P(\boldsymbol{x}_j \rightarrow \boldsymbol{x}_k \mid \mathbf{H}_{\mathrm{IR}}) = \\ &P\left(\left\|\sum_{n=1}^{N} \mathbf{z}_{\mathrm{IR},n}\right\|^2 > \left\|\sum_{n=1}^{N} \mathbf{H}_{\mathrm{IR},n}\left(\mathbf{w}_n^j - \mathbf{w}_n^k\right) + \mathbf{z}_{\mathrm{IR},n}\right\|^2 \middle| \mathbf{H}_{\mathrm{IR}}\right) = \\ &P\left(2\Re\left\{\sum_{n=1}^{N} \mathbf{z}_{\mathrm{IR},n}^H \left(\mathbf{h}_{\mathrm{IR},n}^j \omega_j - \mathbf{h}_{\mathrm{IR},n}^k \omega_k\right)\right\} > \left\|\sum_{n=1}^{N} \left(\mathbf{h}_{\mathrm{IR},n}^j \omega_j - \mathbf{h}_{\mathrm{IR},n}^k \omega_k\right)\right\|^2 \middle| \mathbf{H}_{\mathrm{IR}}\right) \\ &= \mathcal{Q}\left(\sqrt{\sum_{i=1}^{N_{\mathrm{IR}}} \frac{\sum_{n=1}^{N} |\Phi_{\mathrm{IR},i}^{(n)}|^2}{2N\sigma^2}}\right) = \mathcal{Q}\left(\sqrt{\gamma_{\mathrm{IR}}}\right). \end{aligned} \quad (3.18)$$

Herein, $\Phi_{\mathrm{IR},i}^{(n)}$ is defined as $\Phi_{\mathrm{IR},i}^{(n)} = (h_{\mathrm{IR},n,i}^{\Re,j}\omega_j^{\Re} - h_{\mathrm{IR},n,i}^{\Re,k}\omega_k^{\Re}) + (h_{\mathrm{IR},n,i}^{\Im,j}\omega_j^{\Im} - h_{\mathrm{IR},n,i}^{\Im,k}\omega_k^{\Im})$. Note that (3.18) introduces a generalized CPEP expression, and it can be utilized for calculating the different types of the IM schemes, ranging from the ones that do not employ modulated symbols to the ones that also carry a set of modulated symbols. The corresponding expressions for $\mathbf{\Phi}_{\mathrm{IR}}^{(n)}$ are presented in Table 3.1.

IM schemes with one active Tx per index

To begin with, $\Phi_{\mathbf{IR}}^{(n)}$ can be simplified for the SSK and GSSK schemes by considering $\omega_j^{\Re} = \omega_k^{\Re} = \omega_j^{\Im} = \omega_k^{\Im} = 1$, and for the QSSK and GQSSK schemes by considering $\omega_j^{\Re} = \omega_k^{\Re} = 1$ and $\omega_j^{\Im} = \omega_k^{\Im} = j$. This simplification is applicable to the IM schemes that do not employ signal modulation, namely SSK, GSSK, QSSK, and GQSSK.

IM schemes with one multiple Tx per index

In the case of generalized IM schemes, that are GSSK, GSM, GQSSK, and GQSM, that simultaneously activate multiple antennas instead of single one, the corresponding effective channel columns $\mathbf{h}_{\mathrm{IR},n,i}^{j_{\mathrm{eff}}}$ and $\mathbf{h}_{\mathrm{IR},n,i}^{k_{\mathrm{eff}}}$ are considered in the ABER calculation since it represents the summation of the columns corresponding to active transmit antennas in the channel matrix of $\mathbf{H}_{\mathrm{IR}}$.

Table 3.1: CORRESPONDING $\mathbf{\Phi}_{\mathrm{IR}}^{(n)}$ EXPRESSIONS FOR THE USED IM SCHEMES.

IM Scheme	$\mathbf{\Phi}_{\mathrm{IR}}^{(n)}$
SSK	$(\mathbf{h}_{\mathrm{IR},n,i}^{j} - \mathbf{h}_{\mathrm{IR},n,i}^{k})$
QSSK	$(\mathbf{h}_{\mathrm{IR},n,i}^{\Re,j} - \mathbf{h}_{\mathrm{IR},n,i}^{\Re,k}) + j(\mathbf{h}_{\mathrm{IR},n,i}^{\Im,j} - \mathbf{h}_{\mathrm{IR},n,i}^{\Im,k})$
SM	$(\mathbf{h}_{\mathrm{IR},n,i}^{j}\omega_j - \mathbf{h}_{\mathrm{IR},n,i}^{k}\omega_k)$
QSM	$(\mathbf{h}_{\mathrm{IR},n,i}^{\Re,j}\omega_j^{\Re} - \mathbf{h}_{\mathrm{IR},n,i}^{\Re,k}\omega_k^{\Re}) + (\mathbf{h}_{\mathrm{IR},n,i}^{\Im,j}\omega_j^{\Im} - \mathbf{h}_{\mathrm{IR},n,i}^{\Im,k}\omega_k^{\Im})$
GSSK	$(\mathbf{h}_{\mathrm{IR},n,i}^{j_{\mathrm{eff}}} - \mathbf{h}_{\mathrm{IR},n,i}^{k_{\mathrm{eff}}})$
GQSSK	$(\mathbf{h}_{\mathrm{IR},n,i}^{\Re,j_{\mathrm{eff}}} - \mathbf{h}_{\mathrm{IR},n,i}^{\Re,k_{\mathrm{eff}}}) + j(\mathbf{h}_{\mathrm{IR},n,i}^{\Im,j_{\mathrm{eff}}} - \mathbf{h}_{\mathrm{IR},n,i}^{\Im,k_{\mathrm{eff}}})$
GSM	$(\mathbf{h}_{\mathrm{IR},n,i}^{j_{\mathrm{eff}}}\omega_j - \mathbf{h}_{\mathrm{IR},n,i}^{k_{\mathrm{eff}}}\omega_k)$
GQSM	$(\mathbf{h}_{\mathrm{IR},n,i}^{\Re,j_{\mathrm{eff}}}\omega_j^{\Re} - \mathbf{h}_{\mathrm{IR},n,i}^{\Re,k_{\mathrm{eff}}}\omega_k^{\Re}) + (\mathbf{h}_{\mathrm{IR},n,i}^{\Im,j_{\mathrm{eff}}}\omega_j^{\Im} - \mathbf{h}_{\mathrm{IR},n,i}^{\Im,k_{\mathrm{eff}}}\omega_k^{\Im})$

IM schemes with modulated symbol

If there is signal modulation involved, ω is drawn from M-QAM contellation points on top of antenna indices for SM, GSM, QSM, and GQSM schemes.

Then, (3.18) implies that γ_{IR} follows a central chi-square distribution with $2N_{\text{IR}}$ degrees of freedom and it can be written as $\gamma_{\text{IR}} = \Sigma_{r=1}^{N_{\text{IR}}} |\nu_r^{\text{IR}}|^2$. Herein, $\nu_r^{\text{IR}} = \Sigma_{n=1}^{N} (h_{\text{IR},n,r}^{j} \omega_j - h_{\text{IR},n,r}^{k} \omega_k)/\sqrt{2\sigma_n^2}$ represents the rth element of $\mathbf{\Phi}_{\mathbf{IR}}^{(n)}$, which has a row length of N_{IR}.

Remark 1: Assuming that ω_j and ω_k are drawn from real constellation points and equal to 1, such that γ_{IR} reduces to $\gamma_{\text{IR}} = \Sigma_{r=1}^{N_{\text{IR}}} \left(\Sigma_{n=1}^{N} |h_{\text{IR},n,r}^{j} - h_{\text{IR},n,r}^{k}|^2 / 2\sigma_n^2 \right)$. Since there is a constraint on transmit power $\Sigma_{n=1}^{N} \|\mathbf{w}_n\|^2 \leq P_T$, and λ_s^2 is distributed equally among the elements of $\mathbf{w}_n$, introducing more subbands has no effect on $|h_{\text{IR},n,r}^{j} - h_{\text{IR},n,r}^{k}|$. Nonetheless, increasing the number of subbands, N, scales the numerator term of γ_{IR} by $1/(2\Sigma_{n=1}^{N} \sigma_n^2)$. Hence, an increase in N negatively affects the performance of the IH mechanism.

The average PEP, $P(\boldsymbol{x}_j \to \boldsymbol{x}_k)$, is written as follows[Di Renzo and Haas, 2010]:

$$P(\boldsymbol{x}_j \to \boldsymbol{x}_k) = \xi^{N_{\text{IR}}} \sum_{i=0}^{N_{\text{IR}}-1} \begin{pmatrix} N_{\text{IR}} - 1 + i \\ i \end{pmatrix} [1 - \xi]^i , \tag{3.19}$$

where $\xi = (1 - \sqrt{(\bar{\nu}/2)/(1 + \bar{\nu}/2)})/2$ and $\bar{\nu}$ represents the mean value of ν_r^{IR} as detailed in [Mesleh et al., 2015]. After applying (3.19) and utilizing the well-known union bound expression, the generalized ABER expression for the IM-based IH mechanism can be calculated as follows:

$$\text{ABER} = \frac{1}{\eta} \frac{1}{L} \sum_{j=1}^{L} \sum_{k \neq j=1}^{L} \epsilon\,(j,k)\, P(\boldsymbol{x}_j \to \boldsymbol{x}_k), \tag{3.20}$$

where $\epsilon(j,k)$ is the number of erroneous bits when a codeword $\boldsymbol{x}_k$ is decoded at the IR when $\boldsymbol{x}_j$ is transmitted at the WPTx.

3.2.2 ABER of Eavesdropper

In this subsection, the ABER expression at the Eve is investigated, and the results herein can be utilized for evaluating a potential case where the EH acts in a malicious role such that EH tries to intercept information transmission intended for an information receiver for a given service area. To begin with, similar to (3.18), the conditional PEP expression for Eve can be expressed as follows:

$$\begin{aligned} &P(\boldsymbol{x}_j \to \boldsymbol{x}_k \mid \mathbf{G}_{\text{Eve}}) = \\ &P\left(\left\|\sum_{n=1}^{N} \Psi_n \left(\mathbf{G}_{\text{Eve},n}\boldsymbol{\varepsilon}_n + \mathbf{z}_{\text{Eve},n}\right)\right\|^2 \right. \\ &\left. > \left\|\sum_{n=1}^{N} \Psi_n \left[\mathbf{G}_{\text{Eve},n}\left(\mathbf{w}_n^j - \mathbf{w}_n^k\right) + \mathbf{G}_{\text{Eve},n}\boldsymbol{\varepsilon}_n + \mathbf{z}_{\text{Eve},n}\right]\right\|^2 \middle| \mathbf{G}_{\text{Eve}}\right). \end{aligned} \tag{3.21}$$

The expression $\hat{\Phi}_{\text{Eve},i}^{(n)}$ is defined as $\hat{\Phi}_{\text{Eve},i}^{(n)} = (g_{\text{Eve},n,i}^{\Re,j}\omega_j^{\Re} - g_{\text{Eve},n,i}^{\Re,k}\omega_k^{\Re}) + (g_{\text{Eve},n,i}^{\Im,j}\omega_j^{\Im} - g_{\text{Eve},n,i}^{\Im,k}\omega_k^{\Im})$, and it is obtained after applying the whitening transformation. The term $\Psi_n = \sigma_n \mathbf{C}_\epsilon^{-1/2}$ represents the whitening transformation matrix, where $\mathbf{C}_\epsilon$ is the covariance matrix of the interference plus noise term at Eve, given by:

$$\mathbf{C}_\epsilon = \frac{\lambda_u^2}{N(N_T - r)}\mathbf{G}_{\text{Eve},n}\left(\sum_{i=r+1}^{N_T} \mathbf{v}_i^n \mathbf{v} i^{n^H}\right)\mathbf{G}_{\text{Eve},n}^H + \sigma_n^2\mathbf{I}. \tag{3.22}$$

Note that the power of Ψ_n needs to be arranged based on the total number of available subbands and after multiplying Ψ_n with given WPT-IM waveforms, (3.21) reduces to

$$P(\boldsymbol{x}_j \to \boldsymbol{x}_k \mid \mathbf{G}_{\text{Eve}}) = \mathcal{Q}\left(\sqrt{\sum_{i=1}^{N_{\text{Eve}}} \frac{\sum_{n=1}^{N} |\hat{\Phi}_{\text{Eve},i}^{(n)}|^2}{2(N\sigma^2 + \lambda_u^2)}}\right) = \mathcal{Q}\left(\sqrt{\gamma_{\text{Eve}}}\right). \tag{3.23}$$

Herein, $\gamma_{\text{Eve}} = \Sigma_{r=1}^{N_{\text{Eve}}} |\nu_r^{\text{Eve}}|^2$ shows the similar characteristics with γ_{IR} given in (3.18) and the parameter $\nu_r^{\text{Eve}} = \Sigma_{n=1}^{N}(g_{\text{Eve},n,r}^{j}\omega_j - g_{\text{Eve},n,r}^{k}\omega_k) \big/ \sqrt{2\sigma_n^2 + 2\lambda_u^2}$ signifies the r-th element of the vector $\hat{\boldsymbol{\Phi}}_{\text{Eve}}^{(n)}$, which has a row length of N_{Eve}. In this regard, the selection of $\hat{\boldsymbol{\Phi}}_{\text{Eve}}^{(n)}$ should be aligned with the selected IM schemes for information harvesting, as in the selection of $\boldsymbol{\Phi}_{\text{IR}}^{(n)}$. Then, the calculation of the ABER at the Eve can be obtained after substituting (3.23) into (3.20).

Remark 2: Obeying the same constraint on P_T and following the assumption that ω_j and ω_k are drawn from real constellation points and equal to 1, γ_{Eve} reduces to $\gamma_{\text{Eve}} = \Sigma_{r=1}^{N_{\text{Eve}}}\left(\Sigma_{n=1}^{N}|g_{\text{Eve},n,r}^{j} - g_{\text{Eve},n,r}^{k}|^2 \big/ (2\sigma_n^2 + 2\lambda_u^2)\right)$. Therefore, the numerator term of γ_{Eve} is scaled by a factor of $1/\left(2\Sigma_{n=1}^{N}\sigma_n^2 + 2\lambda_u^2\right)$, which means that increasing N will lower the performance of Eve. As the SNR increases, and given that P_T is constant, λ_u^2 will progressively dominate over σ_n^2, especially when $\lambda_u^2 \gg \Sigma_{n=1}^{N}\sigma_n^2$, resulting in performance saturation, leading to identical performance across all values of N.

3.3 Ergodic Secrecy Rate Analysis

In this section, we provide a generalized analytical framework of the ergodic secrecy rate for the proposed IM-based information harvesting schemes.

To do so, the GQSSK-based IH mechanism was considered. In this respect, each transmit antenna set for the real and the imaginary parts is selected with the same probability, $1/L$. Then, the received signal at the IR through N band, $\mathbf{y}_{\mathrm{IR}}$, obeys the following distribution [Huang et al., 2017]

$$p\left(\mathbf{y}_{\mathrm{IR}}\right) = \frac{1}{L^2}\sum_{j=1}^{L}\sum_{k=1}^{L}\frac{1}{\pi\sigma_n^2}e^{-\frac{\|\mathbf{r}_{\mathrm{IR}}\|^2}{\sigma_n^2}}. \tag{3.24}$$

Here, $\mathbf{r}_{\mathrm{IR}} = \mathbf{y}_{\mathrm{IR}} - \mathbf{h}_{\mathrm{IR}}^{\Re,j}\Re\{\omega\} - j\mathbf{h}_{\mathrm{IR}}^{\Im,k}\Im\{\omega\}$ for a transmitted WPT signal, ω. Then, the mutual information, $\mathcal{I}_{\mathrm{IR}}\left(\mathbf{r}_{\mathrm{IR}}\right)$, can be expressed in (3.26), which is a special case of [Eq. (14), [Huang et al., 2017]]. Therein, $\mathbf{d}_{l_1,l_2}^{r_1,r_2}$ is defined as:

$$\mathbf{d}_{l_1,l_2}^{r_1,r_2} = \mathbf{h}_{\mathrm{IR}}^{\Re,l_{2\mathrm{eff}}}\Re\{\omega\} + j\mathbf{h}_{\mathrm{IR}}^{\Im,l_{1\mathrm{eff}}}\Im\{\omega\} - \mathbf{h}_{\mathrm{IR}}^{\Re,r_{1\mathrm{eff}}}\Re\{\omega\} - j\mathbf{h}_{\mathrm{IR}}^{\Im,r_{2\mathrm{eff}}}\Im\{\omega\} \tag{3.25}$$

where $\mathbf{h}_{\mathrm{IR}}^{\mathrm{eff}}$ is the effective channel after incorporating only active transmit antenna set at the IR such that $\mathbf{h}_{\mathrm{Eve}}^{i_{\mathrm{eff}}} = \mathbf{h}_{\mathrm{Eve}}^{i,1} + \cdots + \mathbf{h}_{\mathrm{Eve}}^{i,N_a}$ [Wei et al., 2015].

$$\begin{aligned}\mathcal{I}_{\mathrm{IR}}\left(\mathbf{y}_{\mathrm{IR}}\right) &= \log_2\left(L^2\right)\\ &- \frac{1}{L^2}\sum_{l_1=1}^{L}\sum_{l_2=1}^{L}\mathbb{E}_{\mathbf{z}_{\mathrm{IR}}}\left[\log_2\left(\sum_{r_1=1}^{L}\sum_{r_2=1}^{L}e^{-\frac{\left\|\mathbf{d}_{l_1,l_2}^{r_1,r_2}+\mathbf{z}_{\mathrm{IR}}\right\|^2-\left\|\mathbf{z}_{\mathrm{IR}}\right\|^2}{\sigma^2}}\right)\right].\end{aligned} \tag{3.26}$$

$$\begin{aligned}\mathcal{I}_{\mathrm{Eve}}\left(\mathbf{y}_{\mathrm{Eve}}\right) &= \log_2\left(L^2\right)\\ &- \frac{1}{L^2}\sum_{l_1=1}^{L}\sum_{l_2=1}^{L}\mathbb{E}_{\mathbf{z}_{\mathrm{Eve}}}\left[\log_2\left(\sum_{r_1=1}^{L}\sum_{r_2=1}^{L}e^{-\frac{\left\|\boldsymbol{\delta}_{l_1,l_2}^{r_1,r_2}+\mathbf{z}_{\mathrm{Eve}}\right\|^2-\left\|\mathbf{z}_{\mathrm{Eve}}\right\|^2}{\sigma^2}}\right)\right].\end{aligned} \tag{3.27}$$

Similar to (3.24), the received signal at the Eve obeys the following distribution [Huang et al., 2017]

$$p\left(\mathbf{y}_{\mathrm{Eve}}\right)=\frac{1}{L^2}\sum_{j=1}^{L}\sum_{k=1}^{L}\frac{1}{\pi\sigma_n^2}e^{-\frac{\|\mathbf{r}_{\mathrm{Eve}}\|^2}{\sigma_n^2}}. \tag{3.28}$$

Therein, $\mathbf{r}_{\mathrm{Eve}}=\mathbf{y}_{\mathrm{IR}}-\mathbf{g}_{\mathrm{Eve}}^{\Re,j}\Re\{\omega\}-j\mathbf{g}_{\mathrm{Eve}}^{\Im,k}\Im\{\omega\}$. After accounting for the existence of the AN at the Eve side, the mutual information at Eve, $\mathcal{I}_{\mathrm{Eve}}\left(\mathbf{r}_{\mathrm{Eve}}\right)$, is given in (3.27), which is a special case of [Eq. (15), [Huang et al., 2017]]. Here, $\mathbf{z}_{\mathrm{Eve}}$ is the Gaussian noise at the Eve and $\boldsymbol{\delta}_{l_1,l_2}^{r_1,r_2}$ can be expressed as:

$$\boldsymbol{\delta}_{l_1,l_2}^{r_1,r_2}=\mathbf{C}_{\epsilon}^{-\frac{1}{2}}\left(\mathbf{g}_{\mathrm{Eve}}^{\Re,l_{2\mathrm{eff}}}\Re\{\omega\}+j\mathbf{g}_{\mathrm{Eve}}^{\Im,l_{1\mathrm{eff}}}\Im\{\omega\}\right)-\mathbf{C}_{\epsilon}^{-\frac{1}{2}}\left(\mathbf{g}_{\mathrm{Eve}}^{\Re,r_{1\mathrm{eff}}}\Re\{\omega\}-j\mathbf{g}_{\mathrm{Eve}}^{\Im,r_{2\mathrm{eff}}}\Im\{\omega\}\right), \tag{3.29}$$

where $\mathbf{g}_{\mathrm{Eve}}^{i_{\mathrm{eff}}}$ is the effective channel.

Note that the channel between the WPTx and the IR relies on GQSSK-based modulated antenna indices, so the capacity analysis deducts into a capacity analysis for the discrete-input continuous-output memoryless channel (DCMC) [Singh et al., 2021], and it might be not straightforward to obtain the closed-form analysis in most cases. In this respect, the secrecy rate of IR can be expressed as [Wei et al., 2015]

$$\mathcal{R}_{\mathrm{IR}}=\max\{0,\ \mathcal{I}_{\mathrm{IR}}\left(\mathbf{y}_{\mathrm{IR}}\right)-\mathcal{I}_{\mathrm{Eve}}\left(\mathbf{y}_{\mathrm{Eve}}\right)\}, \tag{3.30}$$

Note that positive secrecy from (3.30) implies communication opportunity on top of the existing WPT mechanism, even if some information can be leaked to Eve in the service area.

For the other IM schemes given in Section II.B, the ergodic secrecy rates can be obtained from (3.30) after modifying (3.26) and (3.27) where L^2 results in exploiting two different active antenna sets for real and imaginary parts of the emitted waveforms where L is the number of available antenna combinations for each part. For instance, in the case of GQSM/QSM-based IH, the summation limits should be replaced with $L\rightarrow LM$ where M is the modulation order and ω seen in (3.25) becomes a variable of the summation indices rather than constant waveform such that ω_{l_1}.

For GQSSK/SSK schemes, the secrecy calculation requires one effective channel definition without dividing real and imaginary parts so the definition of $\mathbf{r}_{\mathrm{IR}}$ in (3.24) is reformulated as $\mathbf{r}_{\mathrm{IR,n}} = \mathbf{y}_{\mathrm{IR,n}} - \mathbf{h}_j^n \omega$ [Wei et al., 2015] which results in

$$\begin{aligned}\mathcal{I}_{\mathrm{IR}}\left(\mathbf{y}_{\mathrm{IR}}\right) &= \log_2\left(L\right) \\ &- \frac{1}{L}\sum_{l_1=1}^{L}\mathbb{E}_{\mathbf{z}_{\mathrm{IR}}}\left[\log_2\left(\sum_{l_2=1}^{L} e^{-\frac{\left\|\mathbf{d}_{l_1}^{l_2}+\mathbf{z}_{\mathrm{IR}}\right\|^2 - \left\|\mathbf{z}_{\mathrm{IR,n}}\right\|^2}{\sigma_n^2}}\right)\right].\end{aligned} \tag{3.31}$$

A similar approach is functional when considering the scenario involving Eve, where its mutual information can be expressed as follows:

$$\begin{aligned}\mathcal{I}_{\mathrm{Eve}}\left(\mathbf{y}_{\mathrm{Eve}}\right) &= \log_2\left(L\right) \\ &- \frac{1}{L}\sum_{l_1=1}^{L}\mathbb{E}_{\mathbf{z}_{\mathrm{Eve}}}\left[\log_2\left(\sum_{l_2=1}^{L} e^{-\frac{\left\|\boldsymbol{\varrho}_{l_1}^{l_2}+\mathbf{z}_{\mathrm{Eve}}\right\|^2 - \left\|\mathbf{z}_{\mathrm{Eve}}\right\|^2}{\sigma_n^2}}\right)\right].\end{aligned} \tag{3.32}$$

Herein, $\mathbf{d}_{l_1}^{l_2}$ and $\boldsymbol{\varrho}_{l_1}^{l_2}$ correspond to the channel distances between m_1th and m_2th antenna index combinations at the IR and the Eve for the nth subband, where N_{a} antennas out of N_T are active such that $\mathbf{d}_{l_1}^{l_2} = \mathbf{h}_{\mathrm{l_1,eff}} - \mathbf{h}_{\mathrm{l_2,eff}}$ and $\boldsymbol{\varrho}_{l_1}^{l_2} = \mathbf{g}_{\mathrm{l_1,eff}} - \mathbf{g}_{\mathrm{l_2,eff}}$, respectively. For GSM/SM-based IH, the summation limits should be replaced with $L \to LM$ where M is the modulation order, the calculation of $\mathbf{d}_{l_1}^{l_2}$ takes into account ω as in [Wei et al., 2015].

3.4 Numerical Results

In this section, we explore the feasibility of IM-based IH schemes in terms of their energy harvesting capability, bit error rate (BER), and ergodic secrecy rate (ESR) performances under various system setups where multitone signals are utilized for far-field WPT transmissions. The comparison involves diverse IM schemes, including GSSK with $N_T = 24$, GSM with $N_T = 8$, and 16-QAM, SM with $N_T = 16$, and 16-QAM, as well as SM with $N_T = 64$ and 4-QAM. Also, QSM with $N_T = 8$ and 4-QAM, QSSK with $N_T = 16$, GQSM with $N_T = 5$ and 4-QAM, and GQSSK with $N_T = 7$ and 4-QAM. Note that all IM schemes share a common spectral efficiency of $\eta = 8$, and in all scenarios, N_{a} and N_{EH} are set to 2 and 4, respectively. The channels between WPTx and EH, as well as between WPTx and IR, are assumed to be Rayleigh fading channels. Considering that the EH's energy scavenging ability is directly impacted by the distance between the transmitter and receiver [Zhou et al., 2013], we utilize the following path loss model: $35.3 + 37.6 \log_{10}(d)$, where d represents the distance between WPTx and EH. The EH is assumed to consist of N_{EH} pairs of receive antennas and rectennas, with perfect matching and an ideal low-pass filter assumed in rectennas.

In order to limit the maximum effective isotropic radiated power (EIRP) as specified in FCC Title 47, Part 15 regulations [Federal Commun. Comm., 2016], the total transmit power is considered as $P_T = 36$ dBm at the WPTx. The total transmit power, P_T, is divided into AN and IM parts based on the power allocation factor ρ $(0 \leq \rho \leq 1)$. Mainly, $\lambda_u^2 = \rho P_T$ represents the transmit power of the AN waveform, and $\lambda_s^2 = (1-\rho)P_T$ represents the transmit power of the IM waveform. Consequently, as ρ increases, the transmit power allocated for the IM waveform decreases, and that of the AN waveform increases.

The WPTx emits multitone IM waveforms where the available power is equally distributed among N_{a} active transmit antennas, whereas the generated AN is emitted from all antennas. Multitone signals with a bandwidth B are defined by the expression $(n-1)\Delta f_N$, where Δf_N represents the inter-carrier frequency spacing, set at 1 kHz and is employed in simulations The frequency of the first subband, f_1, is

Table 3.2: SIMULATION PARAMETERS USED IN IM-based IH.

Parameter	**Value**	**Reference**
k_2, k_4	$0.0034, 0.3829$	[Kim et al., 2020]
d	$[1, 6]$	-
Path-loss model	$35.3 + 37.6 \log_{10}(d)$	[Ilter et al., 2022a]
R_{ant}	50 Ω	[Kim et al., 2020]
P_T	36 dBm	-
N	$\{1, 3, 5\}$	-

set at 100 kHz, while the subsequent subbands adhere to the frequency relationship $f_n = f_1 + \Delta f_N$. Note that WPT waveforms do not rely on CSI, although the CSI of the WPTx-IR link is available at the transmitter and is utilized in generating the AN. The simulation parameters regarding WPTx are provided in Table 3.2.

We compare our simulation results with two benchmark schemes: MU-SWIPT [Xu et al., 2014] and Time Switching (TS)-SWIPT [Kang et al., 2020]. In both settings, $N_T = 6$ transmit antennas are assumed for TS-SWIPT and MU-SWIPT. In MU-SWIPT, matched filtering (MF) [Kim et al., 2020] is employed for the AP-IR and AP-ER links, each with a single receive antenna ($N_{\mathrm{IR}} = 1$) at both the IR and EH. On the other hand, TS-SWIPT has $N_{\mathrm{IR}} = 4$ for both the IR and EH, utilizing DC combining at the EH. In both settings, M-QAM is used for information signals, and RG signals are employed for energy signals. For the MU-SWIPT case, a% of the power is allocated to information transfer, while for the TS-SWIPT case, b% of the transmitted symbol frame is allocated to information transfer.

3.4.1 Energy harvesting capability

In this subsection, we investigated the benefits of the IM-based IH mechanism at the EH and present a comparative analysis that exhaustively evaluates energy harvesting capabilities for different N values and varying ρ parameters. Figs. 3.2 and 3.3 illustrate that AN significantly affects the energy harvesting capability of the IH system since AN introduces interference on the EH end while facilitating secure WIT by disrupting Eve's signal. As the power allocation factor, ρ, increases, EH experiences more interference, which is advantageous for RF energy harvesting. Thus, higher ρ values contribute to improved energy harvesting capability across all IM schemes. As a result, the IH mechanism strategically enhances the system's energy harvesting capability while providing secure WIPT through the incorporation of AN. It is noteworthy that all IM schemes exhibit nearly identical results in the case of CW signals ($N = 1$) for RF energy harvesting since the constant envelope characteristics of CW signals and also modulation schemes such as 4-QAM/PSK are not beneficial for energy harvesting with the utilized nonlinear rectifier model [Clerckx et al.,

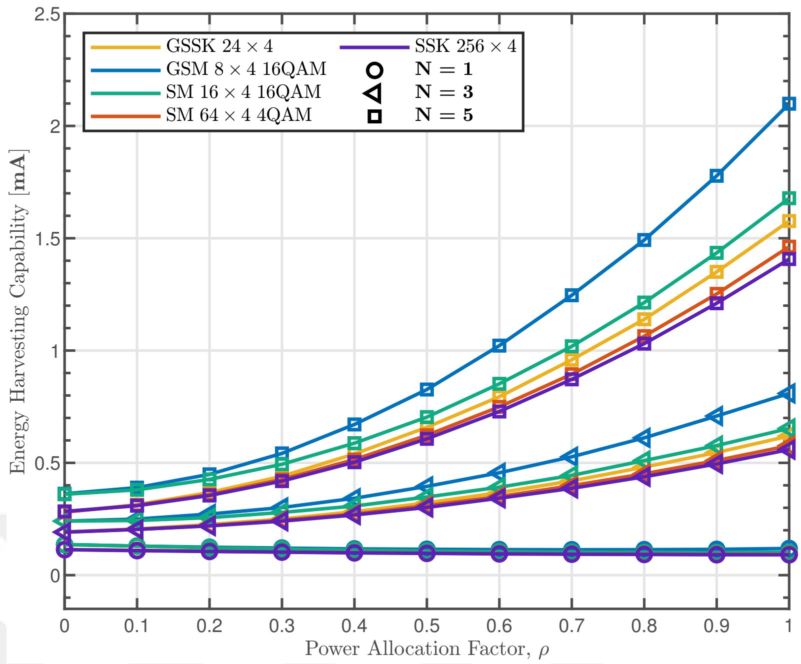

Figure 3.2: The energy harvesting capability (z_{DC}) comparison of SM schemes with $\eta = 8$ for different N values with respect to varying power allocation factors, the EH is located at $d = 1.5$m from the WPTx.

2022]. To illustrate the impact of higher-order modulation schemes on the rectifier's nonlinearity, Fig. 3.2 compares SM schemes utilizing 4-QAM and 16-QAM. It is observed that 16-QAM outperforms 4-QAM in terms of energy harvesting capability due to higher M values inducing amplitude fluctuations, thereby improving the efficiency of RF-to-DC conversion within the rectifier [Clerckx and Bayguzina, 2016]. Therefore, the modulation type impacts the system's energy harvesting capability [Cansiz et al., 2020].

Moreover, the comparison between Figs. 3.2 and 3.3 demonstrate that introducing multitone signals, coupled with IM schemes, enhances the energy harvesting capability across all IM schemes. As N increases, IM schemes exhibit distinct characteristics. The best performance results are acquired by IM schemes that activate more than one antenna at a time and also select $\mathbf{w}_n$ values from the M-QAM constellations. Since IM schemes activate more antennas than those activating one antenna at a time to convey information, they achieve the same spectral efficiency

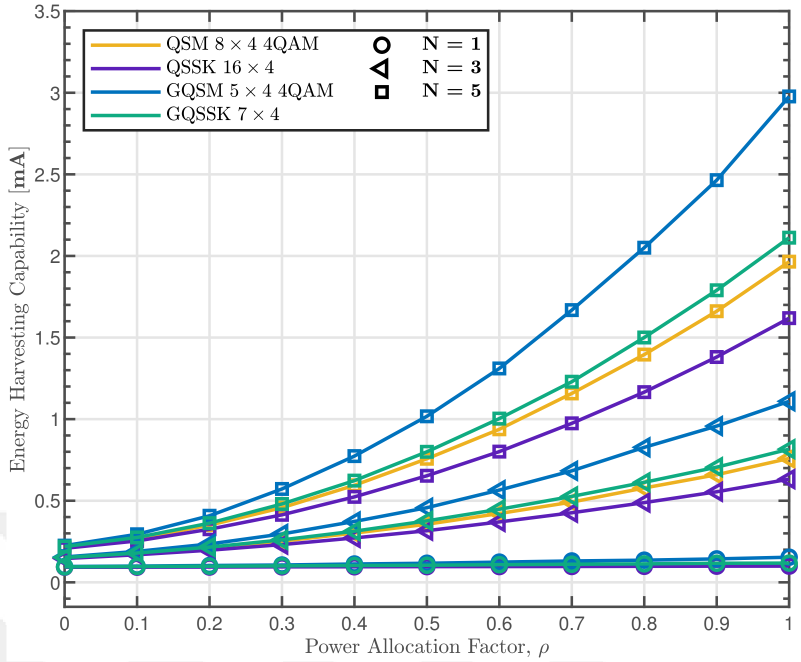

Figure 3.3: The energy harvesting capability (z_{DC}) comparison of QSM schemes with $\eta = 8$ for different N values with respect to varying power allocation factors, the EH is located at $d = 1.5$m from the WPTx.

with a reduced total number of antennas, such as GQSM and GSSK. Thus, dividing λ_u^2 among fewer antennas is profitable to leverage the strategic advantages of AN in terms of energy harvesting capability. Nonetheless, from the information harvesting perspective, increasing the total number of transmit antennas enhances the spectral efficiency of the IH system, allowing the transmission of more information. *Comparison with Benchmark Schemes:* We compare the best and worst cases of the IH mechanism, namely GQSM and SSK, with benchmark schemes in Fig. 3.4 so as to highlight the advantages of the IH mechanism in terms of far-field WPT range. We assume that 70% of the power is allocated for energy harvesting in the MU-SWIPT case, and 70% of the transmitted frame is allocated for energy harvesting in the TS-SWIPT case. The IH system consistently outperforms the considered benchmark schemes, particularly in the scenario with $N = 5$, as the parameters d and ρ increase. Even when $N = 1$, the IH mechanism demonstrates its superiority against benchmark schemes, except in the case where ρ exceeds 0.6 for SSK. It is

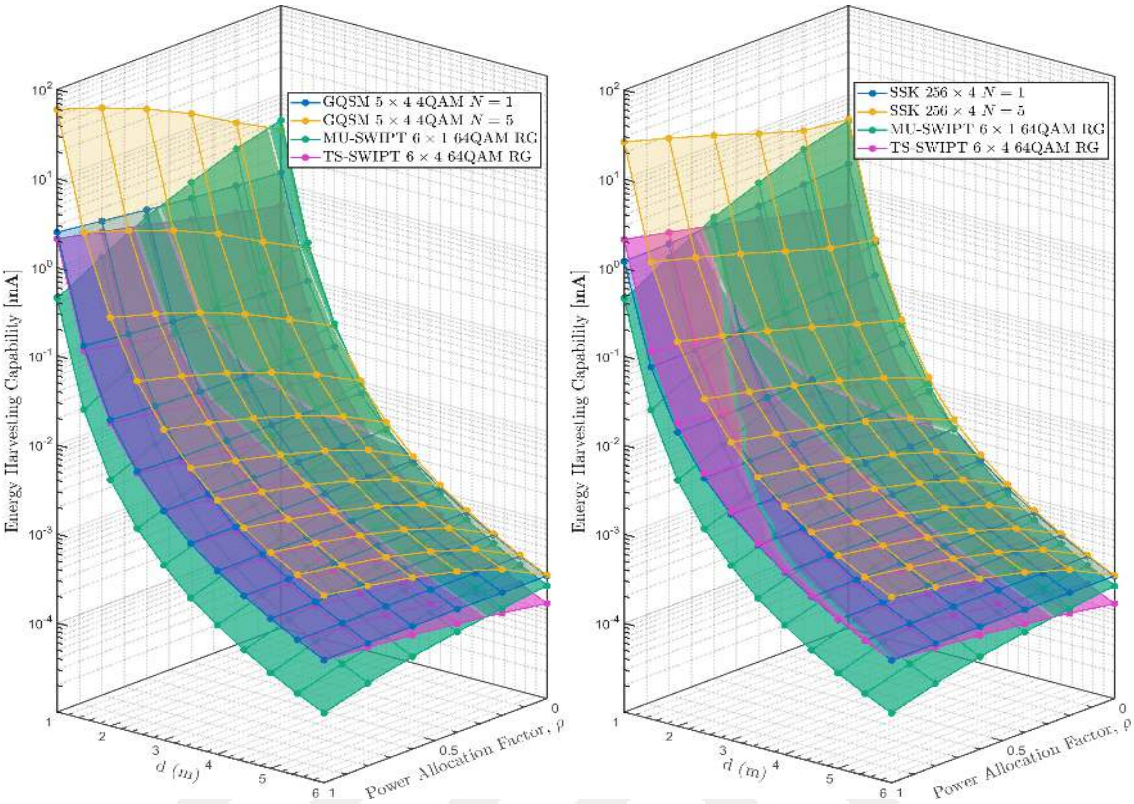

(a) (b)

Figure 3.4: Comparison of the energy harvesting capability (z_{DC}) for the IH mechanism (a) GQSM and (b) SSK with benchmark schemes across varying distances and power allocation factors.

important to note that allocating 70% of the resources for RF energy harvesting is generally unfeasible for SWIPT systems, which prioritize allocating most resources to WIT rather than WPT, as presented in [Zhou et al., 2013]. Despite this generous allocation, the IH system underscores its superiority in terms of range and energy harvesting capability. Notably, the IH mechanism adeptly leverages the benefits of AN, resulting in a secure and more efficient WPT mechanism through the use of IM techniques.

Furthermore, in the MU-SWIPT system, allocating P_T between information and energy signals is required, with both transmitted across all the transmit antennas. Additionally, deploying MF demands an equivalent number of RF chains to

Table 3.3: RECEIVED POWER for IH and SWIPT.

WIPT Mechansim		Approx. d at received signal strength		
		-5 dBm	-10 dBm	-20 dBm
Information	$N = 1$	1.2m	1.4m	1.8m
Harvesting	$N = 5$	1.5m	1.8m	2.3m
MU-SWIPT	70%	1.0m	1.1m	1.5m
TS-SWIPT	70%	1.1m	1.2m	1.6m

the number of transmit antennas, leading to increased power consumption at the transmitter. Meanwhile, the power consumption of the IH mechanism remains unaffected by the total number of antennas. Therefore, fewer RF chains are sufficient to capitalize on the benefits of IM schemes, contributing to a simpler and more power-efficient transmitter design [Basar et al., 2017]. In Table 3.3, we assess our system under average received signal strength constraints of $\{-5, -10, -20\}$ dBm to provide practical insights into the IH mechanism concerning rectenna sensitivity [Kim et al., 2019], [Ayir and Riihonen, 2023]. The evaluation is based on identical setups depicted in Fig. 5(a) at $\rho = 0.4$. Our findings reveal that as N increases, the IH mechanism extends the range at the specified received signal strengths. Additionally, within these distances, the energy harvesting capability illustrated in Fig. 5(a) outperforms benchmarks, except in the case where the MU-SWIPT method outperforms the IH mechanism for $N = 1$.

3.4.2 Error performance

In this subsection, we investigate the BER performance of the proposed IM-based IH mechanism and present numerical results to support its merits. The BER of the IH mechanism for all IM schemes is plotted in Figs. 3.5 and 3.6 to illustrate the impact of multitone signals on information harvesting performance. Within the IH mechanism, N distinct subbands experience the same channel gains between the WPTx and IR, with AWGN added to those subbands per receive antenna. Consequently, the increase in N results in more noise in the received signal vector,

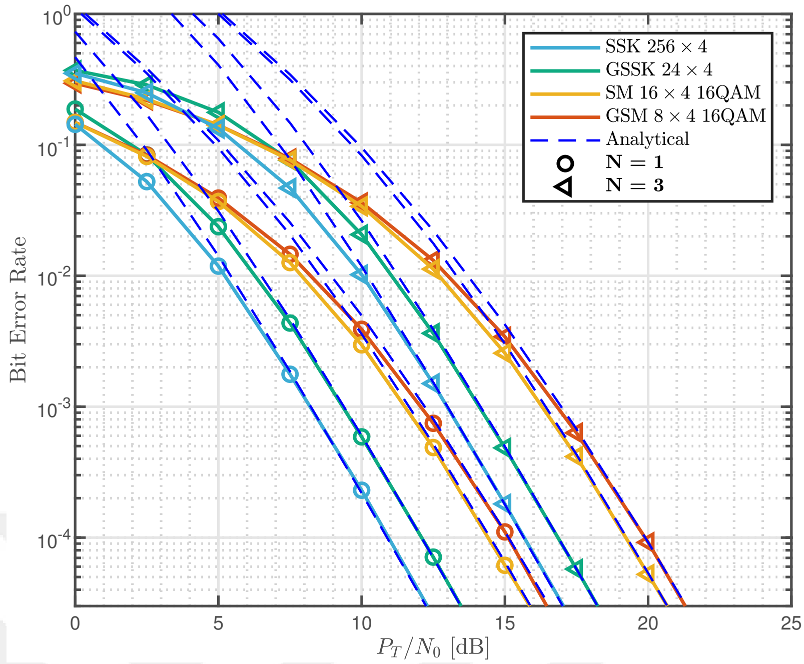

Figure 3.5: The ABER comparison at the IR for SM schemes with $\eta = 8$, $\rho = 0.2$ and for varying N parameters.

detrimentally affecting the information-decoding process. Simulation results are validated with analytical results provided in (3.20) for the IR. As expected, the analytical curves coincide with simulation results as P_T/N_0 increases. The BER of each IM scheme for single subband transmission is approximately 5 dB better than in the case where $N = 3$. Thus, there is a non-trivial tradeoff between the z_{DC} and the BER performance of the IH architecture. Figs. 3.5 and 3.6 also illustrate that best performance results are achieved when all bits are modulated in the spatial domain, particularly SSK and QSSK consistently exhibit superior results compared to the others. Thus, increasing the number of modulated bits in the spatial domain generally enhances the performance of IM schemes. Nonetheless, generalized variants of these techniques, such as GSSK, GQSM, and GQSSK, yield inferior outcomes due to the fact that generalized IM techniques introduce spatial correlation in the spatial domain, adversely affecting the IH system's performance in the end.

Comparison with Benchmark Schemes: In Fig. 3.7, we compare the BER per-

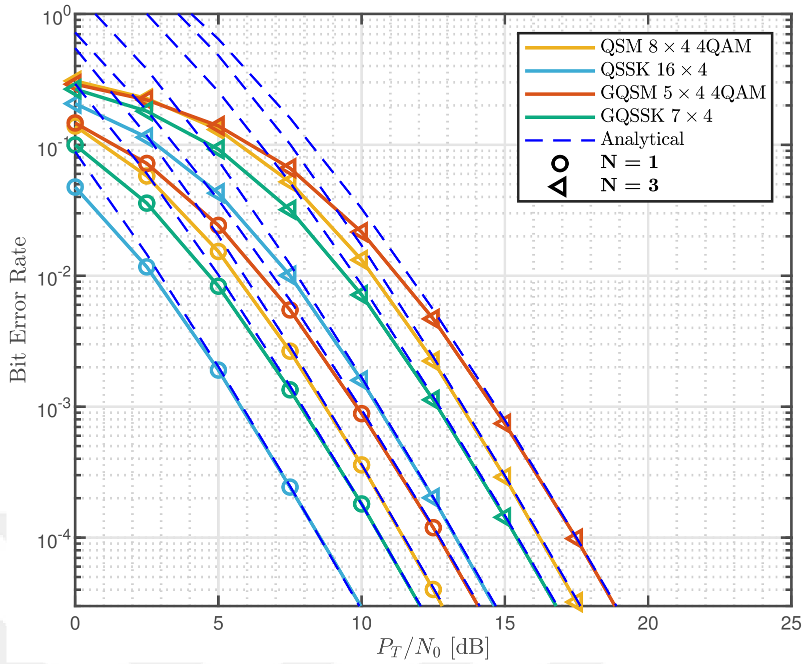

Figure 3.6: The ABER comparison at the IR for QSM schemes with $\eta = 8$, $\rho = 0.2$ and for varying N parameters.

formance of the IH mechanism, using SSK, QSSK, GSM, and GQSM techniques, against benchmark schemes that utilize 64-QAM and 256-QAM for WIT. For the MU-SWIPT and TS-SWIPT cases, 70% of the power and the transmitted frame are assigned for WIT, respectively. In the case of $N = 1$, the IH mechanism outperforms benchmarks across all IM schemes, except in the TS-SWIPT 64-QAM scenario against GSM. Noteworthy is the superior performance of QSSK over the MU-SWIPT 64-QAM case when $N = 3$. Remarkably, the spectral efficiency of the 64-QAM case for both benchmark schemes is only half that of the IM schemes. When the spectral efficiency of the benchmark schemes aligns with that of the IM schemes, the IH mechanism demonstrates superior BER results for $N = 3$ and $N = 5$ compared to the MU-SWIPT 256-QAM case. However, the results are almost identical for GSM, while the TS-SWIPT case outperforms GSM and GQSM when $N = 5$. Unlike the close BER performance of the IH mechanism to the TS-SWIPT case for $N = 3$ and $N = 5$, the IH mechanism reveals significant energy harvesting capability in the identical setup. Hence, the IH mechanism's superiority is attributed to its utilization

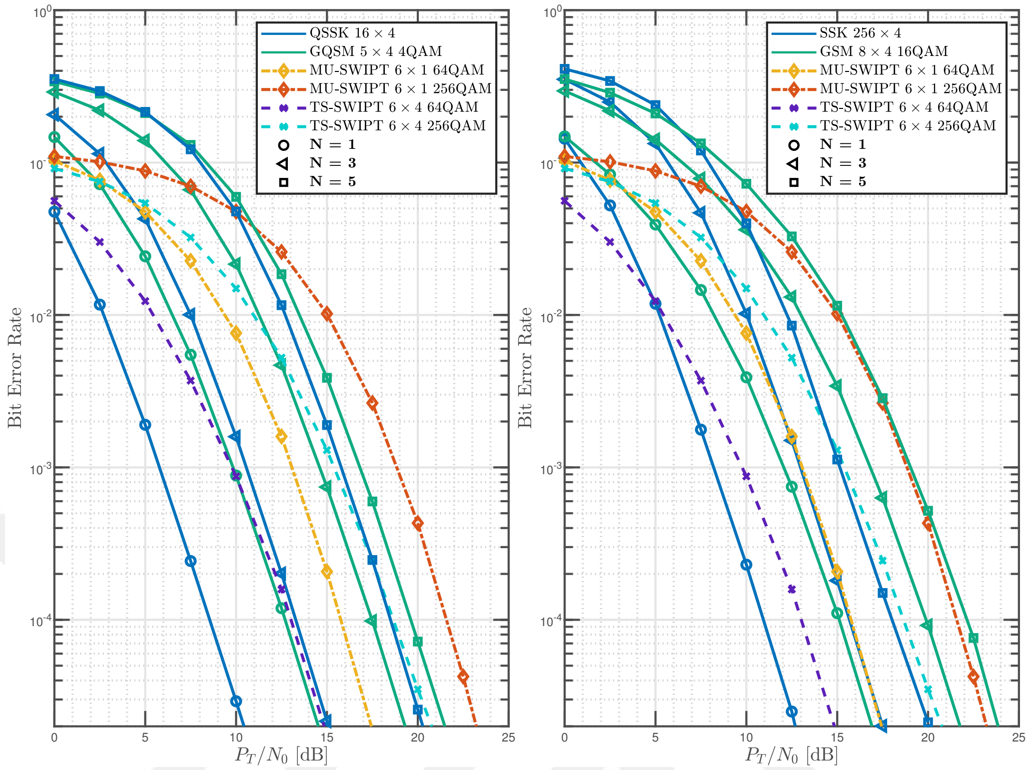

(a) (b)

Figure 3.7: The comparison of ABER among benchmark schemes with the IH mechanism: (a) QSSK and GQSM, and (b) SSK and GSM, where $\eta = 8$, $\rho = 0.2$, and varying N values.

of the antenna domain for conveying information, setting it apart from benchmark schemes. Consequently, the IH mechanism can establish a reliable communication channel with the contribution of IM schemes without disrupting the ongoing far-field WPT mechanism.

The impact of AN on Eve's BER performance is explored in Fig. 3.8, including the use of GSSK with $N_T = 7$, GSM with $N_T = 4$, and 4-QAM, QSSK with $N_T = 4$, as well as GQSSK with $N_T = 4$ schemes where $N = \{1, 3, 5\}$. Analytical curves become more precise as the P_T/N_0 increases. The simulation and analytical curves closely align in the high P_T/N_0 range, particularly when it exceeds 5 dB. Fig. 3.8 illustrates that the introduction of AN on larger subbands significantly disrupts Eve's ability to decode the transmitted data, resulting in a substantial

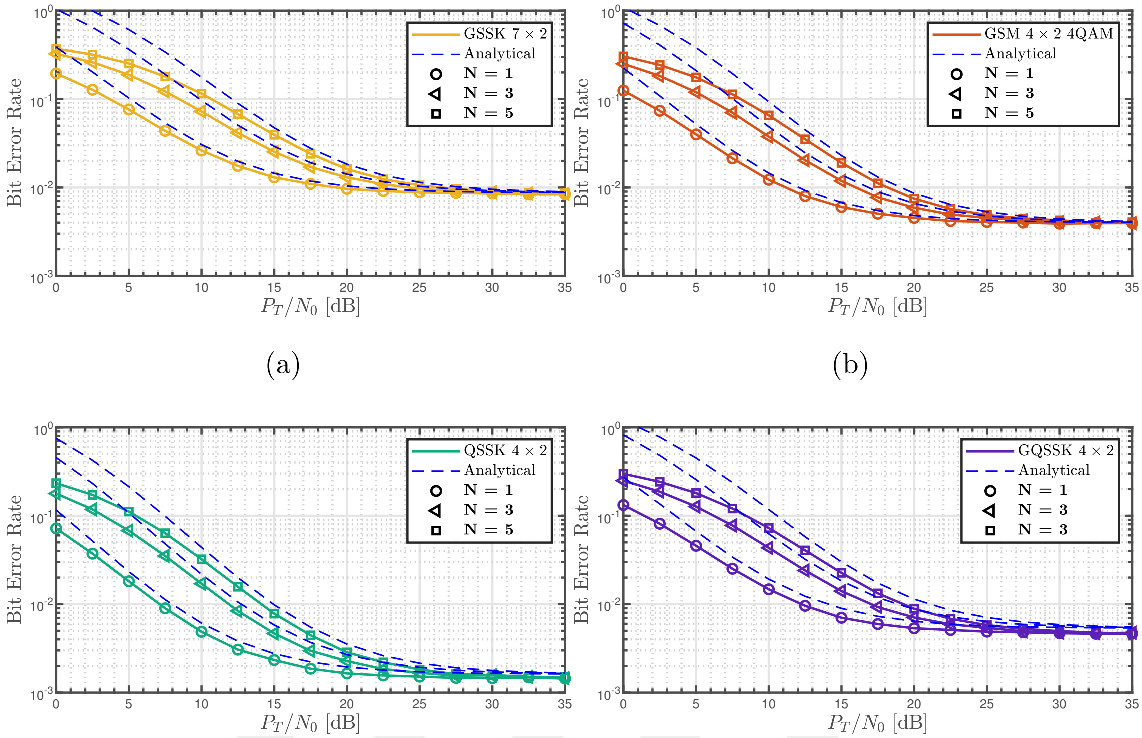

(a) (b) (c) (d)

Figure 3.8: The ABER comparison of Eve for (a) GSSK, (b) GSM, (c) QSSK, and (d) GQSSK with $\eta = 4$, $\rho = 0.025$, and varying values of the parameter N.

deterioration in Eve's BER performance, which accounts for the protective effect of the IH mechanism against eavesdropping attempts.

3.4.3 Secrecy analysis

Now, we investigate the ESR of the proposed IM-based IH schemes, including GSSK, QSSK, QSM, and GQSM, where $N_T = 4$, $N_a = 2$, $N_{IR} = 2$, and 4-QAM is utilized when necessary, resulting in varying spectral efficiencies among the IM schemes with ρ set to 0.2 and 0.6, respectively. Figs. 3.9a and 3.9b reveal that for $\rho = 0.2$, the GSM scheme provides higher secrecy compared to the others, while for $\rho = 0.6$, QSSK outperforms all the schemes at low P_T/N_0 values with the expense of higher decoding complexity. In the high P_T/N_0 region, the GQSM scheme yields the best performance.

Comparison with Benchmark Schemes: In Figs. 3.9(a) and 3.9(b), ESR results

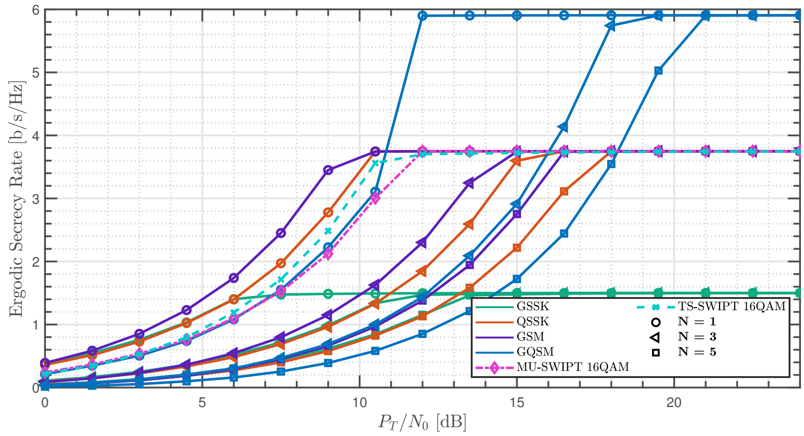

(a)

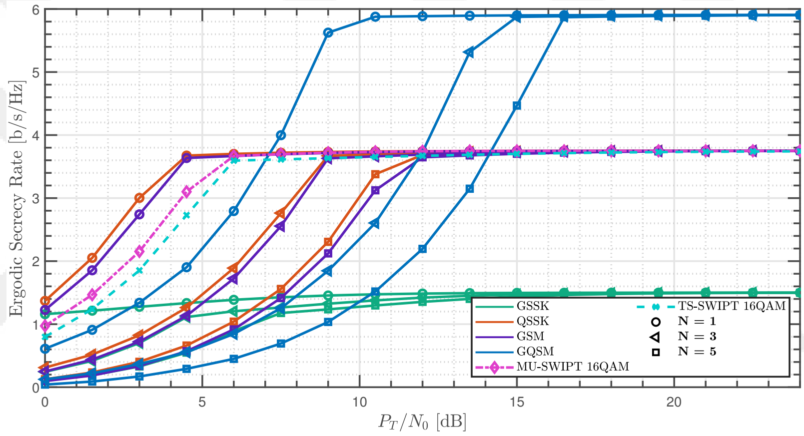

(b)

Figure 3.9: The ESR comparison of the IH mechanism with benchmark schemes (a) $\rho = 0.2$ and (b) $\rho = 0.6$, with varying N values.

are also compared with benchmark schemes, where $N_T = 4$, $N_{\text{IR}} = 1$ for MU-SWIPT, and $N_{\text{IR}} = 2$ for TS-SWIPT, both employing 16-QAM. In MU-SWIPT and TS-SWIPT cases, 70% of the power and the transmitted frame are allocated for WIT, respectively. In scenarios where $N = 3$ and $N = 5$, benchmark schemes initially exhibit better results compared to the IH mechanism at low P_T/N_0 values. However, as P_T/N_0 increases, ESR saturates for all cases, and the results become indistinguishable after reaching specific P_T/N_0 values except for the GQSM scheme, which persists in outperforming benchmarks. Moreover, allocating additional power to generate AN proves crucial in enhancing the secrecy performance of the IH mechanism, effectively preventing Eve from detecting injected data during information seeding. Additionally, the ESR performance of the IH mechanism is negatively influenced by an increasing number of subbands.

It is worth mentioning that the IH mechanism demands an ongoing WPT mechanism and $N_R > 1$ to achieve reliable WIT, as the information bits are injected into multitone waveforms through IM schemes. In contrast, the SWIPT systems can achieve WPT and WIT functions separately without relying on each other, and reliable communication can be achieved with $N_R = 1$ [Ponnimbaduge Perera et al., 2018]. While opting for a higher number of subbands is advantageous for wireless power transmission, it is essential to carefully consider the cumulative impact of channel effects and Gaussian noise on the receiver side since these factors could degrade overall system performance, particularly in terms of WIT. Furthermore, an increased N parameter of multitone signals induces high PAPR characteristics, which result in unwanted amplitude distortion in the transmit signal [Park et al., 2021] such that a proper transmitter design for the IH mechanism is needed while it is likely to design a SWIPT system which is not based on multitone signals.

Chapter 4

OFDM-BASED INFORMATION HARVESTING

This chapter delves into a novel IH mechanism integrated with an OFDM-based far-field wireless power transfer system. The advantages of this proposed IH mechanism are explored in terms of harvested energy, achievable rate, and reliability.

4.1 OFDM-based IH System

Fig.4.1 represents a typical implementation of the OFDM-based IH mechanism. Herein, the WPTx serves as a module supplying far-field power transfer to the EHs along with embedding the information in a choice of active subcarrier set, so-called *information seeding*, while IRs designed for decoding the information out of emitted WPT signal, so called *information harvesting* in [Ilter et al., 2022b]. Note that the IR and EH are not necessarily separate devices, so the IR can act as an EH device provided that it is in the WPT service area and the details regarding each module of the implementation will be described in the following subsections.

4.1.1 OFDM-based WPT transmission

In the considered scenario, the WPT mechanism is assumed to operate over a frequency-selective Rayleigh fading channel. The WPT transmitter emits OFDM waveforms where N_{FFT} is the number of OFDM subcarriers, in other words, the size of the fast Fourier transform (FFT). Each OFDM block is divided into G subblocks, $G = N_{\text{FFT}}/N$, and the localized subcarrier grouping is applied to N subcarriers in each subblock as in [Wen et al., 2016]. Unlike the conventional OFDM approach, the proposed IH mechanism considers only a subgroup of active subcarrier indices. The mapping operation is then performed for the indices of the active subcarriers, K in a considered subblock as in [Wen et al., 2016], so the available information

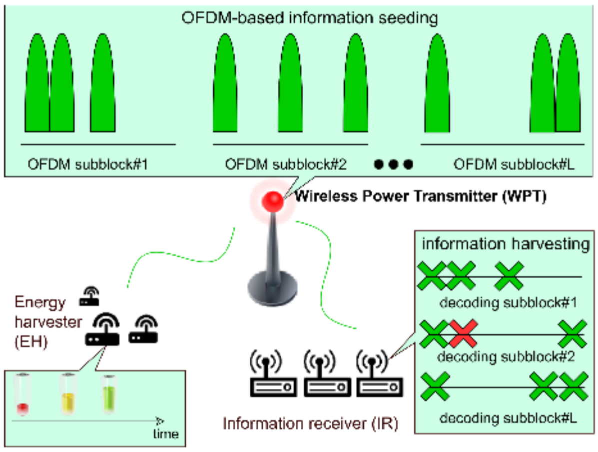

Figure 4.1: The block diagram of OFDM-based IH when both EH and IR exist in the service area.

block is mapped into an active subcarrier set such that $K \leq N$. It was known that the maximum number of information bits per channel use, spectral efficiency, η, can be mapped into the active subcarrier set indices can be expressed as:

$$\eta = \left\lfloor \log_2 \binom{N}{K} \right\rfloor . \tag{4.1}$$

Under this assumption, even if the emitted OFDM waveform does not have any information component itself, the information can be carried inside the indices of the corresponding active subcarrier set out of $L = 2^\eta$ possibilities.

Particularly, the gth OFDM subblock can be expressed as $\mathbf{x}^g = [x^g(1), ..., x^g(N)]$ where $x^g(i)$ is the emitted WPT signal corresponding to ith subcarriers when it is active. For an inactive subcarrier, $x(i) = 0$ holds for $i \in \{1, \ldots, N\}$. For the WPT signal, Zadoff-Chu sequences [Nakamoto et al., 2022] and RG signals [Kim et al., 2020] are used in K active subcarriers. For the first one, the amplitude is constant, and the phase is expressed by [Nakamoto et al., 2022]

$$\theta_x = \exp\left(-j\frac{\pi M_{\mathrm{ZC}} i(i+1)}{K}\right), \quad i = 0, 1, \ldots, N_{\mathrm{ZC}}, \tag{4.2}$$

where M_{ZC} indicates the Zadoff-Chu sequence root index, and N_{ZC} indicates the Zadoff-Chu sequence length, which is K times the number of the OFDM subblock. It was shown in [Nakamoto et al., 2022] that employing Zadoff-Chu sequences results in higher rectification efficiency and lower PAPR than M-QAM and CW for high input power region.

Then, the OFDM subblock is processed by the inverse FFT algorithm where the output is the time-domain version of $\mathbf{x}$ such that giving N_{FFT} time samples is given by,

$$\mathbf{x}_T = \text{IFFT}\left\{\left[\mathbf{x}^1, \ldots, \mathbf{x}^G\right]\right\} = \frac{N}{\sqrt{K}}\mathbf{W}^H_{N_{\text{FFT}}}\mathbf{x}. \tag{4.3}$$

Herein, $\mathbf{W}_{N_{\text{FFT}}}$ is the discrete Fourier transform (DFT) matrix such that $\mathbf{W}^H_{N_{\text{FFT}}}\mathbf{W}_{N_{\text{FFT}}} = N_{\text{FFT}}\mathbf{I}_{N_{\text{FFT}}}$ where $\mathbf{I}_{N_{\text{FFT}}}$ is the identity matrix with the dimension of $N_{\text{FFT}} \times N_{\text{FFT}}$. Then, the cyclic prefix (CP) samples with length of P can be added at the beginning of $\mathbf{x}_T$. Finally, after parallel to serial (P/S) and digital-to-analog conversion, the OFDM waveform is transmitted from the WPT.

The channel between the WPT-EH is considered a slowly time-varying multipath Rayleigh fading channel where a channel impulse response can be expressed as $\mathbf{h}_T = [h_T(1), \ldots, h_T(v)]$ where v is the number of channel taps and each tap is modelled as circularly symmetric complex Gaussian random variables, $h_T(i) \sim \mathbb{CN}(0, \sigma_\delta^2)$ and $\sum \sigma_\delta^2 = 1$ along with $P > v$. Then, the equivalent frequency domain input-output relationship of the considered OFDM scheme can be expressed as

$$y_F^{\text{EH}}(i) = h_F(i)\, x(i) + \omega_F(i), \tag{4.4}$$

where $y_F^{\text{EH}}(i)$, $h_F(i)$ and $\omega_F(i)$ are the CP-contained received signals at the EH, the channel fading coefficients which can be formulated as $h_F(i) = \sum h_T(v)\, e^{2j\pi(i-1)(v-1)/N_{\text{FFT}}}$ and the noise samples in the frequency domain, respectively. The distribution of $\omega_{\mathbb{F}}$ is $\mathcal{CN}(0, N_{0,F})$, and its variance in frequency domain relates with noise variance in the time domain such that $N_{0,F} = KN_{0,T}/N$.

For a more spectrally efficient design, the unused subcarriers in the proposed IH mechanism can be utilized for transmitting a set of symbols selected from a different constellation as in dual-mode OFDM mechanism [Mao et al., 2016]. In this case, K subcarriers emit the WPT signal and the remaining $N - K$ subcarriers can be reserved for modulated symbols where the modulation order of the selected constellation is M.

4.1.2 Decoding at the IR

Similar to the WPT-EH link, the WPT-IR link is modeled with a slowly time-varying multipath Rayleigh channel denoted as $\mathbf{g}_T$. The goal of the IR is to retrieve the information that was mapped into active transmit indices from the received OFDM waveform so the IR can decode the information bits. To do so, the IR first removes the appended CP from the received signal and then implements a decoding mechanism to estimate the active subcarrier index set used in the WPT for a given OFDM subblocks. Herein, two different detection algorithms can be implemented based on the implementation complexity constraint in the IR:

Maximum Likelihood (ML) decoding

The ML detector considers all possible active subcarrier index combinations for a given OFDM subblock so it aims to find an active subcarrier set, $\hat{\mathbf{I}}_{\text{IR}}$, out of L possibilities which minimizes the following metric:

$$\hat{\mathbf{I}}_{\text{IR}} = \arg\min_{l \in L} \|\mathbf{y}_F^{\text{IR}} - \hat{\mathbf{g}}_{l,F}\mathbf{x}\|^2. \tag{4.5}$$

Herein, $\mathbf{y}_F^{\text{IR}}$ is the received signal vector, $\hat{\mathbf{g}}_{l,F}$ corresponds to lth possible channel coefficients set in the frequency domain, and $\mathbf{x} = [x_1, 0, \ldots, x_K, 0]$ is the WPT signal in the frequency domain where zero entries correspond to inactive subcarrier. It can be easily shown that the total computational complexity of the ML detector in (4.7), in terms of complex multiplications, is $\mathcal{O}\left(LK^k\right)$ per subblock. Considering this, the ML detector becomes impractical for larger values of N and K.

Log-Likelihood Ratio (LLR) decoding

ML decoding brings considerable computational complexity since all possible active subcarrier sets are considered for a given $\{N, K\}$ so it makes the proposed OFDM-based IH practical for only limited scenarios. Alternatively, the LLR detector carries out the logarithm of the ratio of a posteriori probabilities by estimating the status of lth subcarrier as being idle or active individually. Then, the decision metric for lth subcarrier can be formulated as $\lambda_l = \ln\left(\Pr\left(A_l\right)/\Pr\left(\bar{A}_l\right)\right)$, where A_l represents a case where the l-th subcarrier is active while $\bar{A}_l$ does idle and using [(12), [Basar et al., 2013]] λ_l can be formulated as

$$\lambda_l = \ln K - \ln (N-K) + \frac{|y_F(l)|^2}{N_{0,F}} + \ln \sum_{k=1}^{K} \left(\exp \left(-\frac{1}{N_{0,F}} |y_F(l) - g_F(l) x_{F,k}|^2 \right) \right), \tag{4.6}$$

where $x_{F,k}$ corresponds to kth WPT signal where the total WPT signal set consists of K symbols. To eliminate the cases of decoding a catastrophic set in the IR, resulting from $\log_2 \binom{N}{K} > \eta$ and the LLR decoder considers each subcarrier detection individually, once (4.6) is calculated for all subcarriers, the LLR detector can estimate active subcarrier after L possibilities are taken into consideration in the IR as in the following:

$$\hat{\mathbf{I}}_{\mathrm{IR}} = \arg \max_{\mathbf{i}_l, l \in L} \sum \lambda_l. \tag{4.7}$$

The computational complexity of the LLR detector in (4.7), in terms of complex multiplications, is $\mathcal{O}(K)$ per subcarrier is the same as that of the classical OFDM detector.

4.2 Performance Metrics

In this section, the performance metrics used in the evaluation of the proposed scheme from energy harvesting and data communication aspects wil be described.

4.2.1 Energy harvesting capability

Once the WPT transmits power transfer waveforms into a service area, the EH is expected to convert the received RF waveforms into DC output power through a rectenna. The rectenna's output DC power, under perfect matching and an ideal low-pass filter, is directly related to the quantity given in (3.2).

4.2.2 Error performance

Now, the reliability of OFDM-based IH mechanism is investigated in terms of the bit error rate at the IR. To do so, the pairwise error probability (PEP), which considers the error event resulting from an inaccurately decoded active subcarrier set corresponding to the correct one, is considered. At this point, the channel coefficients in frequency domain can be expressed in terms of time domain channel coefficients such that $\mathbf{g}_F = \mathbf{W}_{N_{\text{FFT}}}\mathbf{g}_T^0$, where $\mathbf{g}_T^0$ is the zero-padded version of $\mathbf{g}_T$. It was known that the Fourier transform of a Gaussian vector gives another Gaussian vector but the elements of $\mathbf{g}_F$ is no longer uncorrelated. The correlation matrix of $\mathbf{g}_F$ is expressed as $\mathbf{K} = \mathbb{E}_{\mathbf{g}_F}\left[\mathbf{g}_F\mathbf{g}_F^H\right]$ and because $\mathbf{K}$ is a Hermitian Toeplitz, the PEP for a single block can determine the overall PEP performance [Basar et al., 2013] and the unconditional PEP (UPEP) of the OFDM-based IH scheme can be obtained from

$$\mathrm{PEP}_{\mathbf{x_F}\rightarrow\hat{\mathbf{x}}_\mathbf{F}} = \frac{1/12}{\det\left(\mathbf{I}_\mathrm{n} + \mathrm{q}_1\mathbf{K}_\mathrm{n}\mathbf{A}\right)} + \frac{1/4}{\left(\mathbf{I}_\mathrm{n} + \mathrm{q}_2\mathbf{K}_\mathrm{n}\mathbf{A}\right)}, \tag{4.8}$$

along with $q_1 = 1/\left(4N_{0,F}\right)$, $q_2 = 1/\left(3N_{0,F}\right)$, and $\mathbf{A} = \left(\mathbf{x}_F - \hat{\mathbf{x}}_F\right)$ [Basar et al., 2013]. Herein, $\mathbf{K}_n$ is a $n \times n$ submatrix centered along the main diagonal of the matrix of $\mathbf{K}$. Then, average bit error rate (ABER) is bounded by

$$\overline{P}_b \leq \frac{1}{\eta}\frac{1}{L}\sum_{i_1=1}^{L}\sum_{i_2=1, i_1\neq i_2}^{L} N_b\left(i_1, i_2\right)\mathrm{PEP}_{\mathbf{x}_{\mathrm{F},\mathrm{i}_1}\rightarrow\mathbf{x}_{\mathrm{F},\mathrm{i}_2}}, \tag{4.9}$$

where $N_b\left(i_1, i_2\right)$ is the number of erroneous bits resulting from decoding active carrier set, i_2, when i_1 is transmitted.

4.2.3 Achievable rate

While BER analysis is insightful for assessing the error reliability of the OFDM-based IH mechanism, achievable rate analysis can truly unveil its potential and discover the maximum information transmission capacity. To do so, the achievable rate of OFDM-based IH mechanism can be expressed as [Wen et al., 2016]

$$\begin{aligned} R_{\text{OFDM-IH}} &= \frac{\log_2\left(L\right)}{N} - \left(\log_2\left(e\right) - 1\right) - \frac{1}{NL}\sum_{l=1}^{L} \\ &\times \mathbb{E}_{\mathbf{g}_F,\omega_F}\left[\log_2\left(2^N e^{-\left|\mathbf{w}_F\right|^2} + \sum_{l'=1}^{L}\prod_{i=1}^{L}\xi\left(w_F\left(i\right), g_F\left(i\right)\right)\right)\right], \end{aligned} \tag{4.10}$$

where perfect CSI at the information receiver is assumed and $\xi\left(\cdot,\cdot\right)$ is defined in [eq.(13), [Wen et al., 2016]].

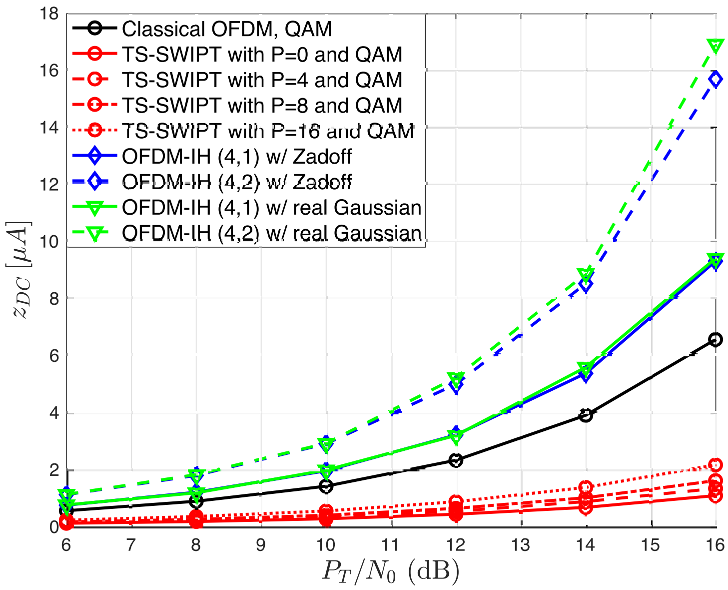

Figure 4.2: Energy harvesting capability (z_{DC}) when the EH is located at $d = 5$m with respect to varying power budget values, P_T/N_0.

4.3 Numerical Results

Now, the performance of the proposed OFDM-based IH mechanism is evaluated in terms of energy harvesting capability, achievable rate, and BER over different (N, K) values. To demonstrate its superiority, classical OFDM and TS-SWIPT mechanism [Buckley and Heath, 2021] was used as a baseline where P denotes the number of extra subcarriers taken from the OFDM data frame for energy harvesting. In the EH, the pair of $\{k_2, k_4\}$ is considered as $\{0.0034, 0.3829\}$, R_{ant} is set to 50Ω [Kim et al., 2020]. For the WPT signal, since the information is only conveyed through the indices of the active subcarrier set, the Zadoff-Chu sequences which have a smaller PAPR are preferred where $M_{\text{ZC}} = 13$ in (4.2).

To start with, Fig. 4.2 illustrates the energy harvesting capability of the considered cases. The channels between the WPT and the EH are modeled with Rayleigh fading along with $v = 10$ taps and the following path-loss model is considered; $PL\,[\text{dB}] = 35.3 + 37.6 \log_{10}(d)$, where d is the distance between the WPT and an EH in meters. In order to keep the same maximum achievable spectral efficiency,

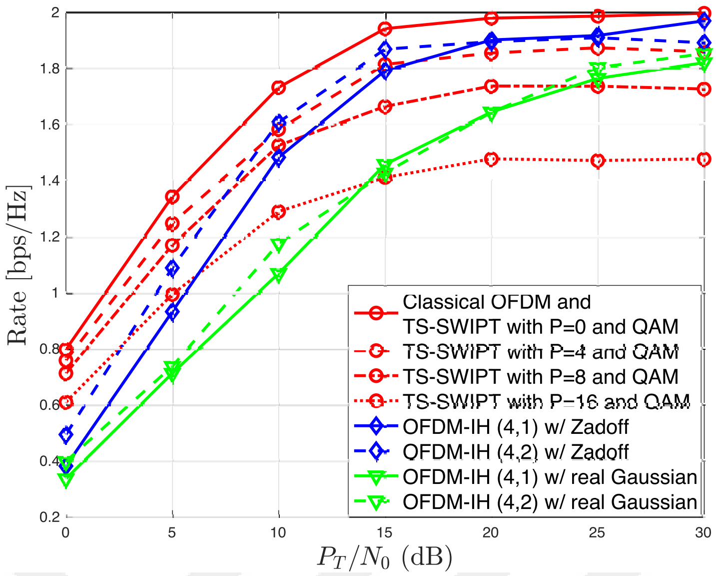

Figure 4.3: Achievable rate comparison of the proposed OFDM-based IH mechanisms deploying Zadoff-Chu and real Gaussian WPT waveform with classical OFDM and TS-SWIPT [Buckley and Heath, 2021] with respect to varying power budget values, P_T/N_0.

which is η for OFDM-IM scheme and $\log_2(M)$ for TS-SWIPT and classical OFDM ones, the transmitter deploys the following setting for corresponding case: $N = 4$, $K = \{1, 2\}$ and QAM modulation for those simulations. It can be clearly seen that the proposed OFDM-IH scheme outperforms classical OFDM and TS-SWIPT mechanisms by utilizing its advantage of being a far-field power transfer mechanism along with WPT waveform, whereas there is negligible difference between Zadoff-Chu and RG signaling. As expected, higher P values result in more harvested energy, but it is still far from the classical OFDM mechanism where all symbols are used for energy harvesting. Then, the achievable rates of the considered scenarios are plotted in Fig. 4.3. Due to its constant amplitude, the Zadoff-Chu outperforms RG signaling from a communication perspective, and while the achievable rate of OFDM-IM is worse under lower power budget, it converges to the classical OFDM achievable rate as higher power for both signaling schemes.

Now, the quality of the bits transmitted over the indices of the active OFDM

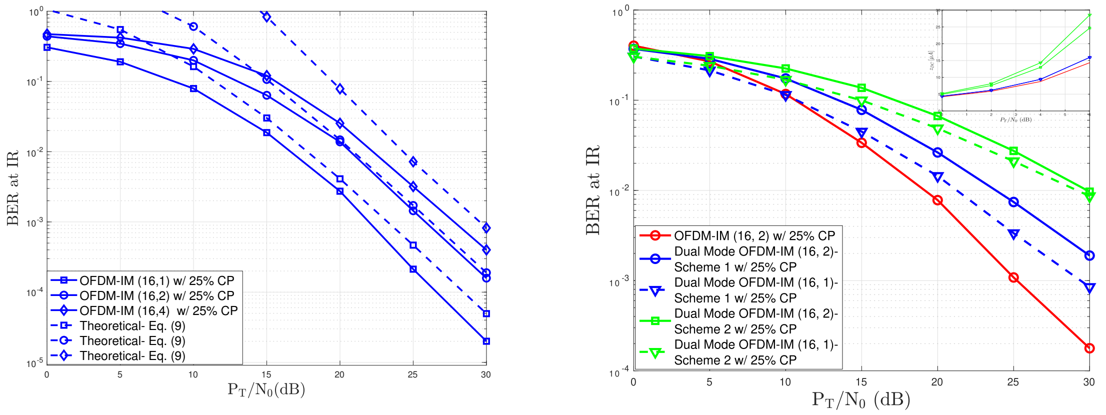

(a) (b)

Figure 4.4: (a) BER results of the proposed OFDM-based IH mechanism, (b) BER results and the energy harvesting capability (z_{DC}) of the proposed dual-mode IH mechanism along with given N and K values over varying power budget values P_T/N_0 at the IR.

subcarrier set is investigated in terms of BER in Fig. 4.4(a) where $v = 4$ is assumed. Herein, the calculation of the BER lies in comparing the transmit active subcarrier set vector and the estimated one at the IR and Gray-coded index mapping is used. Initially, the curves validate the tightness of the BER expression for higher P_T/N_0 values. Considering its practicality, LLR decoding is considered for all cases. It can be seen that a less active subcarrier during OFDM subblock transmission introduces better reliability.

Furthermore, in order to show the feasibility of dual-mode OFDM-based IH, two different schemes are considered for the choice of dual mode constellation. Scheme 1 deploys QAM constellation for $N-K$ subcarriers, inactive ones in previous cases, in each OFDM symbol. In Scheme 2, $N-K$ subcarriers are mapped into Zadoff-Chu sequences with different M_{ZC} values, $M_{\text{ZC}} = 9$ for $N-K$ subcarriers, given in (4.2) where it is assumed that two different M_{ZC} values are known a priori at the IR. Fig. 4.4(b) illustrates that the dual-mode OFDM-based IH sacrifices reliability, whereas energy harvesting capability has been improved considerably. As expected, deploying two different Zadoff-Chu sequences in Scheme 2 outperforms Scheme 1 where QAM is selected.

Chapter 5

TIME INDEX MODULATION-DRIVEN STANDALONE RIS MECHANISM FOR SYMBIOTIC RADIO

This chapter introduces an SR environment where an RIS functions as an BD while maintaining its operations through WEH. The practical rectenna, constant-linear-constant (CLC) model is examined for the standalone RIS architecture and the EH. Additionally, the PTx utilizes the TIM strategy to transmit power and information to the receiving ends. An LLR-based detector is proposed for the TIM-driven SR scheme, and the performance metrics of the proposed scheme are investigated in terms of BER at the PRx and harvested DC power at the standalone RIS and EH.

5.1 Symbiotic Radio Model

In the proposed scheme, the primary system, which consists of a single antenna PTx and an M_{R} antenna PRx, relies on active RF transmission technology. The secondary system comprises a standalone RIS with $N = N_1 + N_2 + N_3$ UCs and a single antenna EH, both of which are passive IoT devices. These passive IoT devices harness the power and spectrum resources of the primary system to sustain their operations such that the primary and secondary systems rely on symbiotic relationships [Liang et al., 2020]. In Fig. 5.1, PTx leverages the TIM technique to send information to the PRx and power to the EH through the direct link and the link empowered by RIS. Therein, the RIS is partitioned into three groups: the first group, with N_1 UCs, assists the PTx transmission; the second group uses N_2 UCs as absorbers to ensure the RIS's self-sustainability through WEH by exploiting the PTx signal; and N_3 UCs in the third group are dedicated to conveying the RIS information by inducing phase shifts in the reflected signal. The PTx-RIS and RIS-PRx channels are defined as $\mathbf{h}_r \triangleq [\mathbf{h}_{r,1}, \mathbf{h}_{r,2}, \mathbf{h}_{r,3}]^T \in \mathbb{C}^{N\times 1}$ and $\mathbf{G}_d \triangleq [\mathbf{G}_{d,1}, \mathbf{G}_{d,2}, \mathbf{G}_{d,3}] \in \mathbb{C}^{N_{\mathrm{R}}\times N}$,

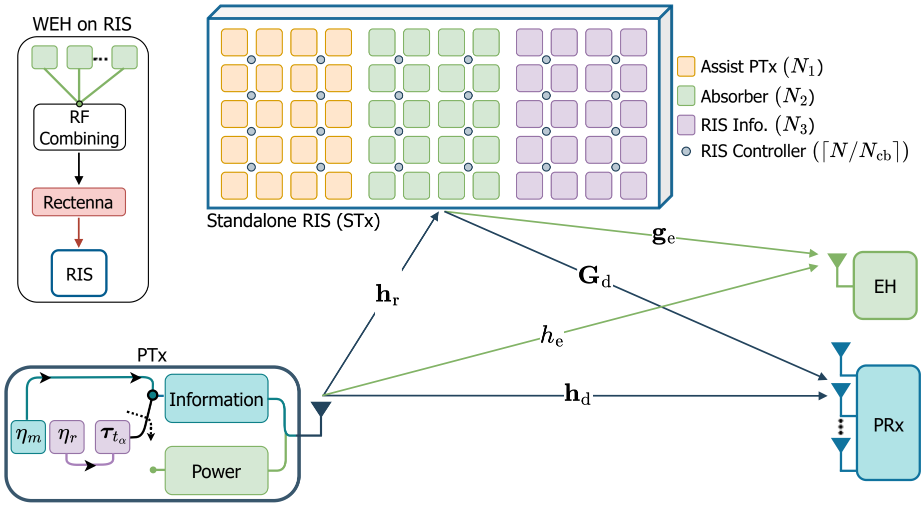

Figure 5.1: System model of TIM-driven RIS-SR scheme.

respectively, where subscripts $l = \{1, 2, 3\}$ associated with the RIS groups with $\{N_1, N_2, N_3\}$ UCs. All links follow the Rician channel model, and v-th entry of PTx-PRx, and (v, n)-th entry of RIS-PRx link can be written as:

$$h_d^v = \sqrt{\nu_p}\left(\sqrt{\frac{\kappa_p}{\kappa_p+1}} h_{d,\mathrm{LoS}}^n + \sqrt{\frac{1}{\kappa_p+1}} h_{d,\mathrm{NLoS}}^n\right), \tag{5.1}$$

$$g_d^{v,n} = \sqrt{\nu_p}\left(\sqrt{\frac{\kappa_p}{\kappa_p+1}} g_{d,\mathrm{LoS}}^{n,v} + \sqrt{\frac{1}{\kappa_p+1}} g_{d,\mathrm{NLoS}}^{n,v}\right), \tag{5.2}$$

where $v \in \{1, 2, \ldots, M_R\}$ and $n \in \{1, 2, \ldots, N\}$. Herein, ν_p and $\kappa_p \geq 0$ for $p \in \{h_d, g_d\}$ represent the path loss and the Rician factors, respectively. The terms $h_{d,\mathrm{LoS}}$, and $g_{d,\mathrm{LoS}}^{v,n}$ are the deterministic line-of-sight (LoS) components with $|h_{d,\mathrm{LoS}}^v| = |g_{d,\mathrm{LoS}}^{v,n}| = 1$ and $h_{d,\mathrm{NLoS}}^v$, and $g_{d,\mathrm{NLoS}}^{v,n}$ represent non-LoS components in which each entry is independent and identically distributed (i.i.d.) according to $\mathcal{CN}(0, 1)$. The definitions of the remaining channels follow similar principles and can be derived analogously.

5.1.1 Primary transmission model

The PTx utilizes the TIM scheme to convey information to the PRx and power to the EH over direct and RIS links. Hence, the PTx also sends bits by indexing information and power transmission stages into distinct time slots, allowing deterministic power signals to participate in information transmission. Thus, there is an ongoing information transmission even when the PTx switches to a power stage.

Information Stage

In the information stage, L information signals $x_i \in \mathcal{M}$ with a power of P_L are drawn from M-PSK/QAM constellation points, where $\mathcal{M} = \{x_i : 1 \leq i \leq M\}$. Therefore, $\eta_m = L\log_2(M)$ bits can be sent over the total block length. By leveraging TIM to alter the transmission ordering of the L information signals, $r = C(K, L)$ distinct mappings of L information signals can be achieved. Thus, additional $\eta_r = \lfloor \log_2(r) \rfloor$ bits are conveyed, such that $\eta = \eta_m + \eta_r$ bits are transmitted over one block duration that spans K transmission stages.

According to η_r bits, the time indices of L information signals are chosen from the set for each block duration, which is given by

$$\mathcal{T} = \left\{ \mathbf{t}_1 \quad \mathbf{t}_2 \quad \ldots \quad \mathbf{t}_{2^{\eta_r}} \right\}, \tag{5.3}$$

in which there are 2^{η_r} possible legitimate time-index selections out of r. After deciding on $\mathbf{t}_\alpha \in \mathbb{Z}^+$, where $\alpha \in \{1, 2, \ldots, 2^{\eta_r}\}$, the time-index vector is defined as $\boldsymbol{\tau}_{\mathbf{t}_\alpha} = \begin{bmatrix} \tau_1 & \tau_2 & \ldots & \tau_K \end{bmatrix}^T \in \mathbb{N}^{K\times 1}$, and τ_k is set to 1 at every information transmission stage, where $k = 1, 2, \ldots, K$.

Power Stage

The remaining $(K-L)$ time slots are used for deterministic power signal $\omega = \omega_I + j\omega_Q$ with a power of $|\omega|^2 = P_H$, where $P_H \geq P_L$, and τ_k is set to 0 at each power transmission stage.

By following the construction of $\boldsymbol{\tau}_{\mathbf{t}_\alpha}$, the η_m bits are mapped to the M-PSK/QAM symbols, where each symbol carries η_m/L bits. The mapping is done considering the legitimate signal set $\mathcal{S}$, which has a length of M^L and is defined as follows:

$$\mathcal{S} = \left\{ \mathbf{x}_1 \quad \mathbf{x}_2 \quad \mathbf{x}_3 \quad \cdots \quad \mathbf{x}_{M^L} \right\}. \tag{5.4}$$

Therein, $\mathbf{x}_n \in \mathcal{S}$, where $n \in \{1, 2, \ldots, M^L\}$, represents a vector of length L, $\mathbf{x}_n = \begin{bmatrix} x_{i,1}^n & x_{i,2}^n & \cdots & x_{i,L}^n \end{bmatrix}^T$ in which, $P_L = \mathbb{E}[|x_i|^2]$ is normalized to unit power.

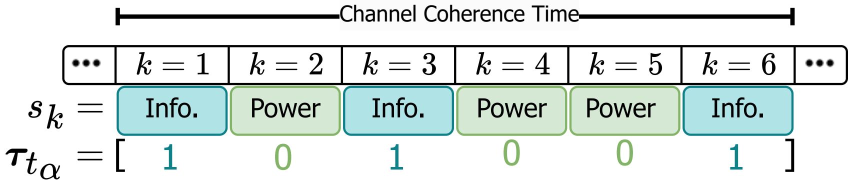

Figure 5.2: PTx transmission strategy.

Consequently, the elements of $\mathbf{x}_n$, namely the symbols, are mapped into the time slots based on $\boldsymbol{\tau}_{\mathbf{t}_\alpha}$ to initialize the transmission stage. Accordingly, the signal $s_k \in \{\mathcal{S}, \omega\}$ is transmitted at each time instant k.

In Fig. 5.2, the transmission strategy of PTx is illustrated for $K = 6$ and $L = 3$. The total block duration is assumed to be less than the channel coherence time, ensuring that the channel coefficients remain unchanged for a block of length K, though they might change from one block to another. Herein, PTx alternates between information and power stages according to $\boldsymbol{\tau}_{\mathbf{t}_\alpha} = \begin{bmatrix} 1 & 0 & 1 & 0 & 0 & 1 \end{bmatrix}$, where $\mathbf{t}_\alpha = \begin{bmatrix} 1 & 3 & 6 \end{bmatrix}$, indicating that the locations of the information and power stages in time domain carry additional information bits.

5.1.2 RIS Absorption Function and WEH

The absorbing function of UCs enables RIS operations through WEH without requiring an external battery or power grid. Hence, RF energy harvesting on the RIS can be achieved through RF switches since they can act as both reflectors and absorbers [Wang et al., 2024]. Accordingly, RF switches are utilized in RIS as UCs, with N_2 UCs serving as perfect absorbers and the remaining $N - N_2$ UCs functioning as perfect reflectors. The RF switch allocates one output port for an impedance-matching component, which absorbs the energy of incoming signals instead of reflecting them. The absorbed signals are fed to the RF combining network, which combines the signals in the RF domain [Shen and Clerckx, 2021a] and outputs them to the nonlinear rectenna as input for obtaining harvested DC power such that the rectenna's input at time instant k is mathematically given by

$$\mathrm{Q}_k = \left| \sum_{n_2=N_1+1}^{N_2} h_{r,2}^{n_2} s_k \right|^2 . \tag{5.5}$$

The constant-linear-constant (CLC) model is employed to capture the practical characteristics of a rectenna, including turn-on sensitivity and saturation. [Moon et al., 2021]. In the CLC rectenna model, the harvested DC power, $\mathcal{P}_{\mathrm{DC}}(\mathrm{Q})$ is expressed as follows:

$$\mathcal{P}_{\mathrm{DC}}(\mathrm{Q}_k) = \begin{cases} 0, & \mathrm{Q}_k \in [0, \mathcal{P}_{\mathrm{on}}) \\ \rho(\mathrm{Q}_k - \mathcal{P}_{\mathrm{on}}), & \mathrm{Q}_k \in [\mathcal{P}_{\mathrm{on}}, \mathcal{P}_{\mathrm{sat}}) \\ \rho(\mathcal{P}_{\mathrm{sat}} - \mathcal{P}_{\mathrm{on}}), & \mathrm{Q}_k \in [\mathcal{P}_{\mathrm{sat}}, \infty) \end{cases} . \tag{5.6}$$

Here, ρ denotes the WEH efficiency, and Q_k represents the input power to the rectifier at time instant k. The turn-on sensitivity $\mathcal{P}_{\mathrm{on}}$ is the minimum received DC power required to activate the rectenna for RF-to-DC conversion. Saturation occurs when the rectenna reaches its maximum power harvesting capacity. The maximum harvested DC power is expressed as $\mathcal{P}_{\max} = \eta(\mathcal{P}_{\mathrm{sat}} - \mathcal{P}_{\mathrm{on}})$. Since the input power of the rectifier circuit varies depending on the specific application, $\mathcal{P}_{\mathrm{sat}}$ and $\mathcal{P}_{\mathrm{on}}$ should be adjusted according to the input power level. When the input power to the rectifier circuit is high, increasing $\mathcal{P}_{\mathrm{sat}}$ can optimize the benefits of the high input power.

Due to the fact that the RIS relies on WEH through its N_2 absorbers to serve its functions, the harvested DC power $\mathcal{P}_{\mathrm{DC}}(\mathrm{Q}_k^{\mathrm{RIS}})$ should be sufficient to maintain the total power consumption of the RIS. The total power consumption required to operate the RIS consists of two parts: the static power consumption caused by the RIS controller and the dynamic power consumption generated by the RIS UCs. Therefore, the total power consumption modeling of RIS can be expressed as follows:

$$P_{\mathrm{RIS}} = P_{\mathrm{stc}} + P_{\mathrm{dyn}} \tag{5.7}$$

where P_{stc}, and P_{dyn} refer to the static and dynamic power consumption of RIS, respectively. P_{stc} consists of the power consumption of the control board, P_{cb}, which has a constant value, and the power consumption of the drive circuits, P_{drv}, which varies with the type of UC driving mechanism. Therefore, various UCs, such as varactors and RF switches, exhibit distinct power consumption characteristics [Petrou and Georgiou, 2022]. Since varactor-based UCs require power-hungry DACs to achieve continuous phase shifts, they lead to increased static power consumption. As N increases, P_{stc} tends to dominate P_{dyn}, making the self-sustainable condition challenging [Ntontin et al., 2024]. To accomplish a standalone RIS architecture, one can utilize RF switches directly driven by RIS controllers without DACs [Wang et al., 2024]. Additionally, an integrated architecture for the RIS controller is a favorable approach to constructing a standalone RIS, as it consumes very low power during static conditions compared to conventional RIS controllers [Petrou and Georgiou, 2022]. Thus, RF switches combined with an integrated architecture could offer a potential solution to meet the standalone RIS condition despite the discrete phase shift capability of RIS compared to the continuous phase shifts provided by varactor-based UCs. The power consumption of the integrated architecture for varactors and RF switches is given by, respectively,

$$P_{\text{RIS}} = \begin{cases} \lceil N/N_{\text{cb}} \rceil P_{\text{cb}} + N\left(2P_{\text{drv}} + P_{\text{varactor}}\right), & \text{for varactor} \\ \lceil N/N_{\text{cb}} \rceil P_{\text{cb}} + NP_{\text{switch}}, & \text{for RF switch} \end{cases}, \tag{5.8}$$

where N_{cb} is the number of UCs controlled by one RIS controller, and $P_{\text{dyn}} \in \{P_{\text{switch}}, P_{\text{varactor}}\}$. The condition that verifies the standalone RIS operation can be given as follows:

$$\frac{1}{K}\sum_{k=1}^{K} \mathcal{P}_{\text{DC}}(\text{Q}_k^{\text{RIS}}) \geq P_{\text{RIS}}, \tag{5.9}$$

which implies that the average harvested DC power over a block of length K should be at least equal to or greater than the power consumption of the RIS.

5.1.3 RIS-enabled passive transmission model

During the information stage, the RIS performs two functions: it assists PTx transmission using N_1 UCs and transmits RIS information through N_3 UCs by applying a phase shift to the signal. Since RF switches are utilized, they can induce discrete phase shifts based on the b-bit resolution from a discrete set, i.e., $\phi_l \in$

$\mathcal{J} = \{0, 2\pi/B, \ldots, (B-1)\pi/B\}$, where ϕ_l represents the common phase shift within the l-th group. The RIS can generate $B = 2^b - 1$ different phase shift levels, as one output port of the RF switches is dedicated to an absorber. Once designed, these phase shifts remain invariant across all channel realizations in the RF switch-based RIS architecture. If a 2-bit resolution RF switch is employed, the possible phase shifts can be expressed as follows:

$$\phi_l \in \left\{ \phi_1 \quad \phi_2 \quad \phi_p \right\}. \tag{5.10}$$

Considering the discrete set in (5.10), in the power stage, the RIS UCs configure the phases of $N - N_2 = N_1 + N_2$ UCs to ϕ_p for power transmission. In the information stage, the RIS selects phase shifts from the set $\mathcal{J}'$, where $\mathcal{J}' = \left\{ \theta_c : 1 \leq c \leq J \right\}$, to represent one bit of information based on the two possible phase options $\theta_c \in \{\phi_1, \phi_2\}$; therefore, the modulation order of RIS information is $J = 2$. The first group of N_1 UCs can alter their phase shifts at each information transmission slot by selecting the closest phase from the set $\mathcal{J}'$ to assist PTx transmission. Meanwhile, to achieve mutualistic SR [Liang et al., 2020], the RIS aligns the third group of N_3 UCs to an invariant phase shift across L information slots during a block of length K. Therefore, the symbol period of RIS information is larger than that of PTx, provided that $L > 1$, and the parameter $\delta = L$ represents the spreading gain that affects the mutualistic symbiosis, and increasing δ improves the detection performance of RIS information at PRx [Zhang and Long, 2022].

Let $\psi_l = \beta_l e^{-j\phi_l}$ denote the reflect beamforming coefficient at the l-th RIS group in which $\beta_l \in [0, 1]$ is the common reflection amplitude within the l-th group and $\mathbf{\Psi}_k = \begin{bmatrix} \psi_1 & \psi_2 & \psi_3 \end{bmatrix}^T$ denote the reflection vector. The received signal at PRx at time instant k is written as:

$$\mathbf{y}_k = \mathbf{h}_d s_k + \sum_{n_1=1}^{N_1} \mathbf{g}_{d,1}^{n_1} e^{-j\phi_l} h_{r,1}^{n_1} s_k + \sum_{n_3=N_2+1}^{N_3} \mathbf{g}_{d,3}^{n_3} e^{-j\phi_l} h_{r,3}^{n_3} s_k + \mathbf{z}_k. \tag{5.11}$$

Herein, the reflection amplitudes are fixed to $\beta_l = 1$ for the first and third groups to maximize the reflected power, while $\beta_2 = 0$ since the second group absorbs the signal such that $\psi_2 = 0$. Additionally, $\mathbf{z}_k \in \mathbb{C}^{M_{\mathrm{R}} \times 1}$ denotes the additive white Gaussian noise (AWGN) sample vector, where each element $z_k \sim \mathcal{CN}(0, \sigma^2)$ has a zero mean and variance σ^2, added to the signal at each information stage. Defining $\underline{\mathbf{f}} \triangleq \begin{bmatrix} \mathbf{G}_{r,1}\mathbf{h}_{r,1} & \mathbf{G}_{r,2}\mathbf{h}_{r,2} & \mathbf{G}_{r,3}\mathbf{h}_{r,3} \end{bmatrix} \in \mathbb{C}^{N_{\mathrm{R}}\times 3}$ as PTx-RIS-PRx cascaded channel matrix, the (5.11) can be rewritten as:

$$\mathbf{y}_k = \mathbf{h}_d s_k + \underline{\mathbf{f}}\mathbf{\Psi}_k s_k + \mathbf{z}_k. \tag{5.12}$$

Similarly, the received signal at EH is given by

$$\varepsilon_k = h_e s_k + \underline{\mathbf{v}}\mathbf{\Psi}_k s_k, \tag{5.13}$$

where $\underline{\mathbf{v}} \triangleq \begin{bmatrix} \mathbf{h}_{r,1}\mathbf{g}_{e,1} & \mathbf{h}_{r,2}\mathbf{g}_{e,2} & \mathbf{h}_{r,3}\mathbf{g}_{e,3} \end{bmatrix} \in \mathbb{C}^{1\times 3}$ denotes the PTx-RIS-EH cascaded channel matrix and AWGN term is omitted since it is too low to be harvested. Therein, $\mathrm{Q}_{\mathrm{EH}} = |\varepsilon_k|^2$ is input for the CLC rectenna defined in (5.6) and the average harvested DC power can be calculated by putting $\mathrm{Q}_k^{\mathrm{EH}}$ into (5.9).

The cascaded channel of the PTx-RIS-PRx (EH) links can be estimated using the method in [Jensen and De Carvalho, 2020]. Subsequently, we assume that PTx perfectly knows the cascaded channel and direct link channel. Therefore, PTx can transmit the phase knowledge and the corresponding transmission stage to the RIS prior to each transmission by determining the phase shift of the first group through $\psi_1 = \arg\min_{\theta_c\in\mathcal{J}'}|\theta_c - \mathbb{E}[(\angle\mathbf{G}_{r,1}\mathbf{h}_{r,1} + \angle h_d)]|^2$. Accordingly, the RIS sets the phase of N_1 UCs and arranges the phase of N_3 UCs at time instant k.

5.2 SR-based Decoder

The PRx task involves jointly estimating the time-index vector $\boldsymbol{\tau}_{\mathbf{t}_\alpha}$ as well as the information of PTx and RIS by considering all possible time-index selections and corresponding symbols from the sets $\mathcal{S}$ and $\mathcal{J}'$, respectively. To do so, PRx employs a maximum likelihood (ML) detector and minimizes the following metric:

$$\left(\hat{\boldsymbol{\tau}}_{\mathbf{t}_\alpha}, \hat{\mathbf{x}}_n, \hat{\psi}_3\right) = \arg\min_{\substack{\mathbf{x}_n\in\mathcal{S}\\ \mathbf{t}_\alpha\in\mathcal{T}\\ \psi_3\in\mathcal{J}'}} \sum_{k=1}^{L} \|\mathbf{y}_k - \mathbf{h}_d s_k + \underline{\mathbf{f}}\mathbf{\Psi}_k s_k\|^2. \tag{5.14}$$

Since the ML detector searches for all possible mapping rules and the corresponding symbols, the decoding complexity increases as K, L, and M grow. The

Algorithm 1: LLR-Based Detector for TIM

Require: $\mathbf{y}_k$, $\mathbf{h}_d$, $\underline{\mathbf{f}}$, $\mathbf{\Lambda}_c$, $\mathbf{\Omega}$, $\mathcal{J}'$, $\mathcal{M}$, σ^2, K, L

Ensure : ϑ_k is the LLR of k-th time instant

for $k = 1$ ***to*** K **do**

    $\Delta_i = -\frac{1}{\sigma^2}\|\mathbf{y}_k - \mathbf{h}_d x_1 + \underline{\mathbf{f}}\mathbf{\Lambda}_1 x_1\|^2$

    $\Delta_p = -\|\mathbf{y}_k - \mathbf{h}_d \omega + \underline{\mathbf{f}}\mathbf{\Omega}\omega\|^2$

    for $c = 1$ ***to*** J **do**

        for $i = 2$ ***to*** M **do**

            $\xi_1 = -\frac{1}{\sigma^2}\|\mathbf{y}_k - \mathbf{h}_d x_i + \underline{\mathbf{f}}\mathbf{\Lambda}_c x_i\|^2$

            $\xi_2 = \max\{\Delta_i, \xi_1\} + \ln(1 + \exp(-|\xi_1 - \Delta_i|))$

            $\Delta_i = \xi_2$

        end

    end

    $\vartheta_k = \ln(L^2) - \ln((K-L)^2) + \Delta_i - \Delta_p$

end

return $\boldsymbol{\vartheta}$

computational complexity of the ML detector is approximately $\mathcal{O}(2^{\eta_r} J M^L)$ in terms of complex multiplications. Therefore, we propose an LLR-based detector for our scheme to reduce the decoding complexity while maintaining the reliability of decoding at PRx.

Let us define two vectors for the information and power stages from $\mathbf{\Psi}_k$ to ease the exposition. To describe the power stage, we can represent $\mathbf{\Psi}_k$ as $\mathbf{\Omega} = \begin{bmatrix} e^{-j\phi_p} & 0 & e^{-j\phi_p} \end{bmatrix}$, and for the information stage, $\Lambda_c = \begin{bmatrix} \psi_1 & 0 & \theta_c \end{bmatrix}$. Now, we can write the expression representing the logarithm ratio of the a posteriori probabilities of the symbols, taking into account that their values may indicate the selection of either information or power signal. The expression is as follows:

$$\vartheta_k = \ln\left(\frac{\sum_{c=1}^{J}\sum_{i=1}^{M}\Pr\left(s_k = x_i, \psi_3 = \theta_c \mid \mathbf{y}_k\right)}{\Pr\left(s_k = \omega, \psi_3 = \phi_p \mid \mathbf{y}_k\right)}\right). \tag{5.15}$$

A higher value of ϑ_k in (5.15) indicates a higher likelihood of information being

Algorithm 2: Mapping Rule-aided Info. Slot Selection

Require: $\boldsymbol{\vartheta}$, $\mathcal{T}$, η_r, K, L

Ensure : $\mathbf{t}_\alpha$ belongs to the legitimate set $\mathcal{T}$ and $\mathbf{t}_\alpha^\iota$ is the ι-th element of $\mathbf{t}_\alpha$.

$\vartheta = \boldsymbol{\vartheta}_k$
$\mathbf{b} = \mathbf{0}_{2^{\eta_r}\times 1}$
for $\alpha = 1$ ***to*** 2^{η_r} **do**
  if $L > 1$ **then**
    for $\iota = 1$ ***to*** L **do**
      $a = \mathbf{t}_\alpha^\iota$
      $\mathbf{b}_\alpha \mathrel{+}= \boldsymbol{\vartheta}_a$
    end
  end
  else if $L = 1$ **then**
    $a = \mathbf{t}_\alpha$
    $\mathbf{b}_\alpha = \boldsymbol{\vartheta}_a$
  end
end
$\mathbf{t}_\alpha = \arg\max_\alpha \{\mathbf{b}_\alpha\}$
return $\hat{\boldsymbol{\tau}}_{\mathbf{t}_\alpha}$

transmitted at time instant k. Applying Bayes' formula, with $\Sigma_{i=1}^{M}\Pr(s_k = x_i) = \Sigma_{c=1}^{J}\Pr(s_k = \theta_c) = L/K$ and $\Pr(s_k = \omega) = \Pr(\psi_3 = \phi_p) = (K-L)/K$, (5.15) can be expanded as:

$$\begin{aligned}\vartheta_k = &\ln\left(\sum_{c=1}^{J}\sum_{i=1}^{M}\exp\left(-\frac{1}{\sigma^2}\|\mathbf{y}_k - \mathbf{h}_d x_i + \underline{\mathbf{f}}\boldsymbol{\Lambda}_c x_i\|^2\right)\right)\\ &- \ln\left(\exp\left(-\|\mathbf{y}_k - \mathbf{h}_d\omega + \underline{\mathbf{f}}\boldsymbol{\Omega}\omega\|^2\right)\right) + \ln\left(L^2\right) - \ln\left((K-L)^2\right). \end{aligned} \tag{5.16}$$

Then, recursion initializes with $\Delta_i = -\frac{1}{\sigma^2}\|\mathbf{y}_k - \mathbf{h}_d x_1 + \underline{\mathbf{f}}\boldsymbol{\Lambda}_1 x_1\|^2$. To avoid numerical overflow, we utilize the following identity: $\ln\left(e^{\xi_1} + e^{\xi_2} + \cdots + e^{\xi_\chi}\right) = \ln\left(e^{\Delta_i} + e^{\xi_\chi}\right) = \max\{\Delta_i, \xi_\chi\} + \ln\left(1 + e^{-|\xi_\chi - \Delta_i|}\right)$ [Basar et al., 2013] at each iteration in which $\xi_\chi = \|\mathbf{y}_k - \mathbf{h}_d x_i + \underline{\mathbf{f}}\boldsymbol{\Lambda}_j x_i\|^2$ by setting $c = 1$ to J and $i = 2$ to M. Since

Table 5.1: MAPPING RULE of $\boldsymbol{\tau}_{\mathbf{t}_{\boldsymbol{\alpha}}}$ for $K = 4$ and $L = 2$.

Bits	$\boldsymbol{\tau}_{\mathbf{t}_{\alpha}}$	$\mathcal{T}$
00	$\begin{bmatrix}1 & 0 & 1 & 0\end{bmatrix}$	$\mathbf{t}_1 = \begin{bmatrix}1 & 3\end{bmatrix}$
01	$\begin{bmatrix}1 & 0 & 0 & 1\end{bmatrix}$	$\mathbf{t}_2 = \begin{bmatrix}1 & 4\end{bmatrix}$
10	$\begin{bmatrix}0 & 1 & 0 & 1\end{bmatrix}$	$\mathbf{t}_3 = \begin{bmatrix}2 & 4\end{bmatrix}$
00	$\begin{bmatrix}0 & 1 & 1 & 0\end{bmatrix}$	$\mathbf{t}_4 = \begin{bmatrix}2 & 3\end{bmatrix}$
X	$\begin{bmatrix}1 & 1 & 0 & 0\end{bmatrix}$	-
X	$\begin{bmatrix}0 & 0 & 1 & 1\end{bmatrix}$	-

there is one possible power signal once $\Delta_p = -\|\mathbf{y}_k - \mathbf{h}_d\omega + \underline{\mathbf{f}}\boldsymbol{\Omega}\omega\|^2$ is evaluated and keep the same for each iteration. Afterward, LLR value is obtained by Algorithm 1 for each time instant k and they are collected in a vector which is given by

$$\boldsymbol{\vartheta} = \begin{bmatrix}\vartheta_1 & \vartheta_2 & \dots & \vartheta_k\end{bmatrix}. \tag{5.17}$$

Finally, the receiver decides on the time indices of L information slots $\mathbf{t}_\alpha$ based on maximum LLR values with the aid of $\boldsymbol{\vartheta}$ and estimates $\hat{\boldsymbol{\tau}}_{\mathbf{t}_{\boldsymbol{\alpha}}}$. It can be seen that the proposed LLR detector simplifies decoding complexity to around $\mathcal{O}(K(JM+1))$ in terms of complex multiplications.

The mapping rule for $(K = 4, L = 2)$ is demonstrated in Table 5.1. When selecting $(4, 2)$, there are 6 possible mappings. Nevertheless, only $2^{\lfloor \log_2(6) \rfloor} = 4$ legitimate mappings can be chosen, as there are four possible bit combinations. Therefore, it is likely to decide on an illegitimate set with Algorithm 1.

Assuming that $\hat{L}$ is the number of estimated information slots in $\hat{\boldsymbol{\tau}}_{\mathbf{t}_{\boldsymbol{\alpha}}}$, in cases where $\hat{L} > L$ or $\hat{L} < L$, or even when $\hat{L} = L$, the receiver can detect $\boldsymbol{\tau}_{\mathbf{t}\boldsymbol{\alpha}}$, which is not specified in the mapping rule, such that the detection process will fail. Thus, we present an LLR detector that operates in cooperation with the mapping rule to prevent the detection of illegitimate sets. Hence, regarding the potential scenario where the PRx might choose $\boldsymbol{\tau}_{\mathbf{t}\boldsymbol{\alpha}}$ that does not belong to the mapping rule, Algorithm 2 is provided to compute the maximum LLR sum for determining time-indices $\mathbf{t}_\alpha$ from legitimate set $\mathcal{T}$ [Basar et al., 2013]. Ultimately, to estimate $(\hat{\mathbf{x}}_n, \hat{\psi}_3)$ for selected time instants (information slots), the receiver applies an ML detector, which can be expressed as:

$$\left(\hat{\mathbf{x}}_n, \hat{\psi}_3\right) = \arg \min_{\substack{\mathbf{x}_n \in \mathcal{S} \\ \psi_3 \in \mathcal{J}'}} \sum_{\alpha=1}^{L} \|\mathbf{y}_\alpha - \mathbf{h}_d s_\alpha + \underline{\mathbf{f}} \mathbf{\Psi}_\alpha s_\alpha\|^2. \tag{5.18}$$

where $\mathbf{y}_\alpha, s_\alpha, \mathbf{\Psi}_\alpha$ corresponds to the estimated time indices in $\hat{\boldsymbol{\tau}}_{\mathbf{t}_{\boldsymbol{\alpha}}}$ computed by Algorithm 2.

5.3 Numerical Results

In this section, we evaluate the performance of our proposed scheme in terms of average harvested DC power and bit error rate (BER). For all channels, a Rician factor $\kappa_p = 5$ is considered, and the 3GPP Indoor hotspot (InH) path loss model is employed, which is expressed as follows [3GPP, 2010]:

$$\nu_p(d) = 32.8 + 16.9 \log_{10}(d) + 20 \log_{10}(f), \tag{5.19}$$

where f is the carrier frequency, and d refers to the distance, with $d \in \{5, 10, 14\}$ for the PTx-RIS, RIS-PRx (EH), and PTx-RIS-PRx (EH) links, respectively. Unless otherwise specified, 4-QAM is employed at PTx, and $M_R = 4$, and $N_1 = 60$ are used in the simulations. The simulation parameters are presented in Table 5.2.

We aim to demonstrate the proposed standalone RIS architecture in terms of average harvested DC power and the number of N_2 UCs required to meet the condition

Table 5.2: SIMULATION PARAMETERS

	Parameter	Value
PTx	P_L, P_H	30 dBm, 34 dBm
	f	2 GHz
RIS	N, N_{cb}	$256, 4$
	P_{cb}, P_{dyn}	50 μW , 40 μW [Petrou and Georgiou, 2022]
	P_{switch}, P_{varactor}	1μW [Rossanese et al., 2022], 0 W [Wang et al., 2024]
	ρ, $\mathcal{P}_{\text{on}}$, $\mathcal{P}_{\text{sat}}$	0.75, 150 μW, 70 mW
EH	ρ, $\mathcal{P}_{\text{on}}$, $\mathcal{P}_{\text{sat}}$	0.75, 50 μW, 0.1 mW

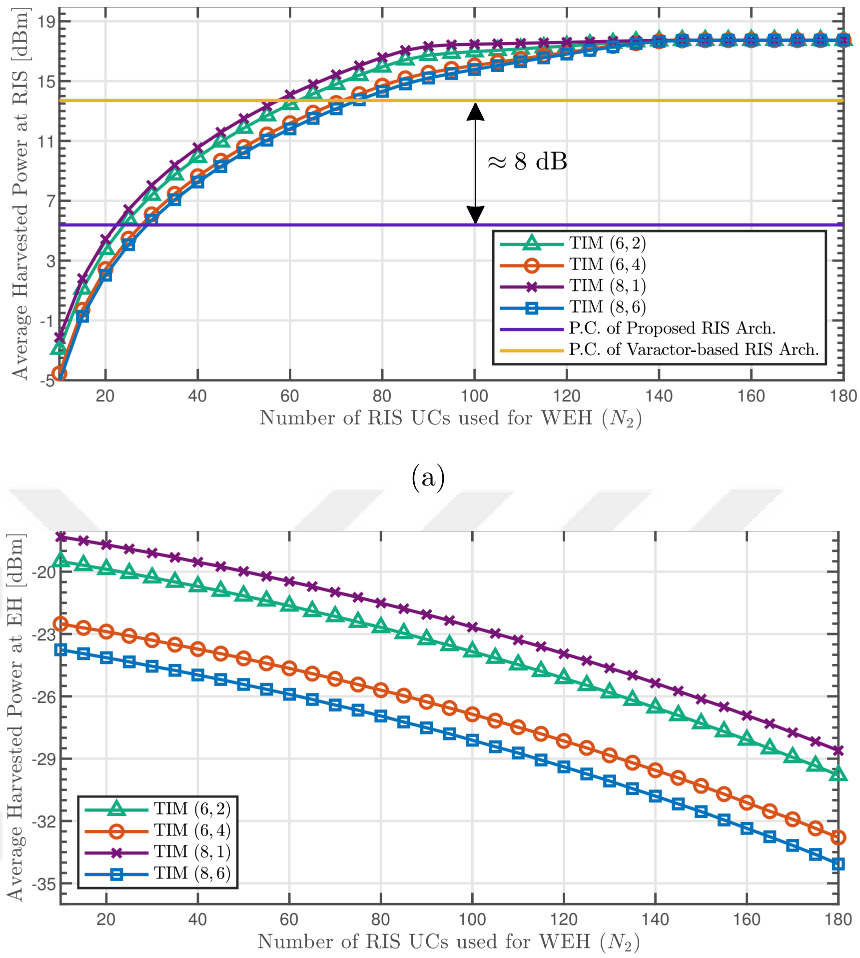

(a)

(b)

Figure 5.3: Average harvested DC power (5.5) with respect to N_2 UCs for (a) standalone RIS and (b) EH.

(5.9). Fig. 5.3(a) indicates that the minimum number of N_2 UCs required for a standalone RIS architecture is approximately two times fewer for RF switches compared to varactors. This difference arises as varactors are driven by power-hungry DACs that make accomplishing a standalone operation challenging, resulting in roughly 8 dB more power consumption than RF switches. As expected, reserving more time slots for the power stage in the TIM scheme increases the average harvested DC power, as illustrated in Figs. 5.3(a) and 5.3(b). Importantly, around $N_2 = 140$, the CLC rectenna reaches saturation region for all TIM schemes. Herein, it is crucial to mention the parameters of the CLC rectenna model can be reconfigured according

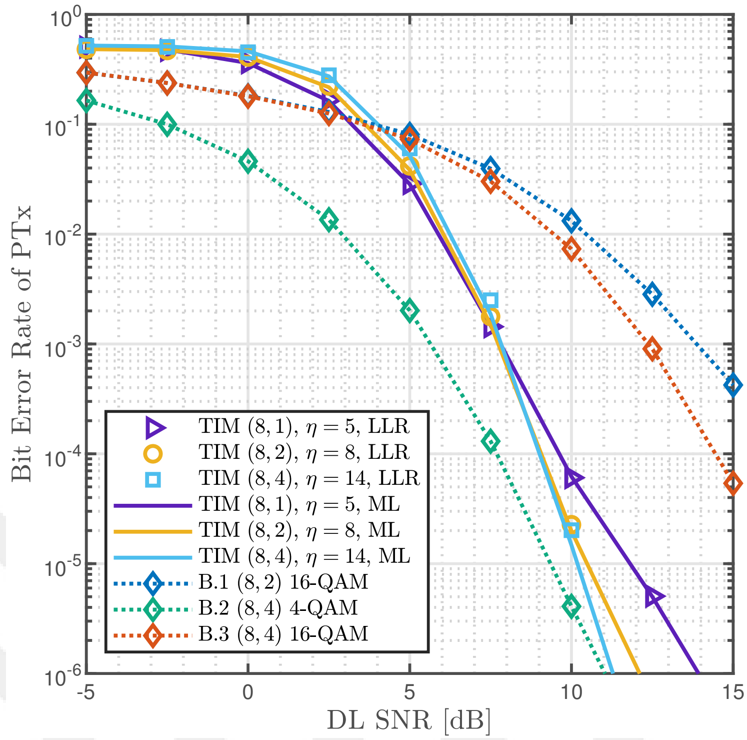

Figure 5.4: BER comparison of PTx with benchmark schemes with respect to DL SNR.

to N_2 UCs to leverage the benefits effectively. Furthermore, allocating more N_2 UCs at the RIS reduces the average harvested DC power at the EH, as the total number of reflectors, which is $N - N_2$ UCs, decreases. Since $N_2 = 35$ satisfies the standalone condition (5.9) for all schemes in Fig. 5.3(a), we exploit this in our simulations to ensure that RIS performs its functions by WEH in the SR environment.

In Figs. 5.4 and 5.5, we demonstrate the BER performance of our scheme for ML and LLR detectors with respect to direct link (DL) signal-to-noise ratio (SNR), $\gamma_{\mathrm{DL}} = \nu_{h_d}(d)/\sigma^2$. It can be observed from Figs. 5.4 and 5.5 that BER performances of the ML and LLR detectors align with one another. However, the LLR detector reduces the complexity by approximately 86% compared to the ML detector in terms of complex multiplications, considering the TIM $(8, 2)$ scheme. Additionally, based on the setup in [Yang et al., 2024], we compare our scheme with benchmarks. We assume that the benchmark schemes maintain RIS information unchanged for L

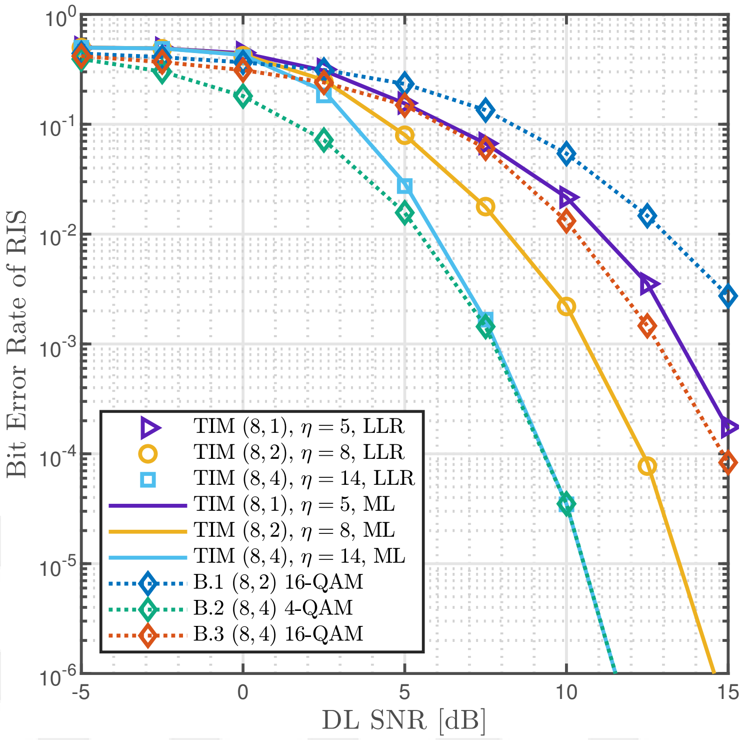

Figure 5.5: BER comparison of RIS with benchmark schemes with respect to DL SNR.

information slots for a block size of $K = 8$, without utilizing TIM at the PTx. Thus, the benchmark schemes convey $\eta_m = L\log_2(M)$ bits and $(K - L)$ power signals in a given block. In Fig. 5.4, the benchmark scheme B.2 outperforms our proposed scheme. Nevertheless, when considering the $(8, 2)$ case, since our scheme exploits six time slots for power transfer while the benchmark B.2 uses four time slots, the average harvested DC power in a block size of K should be higher than that of B.2. If the benchmark utilizes six time slots (B.1) for power transfer, all TIM schemes show their superiority against it. Thus, modulating bits in the time domain rather than the signal domain enhances the BER performance of the SR system. In Fig. 5.5, the proposed scheme outperforms benchmark B.1 in terms of BER of RIS information. Despite B.3 having a spreading gain four times that of the TIM $(8, 1)$ case, their performances are close due to the fact that PTx and RIS information are coupled. Therefore, increasing the modulation order M of PTx has a detrimental

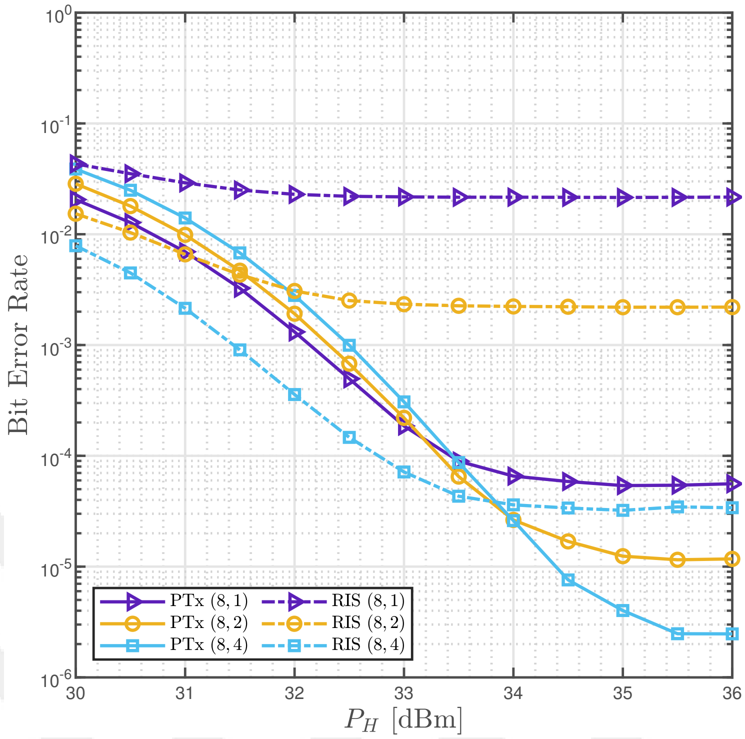

Figure 5.6: BER comparison of PTx and RIS for various TIM schemes with varying P_H.

impact on RIS information. Additionally, as the DL SNR increases, the BER of B.2 and TIM $(8, 4)$ cases become indistinguishable. Moreover, the BER performance of the RIS improves with increasing spreading gain δ, which also enhances the BER of PTx in the high SNR region, as observed in Fig. 5.4.

To emphasize the effect of P_H on decoding performance in the LRR detector, the BER for PTx and RIS information is plotted in Fig. 5.6 with $\gamma_{\mathrm{DL}} = 10$ dB. As P_H increases, the distinction between information and power stages becomes more accurate, leading to a better estimation of time-index bits in the LLR detector. Interestingly, the impact of P_H on the BER of RIS information is highly coupled with the spreading factor δ. Therefore, as δ improves, increasing P_H becomes more meaningful for achieving better BER performance. Furthermore, the BER of PTx and RIS information saturates after a specific SNR value in all TIM schemes, indicating that further increasing P_H will not affect decoding performance.

Chapter 6

CONCLUSION

The massive connections of simple nodes present significant challenges to the communication infrastructure as we move towards 6G technology. Establishing sustainable, green, and secure communication accounts for providing synergistic ways of delivering information and power to IoT devices. Chapter 3 presents a comprehensive framework for the IH mechanism, leveraging existing far-field WPT mechanisms to enable wireless communication through exploiting diverse IM techniques. The presented simulations and analytical derivations underline the advantages of IM-based IH mechanisms, particularly in terms of energy harvesting capabilities at the EH and the reliability and secrecy of the communication at the IR. In this respect, the results reveal that the IH mechanism can extend the far-field WPT range and energy harvesting capability while ensuring secure and reliable WIT through efficient transmitter design by harnessing the amalgamation of multitone signals with IM techniques. In summary, the IH mechanism holds significant potential for IoT devices in the 6G era by introducing a novel communication channel atop existing WPT mechanisms.

In Chapter 4, Information Harvesting concept has been applied to OFDM-based far-field power transfer systems. The simulation results verify that OFDM-based IH can boost energy harvesting capability at the EH, and while the achievable rate may not match its energy harvesting superiority compared to its counterparts, it provides comparable performance when the power budget is relaxed. Furthermore, dual-mode OFDM introduces some sacrifice in terms of reliability along with enhanced energy harvesting capability compared to the proposed one. Following the presented results, it becomes apparent that OFDM-based IH has the potential to serve as an alternative approach in the establishment of carbon-free communication platform in future networks.

The coexistence of cellular and IoT devices in next-generation communication frameworks becomes more power and bandwidth-hungry as the number of connected devices increases. Therefore, delivering power and information in a mutualistic manner is of paramount importance for designing next-generation networks. Chapter 5 presents a novel low-power, standalone RIS architecture that serves as a BD in an SR environment. In this setup, the PTx utilizes a TIM scheme to transfer information to the PRx and power to the RIS and EH, respectively. We propose an LLR-based detector to reduce computational complexity at the PRx and investigate the proposed scheme in terms of average harvested DC power and BER performance while ensuring the necessary conditions for being a standalone RIS. Our results demonstrate that a standalone RIS can establish a mutualistic symbiosis with the PTx, and the proposed system can achieve reliable communication while incorporating power transfer into its transmission strategy without demanding additional power resources.

Consequently, these studies demonstrate the novel and synergistic implementation of information and power transfer mechanisms through emerging technologies for the next-generation frameworks. Deploying RF energy harvesting is a longstanding challenge, and novel ways are required to investigate the relationship between WPT and WIT. Future works can include innovative WPT-suitable modulation designs and proper channel modeling of wireless communication systems that employ RF energy harvesting to power devices or even enable zero-power devices.

BIBLIOGRAPHY

[3GPP, 2010] 3GPP (Mar. 2010). Further advancements for E-UTRA physical layer aspects (release 9). Technical Report TR 36.814 v9.0.0 (2010-03), 3GPP.

[Abadal et al., 2020] Abadal, S., Cui, T.-J., Low, T., and Georgiou, J. (2020). Programmable metamaterials for software-defined electromagnetic control: Circuits, systems, and architectures. *IEEE J. Emerg. Sel. Top. Circuits Syst.*, 10(1):6–19.

[Alevizos and Bletsas, 2018] Alevizos, P. N. and Bletsas, A. (2018). Sensitive and nonlinear far-field RF energy harvesting in wireless communications. *IEEE Trans. Wireless Commun.*, 17(6):3670–3685.

[Amarasuriya et al., 2016] Amarasuriya, G., Larsson, E. G., and Poor, H. V. (2016). Wireless information and power transfer in multiway massive MIMO relay networks. *IEEE Trans. Wireless Commun.*, 15(6):3837–3855.

[Ayir and Riihonen, 2023] Ayir, N. and Riihonen, T. (2023). Efficiency–throughput trade-off of pulsed rf waveforms in simultaneous wireless information and power transfer. In *IEEE Wireless Power Technol. Conf. Expo (WPTCE)*, pages 1–5.

[Basar et al., 2013] Basar, E., Aygolu, U., Panayirci, E., and Poor, H. V. (2013). Orthogonal frequency division multiplexing with index modulation. *IEEE Trans. Signal Process.*, 61(22):5536–5549.

[Basar et al., 2019] Basar, E., Di Renzo, M., De Rosny, J., Debbah, M., Alouini, M.-S., and Zhang, R. (2019). Wireless communications through reconfigurable intelligent surfaces. *IEEE Access*, 7:116753–116773.

[Basar et al., 2017] Basar, E., Wen, M., Mesleh, R., Di Renzo, M., Xiao, Y., and

Haas, H. (2017). Index modulation techniques for next-generation wireless networks. *IEEE Access*, 5:16693–16746.

[Bi et al., 2016] Bi, S., Zeng, Y., and Zhang, R. (2016). Wireless powered communication networks: an overview. *IEEE Wireless Commun.*, 23(2):10–18.

[Boaventura et al., 2015] Boaventura, A., Belo, D., Fernandes, R., Collado, A., Georgiadis, A., and Carvalho, N. B. (2015). Boosting the efficiency: Unconventional waveform design for efficient wireless power transfer. *IEEE Microw. Mag.*, 16(3):87–96.

[Boyer and Roy, 2014] Boyer, C. and Roy, S. (2014). — invited paper — backscatter communication and rfid: Coding, energy, and mimo analysis. *IEEE Trans. Commun.*, 62(3):770–785.

[Buckley and Heath, 2021] Buckley, R. F. and Heath, R. W. (2021). System and design for selective OFDM SWIPT transmission. *IEEE Trans. Green Commun. Netw.*, 5(1):335–347.

[Cansiz et al., 2020] Cansiz, M., Altinel, D., and Kurt, G. K. (2020). Effects of different modulation techniques on charging time in RF energy-harvesting system. *IEEE Trans. Instrum. Meas.*, 69(9):6904–6911.

[Clerckx and Bayguzina, 2016] Clerckx, B. and Bayguzina, E. (2016). Waveform design for wireless power transfer. *IEEE Trans. Signal Process.*, 64(23):6313–6328.

[Clerckx et al., 2018] Clerckx, B., Costanzo, A., Georgiadis, A., and Borges Carvalho, N. (2018). Toward 1G mobile power networks: RF, signal, and system designs to make smart objects autonomous. *IEEE Microw. Mag.*, 19(6):69–82.

[Clerckx et al., 2022] Clerckx, B., Kim, J., Choi, K. W., and Kim, D. I. (2022). Foundations of wireless information and power transfer: Theory, prototypes, and experiments. *Proc. IEEE Proc.*, 110(1):8–30.

[Clerckx et al., 2019] Clerckx, B., Zhang, R., Schober, R., Ng, D. W. K., Kim, D. I., and Poor, H. V. (2019). Fundamentals of wireless information and power transfer: From RF energy harvester models to signal and system designs. *IEEE J. Sel. Areas Commun.*, 37(1):4–33.

[Costanzo and Masotti, 2016] Costanzo, A. and Masotti, D. (2016). Smart solutions in smart spaces: Getting the most from far-field wireless power transfer. *IEEE Microw. Mag.*, 17(5):30–45.

[Di Renzo and Haas, 2010] Di Renzo, M. and Haas, H. (2010). A general framework for performance analysis of space shift keying (SSK) modulation for MISO correlated Nakagami-m fading channels. *IEEE Trans. Commun.*, 58(9):2590–2603.

[El Shafie et al., 2017] El Shafie, A., Tourki, K., and Al-Dhahir, N. (2017). An artificial-noise-aided hybrid TS/PS scheme for OFDM-based SWIPT systems. *IEEE Commun. Lett.*, 21(3):632–635.

[Federal Commun. Comm., 2016] Federal Commun. Comm. (Washington, DC, USA, 2016). 47 CFR Part15-Radio Frequency Devices.

[Goel and Negi, 2008] Goel, S. and Negi, R. (2008). Guaranteeing secrecy using artificial noise. *IEEE Trans. Wireless Commun.*, 7(6):2180–2189.

[Gu et al., 2021] Gu, X., Burasa, P., Hemour, S., and Wu, K. (2021). Recycling ambient RF energy: Far-field wireless power transfer and harmonic backscattering. *IEEE Microw. Mag.*, 22(9):60–78.

[Gu et al., 2019] Gu, Y., Wu, Z., Yin, Z., and Zhang, X. (2019). The secrecy capacity optimization artificial noise: A new type of artificial noise for secure communication in MIMO system. *IEEE Access*, 7:58353–58360.

[Huang et al., 2018] Huang, Y., Liu, M., and Liu, Y. (2018). Energy-efficient SWIPT in IoT distributed antenna systems. *IEEE Internet Things J.*, 5(4):2646–2656.

[Huang et al., 2017] Huang, Z., Gao, Z., and Sun, L. (2017). Anti-eavesdropping scheme based on quadrature spatial modulation. *IEEE Commun. Lett.*, 21(3):532–535.

[Ilter et al., 2022a] Ilter, M. C., Basar, E., Wichman, R., and Hämäläinen, J. (2022a). Information harvesting for far-field RF power transfer through index modulation. In *Proc. IEEE Glob. Commun. Conf. (GLOBECOM).*

[Ilter et al., 2024] Ilter, M. C., Pihtili, M. E., Basar, E., and Wichman, R. (2024). OFDM-based information harvesting. *IEEE Commun. Lett.*, 28(3):707–711.

[Ilter et al., 2023] Ilter, M. C., Wichman, R., Hämäläinen, J., and Ikki, S. (2023). A new information harvesting mechanism for far-field wireless power transfer. In *Proc. IEEE Veh. Tech. Conf. (VTC-Spring)*, pages 1–6.

[Ilter et al., 2022b] Ilter, M. C., Wichman, R., Säily, M., and Hämäläinen, J. (2022b). Information harvesting for far-field wireless power transfer. *IEEE Internet Things Mag.*, 5(2):127–132.

[Jeganathan et al., 2008] Jeganathan, J., Ghrayeb, A., and Szczecinski, L. (2008). Generalized space shift keying modulation for MIMO channels. In *Proc. IEEE Int. Symp. on Pers., Indoor and Mobile Radio Commun. (PIMRC)*, pages 1–5.

[Jensen and De Carvalho, 2020] Jensen, T. L. and De Carvalho, E. (2020). An optimal channel estimation scheme for intelligent reflecting surfaces based on a minimum variance unbiased estimator. In *ICASSP 2020 - 2020 IEEE Int. Conf. Acoust., Speech, Signal Process. (ICASSP)*, pages 5000–5004.

[Kang et al., 2020] Kang, S., Lee, H., Hwang, S., and Lee, I. (2020). Time switching protocol for multi-antenna SWIPT systems. *IEEE Wireless Commun. and Netw. Conf. (WCNC)*, pages 1–6.

[Kim et al., 2019] Kim, J., Clerckx, B., and Mitcheson, P. D. (2019). Experimental analysis of harvested energy and throughput trade-off in a realistic SWIPT system. In *IEEE Wireless Power Transfer Conf. (WPTC)*, pages 1–5.

[Kim et al., 2020] Kim, J., Clerckx, B., and Mitcheson, P. D. (2020). Signal and system design for wireless power transfer: Prototype, experiment and validation. *IEEE Trans. Wireless Commun.*, 19(11):7453–7469.

[Kimionis et al., 2014] Kimionis, J., Bletsas, A., and Sahalos, J. N. (2014). Increased range bistatic scatter radio. *IEEE Trans. Commun.*, 62(3):1091–1104.

[Krikidis and Psomas, 2019] Krikidis, I. and Psomas, C. (2019). Tone-index multisine modulation for SWIPT. *IEEE Signal Process. Lett.*, 26(8):1252–1256.

[Ku et al., 2016] Ku, M.-L., Li, W., Chen, Y., and Ray Liu, K. J. (2016). Advances in energy harvesting communications: Past, present, and future challenges. *IEEE Commun. Surv. Tutor.*, 18(2):1384–1412.

[Leemput et al., 2023] Leemput, D. V., Sabovic, A., Hammoud, K., Famaey, J., Pollin, S., and Poorter, E. D. (2023). Energy harvesting for wireless IoT use cases: A generic feasibility model and tradeoff study. *IEEE Internet Things J.*, pages 1–1.

[Li et al., 2016] Li, J., Wen, M., Zhang, M., and Cheng, X. (2016). Virtual spatial modulation. *IEEE Access*, 4:6929–6938.

[Liang et al., 2020] Liang, Y.-C., Zhang, Q., Larsson, E. G., and Li, G. Y. (2020). Symbiotic radio: Cognitive backscattering communications for future wireless networks. *IEEE Trans. Cogn. Commun. Netw.*, 6(4):1242–1255.

[Lin et al., 2022] Lin, S., Chen, F., Wen, M., Feng, Y., and Di Renzo, M. (2022). Reconfigurable intelligent surface-aided quadrature reflection modulation for simultaneous passive beamforming and information transfer. *IEEE Trans. Wirel. Commun.*, 21(3):1469–1481.

[Lin et al., 2021] Lin, S., Zheng, B., Alexandropoulos, G. C., Wen, M., Renzo, M. D., and Chen, F. (2021). Reconfigurable intelligent surfaces with reflection pattern modulation: Beamforming design and performance analysis. *IEEE Trans. Wirel. Commun.*, 20(2):741–754.

[Liu et al., 2013] Liu, V., Parks, A., Talla, V., Gollakota, S., Wetherall, D., and Smith, J. R. (2013). Ambient backscatter: wireless communication out of thin air. *SIGCOMM Comput. Commun. Rev.*, 43(4):39–50.

[Liu et al., 2016] Liu, W., Zhou, X., Durrani, S., and Popovski, P. (2016). SWIPT with practical modulation and RF energy harvesting sensitivity. In *Proc. IEEE Int. Conf. Commun. (ICC)*, pages 1–7.

[Liu et al., 2022] Liu, Y., Li, D., Dai, H., Li, C., and Zhang, R. (2022). Understanding the impact of environmental conditions on zero-power Internet of Things: An experimental evaluation. *IEEE Wireless Commun.*, pages 1–8.

[Long et al., 2020] Long, R., Liang, Y.-C., Guo, H., Yang, G., and Zhang, R. (2020). Symbiotic radio: A new communication paradigm for passive Internet of Things. *IEEE Internet Things J.*, 7(2):1350–1363.

[Lv et al., 2018] Lv, L., Ding, Z., Ni, Q., and Chen, J. (2018). Secure MISO-NOMA transmission with artificial noise. *IEEE Trans. Veh. Technol.*, 67(7):6700–6705.

[Mao et al., 2016] Mao, T., Wang, Z., Wang, Q., Chen, S., and Hanzo, L. (2016). Dual-mode index modulation aided OFDM. *IEEE Access*, 5:50–60.

[Mesleh et al., 2015] Mesleh, R., Ikki, S. S., and Aggoune, H. M. (2015). Quadrature spatial modulation. *IEEE Trans. Veh. Technol.*, 64(6):2738–2742.

[Mesleh et al., 2008] Mesleh, R. Y., Haas, H., Sinanovic, S., Ahn, C. W., and Yun, S. (2008). Spatial modulation. *IEEE Trans. Veh. Technol.*, 57(4):2228–2241.

[Moon et al., 2021] Moon, J. H., Park, J. J., Lee, K.-Y., and Kim, D. I. (2021). Heterogeneously reconfigurable energy harvester: An algorithm for optimal reconfiguration. *IEEE Internet Things J.*, 8(3):1437–1452.

[Nakamoto et al., 2022] Nakamoto, Y., Hasegawa, N., Hirakawa, T., and Ohta, Y. (2022). A study on OFDM modulation suitable for wireless power transfer. In *Wireless Power Week (WPW)*, pages 21–24.

[Naser et al., 2023] Naser, S., Bariah, L., Muhaidat, S., and Basar, E. (2023). Zero-energy devices empowered 6G networks: Opportunities, key technologies, and challenges.

[Nasir et al., 2020] Nasir, A. A., Tuan, H. D., Duong, T. Q., and Poor, H. V. (2020). MIMO-OFDM-based wireless-powered relaying communication with an energy recycling interface. *IEEE Trans. Commun.*, 68(2):811–824.

[Nasir et al., 2022] Nasir, A. A., Tuan, H. D., Dutkiewicz, E., Poor, H. V., and Hanzo, L. (2022). Relay-aided multi-user OFDM relying on joint wireless power transfer and self-interference recycling. *IEEE Trans. Commun.*, 70(1):291–305.

[Ntontin et al., 2023] Ntontin, K., Boulogeorgos, A. A., Björnson, E., Martins, W. A., Kisseleff, S., Abadal, S., Alarcón, E., Papazafeiropoulos, A., Lazarakis, F. I., and Chatzinotas, S. (2023). Wireless energy harvesting for autonomous reconfigurable intelligent surfaces. *IEEE Trans. Green Commun. Netw.*, 7(1):114–129.

[Ntontin et al., 2024] Ntontin, K., Boulogeorgos, A.-A. A., Abadal, S., Mesodiakaki, A., Chatzinotas, S., and Ottersten, B. (2024). Perpetual reconfigurable intelligent surfaces through in-band energy harvesting: Architectures, protocols, and challenges. *IEEE Veh. Technol. Mag.*, 19(1):36–44.

[Pan et al., 2019] Pan, G., Diamantoulakis, P. D., Ma, Z., Ding, Z., and Karagiannidis, G. K. (2019). Simultaneous lightwave information and power transfer: Policies, techniques, and future directions. *IEEE Access*, 7:28250–28257.

[Paolini et al., 2022] Paolini, G., Quddious, A., Chatzichristodoulou, D., Masotti, D., Nikolaou, S., and Costanzo, A. (2022). An energy-autonomous SWIPT RFID tag for communication in the 2.4 GHz ISM band. In *3rd URSI Atlantic and Asia Pacific Radio Science Meeting (AT-AP-RASC)*, pages 1–4.

[Park et al., 2021] Park, J. J., Moon, J. H., Jang, H. H., and Kim, D. I. (2021). Performance analysis of power amplifier nonlinearity on multi-tone SWIPT. *IEEE Wireless Commun. Lett.*, 10(4):765–769.

[Petrou and Georgiou, 2022] Petrou, L. and Georgiou, J. (2022). An ASIC architecture with inter-chip networking for individual control of adaptive-metamaterial cells. *IEEE Access*, 10:80234–80248.

[Petrou et al., 2018] Petrou, L., Karousios, P., and Georgiou, J. (2018). Asynchronous circuits as an enabler of scalable and programmable metasurfaces. In *Proc. - IEEE Int. Symp. Circuits Syst.*, pages 1–5.

[Ponnimbaduge Perera et al., 2018] Ponnimbaduge Perera, T. D., Jayakody, D. N. K., Sharma, S. K., Chatzinotas, S., and Li, J. (2018). Simultaneous wireless information and power transfer (SWIPT): Recent advances and future challenges. *IEEE Commun. Surveys Tuts.*, 20(1):264–302.

[Rossanese et al., 2022] Rossanese, M., Mursia, P., Garcia-Saavedra, A., Sciancalepore, V., Asadi, A., and Costa-Perez, X. (2022). Designing, building, and characterizing RF switch-based reconfigurable intelligent surfaces. In *Proc. 16th ACM Workshop Wireless Netw. Testbeds, Exp. Eval. & Char. (WiNTECH), 2022*, pages 69–76.

[Shen and Clerckx, 2021a] Shen, S. and Clerckx, B. (2021a). Beamforming optimization for MIMO wireless power transfer with nonlinear energy harvesting: RF combining versus DC combining. *IEEE Trans. Wirel. Commun.*, 20(1):199–213.

[Shen and Clerckx, 2021b] Shen, S. and Clerckx, B. (2021b). Joint waveform and beamforming optimization for MIMO wireless power transfer. *IEEE Trans. Commun.*, 69(8):5441–5455.

[Singh et al., 2021] Singh, U., Bhatnagar, M. R., and Tsiftsis, T. A. (2021). Secrecy analysis of SSK modulation: Adaptive antenna mapping and performance results. *IEEE Trans. Wireless Commun.*, 20(7):4614–4630.

[Tesla, 1904] Tesla, N. (1904). The transmission of electrical energy without wires. *Electrical World and Engineer*, 1:21–24.

[Tyrovolas et al., 2023] Tyrovolas, D., Tegos, S. A., Papanikolaou, V. K., Xiao, Y., Mekikis, P.-V., Diamantoulakis, P. D., Ioannidis, S., Liaskos, C. K., and Karagiannidis, G. K. (2023). Zero-energy reconfigurable intelligent surfaces (zeris). *IEEE Trans. Wirel. Commun.*, pages 1–1.

[Uysal et al., 2021] Uysal, M., Ghasvarianjahromi, S., Karbalayghareh, M., Diamantoulakis, P. D., Karagiannidis, G. K., and Sait, S. M. (2021). SLIPT for underwater visible light communications: Performance analysis and optimization. *IEEE Trans. Wireless Commun.*, 20(10):6715–6728.

[Valenta and Durgin, 2014] Valenta, C. R. and Durgin, G. D. (2014). Harvesting wireless power: Survey of energy-harvester conversion efficiency in far-field, wireless power transfer systems. *IEEE Microw. Mag.*, 15(4):108–120.

[Van Huynh et al., 2018] Van Huynh, N., Hoang, D. T., Lu, X., Niyato, D., Wang, P., and Kim, D. I. (2018). Ambient backscatter communications: A contemporary survey. *IEEE Commun. Surv. Tutor.*, 20(4):2889–2922.

[Veedu et al., 2022] Veedu, S. N. K., Mozaffari, M., Höglund, A., Yavuz, E. A., Tirronen, T., Bergman, J., and Wang, Y.-P. E. (2022). Toward smaller and lower-cost 5G devices with longer battery life: An overview of 3GPP release 17 RedCap. *IEEE Commun. Stand. Mag.*, 6(3):84–90.

[Wang et al., 2016] Wang, G., Gao, F., Fan, R., and Tellambura, C. (2016). Ambient backscatter communication systems: Detection and performance analysis. *IEEE Trans. Commun.*, 64(11):4836–4846.

[Wang et al., 2024] Wang, J., Tang, W., Liang, J. C., Zhang, L., Dai, J. Y., Li, X., Jin, S., Cheng, Q., and Cui, T. J. (2024). Reconfigurable intelligent surface: Power consumption modeling and practical measurement validation. *IEEE Trans. Commun.*, pages 1–1.

[Wang et al., 2019] Wang, N., Wang, P., Alipour-Fanid, A., Jiao, L., and Zeng, K. (2019). Physical-layer security of 5G wireless networks for IoT: Challenges and opportunities. *IEEE Internet Things J.*, 6(5):8169–8181.

[Wei et al., 2015] Wei, Y., Wang, L., and Svensson, T. (2015). Analysis of secrecy rate against eavesdroppers in MIMO modulation systems. In *Int. Conf. on Wireless Commun. Signal Process. (WCSP)*, pages 1–5.

[Wen et al., 2016] Wen, M., Cheng, X., Ma, M., Jiao, B., and Poor, H. V. (2016). On the achievable rate of OFDM with index modulation. *IEEE Trans. Signal Process.*, 64(8):1919–1932.

[Xu and Zhu, 2019] Xu, D. and Zhu, H. (2019). Secure transmission for SWIPT IoT systems with full-duplex IoT devices. *IEEE Internet Things J.*, 6(6):10915–10933.

[Xu et al., 2014] Xu, J., Liu, L., and Zhang, R. (2014). Multiuser MISO beamforming for simultaneous wireless information and power transfer. *IEEE Trans. Signal Process.*, 62(18):4798–4810.

[Yang et al., 2024] Yang, H., Ding, H., Cao, K., Elkashlan, M., Li, H., and Xin, K. (2024). A RIS-segmented symbiotic ambient backscatter communication system. *IEEE Trans. Veh. Technol.*, 73(1):812–825.

[Zhang and Long, 2022] Zhang, Y. and Long, B. (2022). A review of 5G-advanced service and system aspects standardization in 3GPP. In *2022 IEEE/CIC Int. Conf. Commun. in China (ICCC Workshops)*, pages 94–99.

[Zhao et al., 2023] Zhao, Y., Wu, Y., Hu, J., and Yang, K. (2023). A general analysis and optimization framework of time index modulation for integrated data and energy transfer. *IEEE Trans. Wirel. Commun.*, 22(6):3657–3670.

[Zhou et al., 2013] Zhou, X., Zhang, R., and Ho, C. K. (2013). Wireless information and power transfer: Architecture design and rate-energy tradeoff. *IEEE Trans. Commun.*, 61(11):4754–4767.